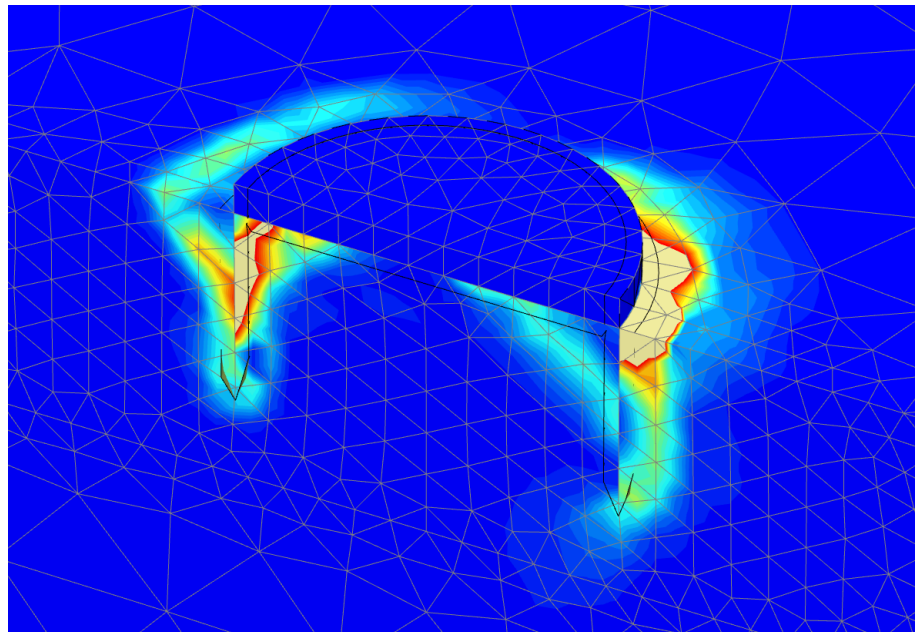


Numerical modelling of foundations for offshore wind turbines



9TH SEMESTER PROJECT - MASTER THESIS
STRUCTURAL AND CIVIL ENGINEERING
AALBORG UNIVERSITY
AUGUST 12TH 2017



AALBORG UNIVERSITY
STUDENT REPORT

School of Engineering and Science
Study Board of Civil Engineering
Thomas Manns Vej 23, 9220 Aalborg Øst
<http://www.ses.aau.dk>

Title:

Numerical modelling of foundations
for offshore wind turbines

Project period:

April 2017 - August 2017

Participant(s):

Tamás Csaba Bogdán

Supervisors:

Johan Clausen
Laura Govoni

Total pages: 115

Report pages: 91

Appendix pages: 13

Completed: 12-08-2017

Synopsis:

The aim of the thesis is to study the long-term behavior of suction caissons (bucket foundations) in drained sand. The project consists of two parts, a literature review and a numerical study part.

In the former first the most commonly used foundation types (gravity-based, monopile, jacket and suction caisson foundations) are presented in detail with a focus on bearing behavior, construction and transport and installation and operating. Consequently the most commonly used design codes and guidelines are demonstrated, pointing out the differences between and shortcomings of the deterministic, semi-probabilistic and probabilistic models. Additionally, based on field, lab and numerical model tests by experts in suction caissons, the behavior of such foundations are studied under different loading conditions.

In the numerical analysis part first the different soil constitutive models are presented, then the model is validated based on a convergence analysis and an already calibrated model by [Thieken, 2013]. Later a numerical study is conducted to study the effects of different constitutive models, caisson geometries, loading types (uniaxial or combined loading), vertical loading on the response of the foundation.

Preface

The following report forms my final thesis for the master program Structural and Civil engineering. The thesis was written in collaboration with the University of Bologna, having a main supervisor in the home institution at AAU in Aalborg. The theme of the project is *Numerical modelling of foundations for offshore wind turbines*.

The author would like to show gratitude to the supervisors of the project, Johan Clausen, as well as to the supervisors at the University of Bologna, professor Laura Govoni, for facilitating my extended stay in Bologna and allowing me to use the resources of the university for my thesis.

Reading guide

Through the report, source references in the form of the Harvard method are applied. References from books, homepages or the like appear with the last name of the author and the year of publication in the form of [Author, Year]. They can furthermore appear with specific reference to a chapter, page, figure or table. All references are listed in alphabetical order in the bibliography, at the end of the report.

Figures and tables in the report are numbered according to the respective chapter. In this way the first figure in chapter 2 has number 2.1, the second number 2.2 and so on. Explanatory text is found near the given figures and tables.

Tamás Csaba Bogdán

Table of contents

| | |
|---|-----------|
| Chapter 1 Introduction | 1 |
| 1.1 Project overview | 3 |
| I Literature review | 4 |
| Chapter 2 Foundation types | 5 |
| 2.1 Gravity-based foundations | 5 |
| 2.1.1 Bearing behavior | 6 |
| 2.1.2 Construction and transport | 6 |
| 2.1.3 Installation and operating | 7 |
| 2.2 Monopiles | 8 |
| 2.2.1 Bearing behavior | 9 |
| 2.2.2 Transport | 10 |
| 2.2.3 Monitoring | 10 |
| 2.2.4 Installation, piling | 11 |
| 2.3 Steel frame structures | 14 |
| 2.3.1 Bearing behavior | 14 |
| 2.3.2 Fabrication and transport | 15 |
| 2.3.3 Installation and monitoring | 15 |
| 2.4 Suction caisson foundations | 16 |
| 2.4.1 History of suction buckets | 16 |
| 2.4.2 Bearing behavior | 19 |
| 2.4.3 Transportation and installation | 19 |
| Chapter 3 Design codes and guidelines for shallow offshore foundations | 23 |
| 3.1 Introduction | 23 |
| 3.2 Guidelines of practice | 24 |
| 3.2.1 Bearing capacity equations for deterministic and semi-probabilistic calculations | 25 |
| 3.2.2 Deterministic models | 27 |
| 3.2.3 Probabilistic methods | 29 |
| 3.3 Conclusion | 31 |
| Chapter 4 Suction caisson behavior under different loading conditions | 32 |
| 4.1 Monotonic loading | 36 |
| 4.1.1 Compression | 36 |
| 4.1.2 Tension | 38 |
| 4.2 Cycling loading | 41 |
| 4.2.1 Vertical loading tests | 41 |
| 4.2.2 Moment loading tests | 43 |
| 4.3 Summary of results | 44 |

| | |
|---|-----------|
| II Numerical analysis | 47 |
| Chapter 5 Model validation and soil constitutive models | 48 |
| 5.1 Soil constitutive models | 48 |
| 5.1.1 Mohr-Coulomb model | 51 |
| 5.1.2 Hardening soil model | 52 |
| 5.1.3 Hardening soil model with small strain stiffness | 54 |
| 5.2 Model validation based on convergence analysis | 56 |
| 5.2.1 Soil parameters | 56 |
| 5.2.2 Model set-up | 57 |
| 5.2.3 Failure mechanism analysis | 61 |
| 5.2.4 Mesh convergence analysis - rigid body elements | 64 |
| 5.2.5 Mesh convergence analysis - plate elements | 67 |
| 5.3 Model validation based on already validated model | 72 |
| Chapter 6 Numerical study | 74 |
| 6.1 Uniaxial loading with Mohr-Coulomb model | 74 |
| 6.2 Combined loading with Mohr-Coulomb model | 76 |
| 6.2.1 Constant vertical load (varying embedment lengths) | 77 |
| 6.2.2 Different V/V_{max} values | 78 |
| 6.2.3 Constant vertical load (varying lid diameters) | 80 |
| 6.2.4 Interpretation of results | 82 |
| 6.3 Combined loading using HS and HS small strains models | 82 |
| 6.3.1 Interpretation of results | 87 |
| Chapter 7 Conclusion | 88 |
| Bibliography | 89 |
| Appendix A List of Enclosures | 3 |
| Appendix B Model validation | 4 |
| B.1 Failure mechanism analysis | 4 |
| B.2 Convergence analysis | 4 |
| Appendix C Numerical study | 7 |
| C.1 Vertical loading, MC model | 7 |
| C.2 Combined loading, MC model | 9 |
| C.2.1 Different V/V_{max} values for different relative densities | 9 |
| C.2.2 Different V/V_{max} values for different aspect ratios | 10 |
| C.2.3 Combined loading using HS and HS small strains models | 13 |

Introduction

1

In the first chapter the current situation in the energy industry is explained with a focus on the reasons of the increasing popularity of the wind energy sector, thus the construction of offshore wind turbines and the prospects for offshore wind energy in the future. The introduction is based on [Houlsby, 2015] and [Houlsby, 2010]. The statistics and data mentioned in the chapter are according to [Schwägerl, 2016], a Guardian article which is based on an interview conducted with the vice president of Dong Energy, Benj Sykes.

Alternative, renewable energy sources are becoming more and more popular and the most desired sources of energy production. Having the most promise to reduce the effects of global warming by reducing the amount of CO_2 in the atmosphere, governments all over Europe are trying to exploit the possibilities that lie in renewable energy. Possible sources of renewable energy include wind, waves, currents, tides and solar energy. However wind and solar energy are “the only ones to be exploited on a commercial scale” [Houlsby, 2010]. As solar energy being dependent on the geographical location of the countries, wind power proves to be a more “reliable” and permanent energy source.

The wind energy sector became the most rapidly developing energy sector (the share of wind energy in the European Union’s electricity supply has experienced a 10% growth since the year 2000 [Schwägerl, 2016]) in the past few years for mainly two reasons; on one hand the production costs of wind energy have been dramatically reduced, mainly because of the standardized and more industrialized production of the turbines and other parts. According to [Schwägerl, 2016], one MWh costs between 50 and 96 euros for onshore wind and 73 to 140 for offshore wind, while the gas and coal prices range between 65 to 70 euros. On the other hand the European Union has been making a lot of effort to push away from fossil fuels thus invest in and facilitate renewable energy, especially offshore wind energy. As a result of this, the newly installed wind energy capacity was 13 GW in 2015, twice the amount of newly installed nuclear and fossil fuel combined [Schwägerl, 2016]. It can be said that wind energy has outcompeted coal-fired power plants, giving a headache to companies invested in fossil fuels. Besides the previously mentioned, an important factor in choosing wind energy over fossil fuels is that the former uses an unlimited resource, the wind.

These wind farms can either be completed offshore or onshore. The costs of onshore energy (wind) are significantly lower than of the offshore energy, being the main contributor the cost of the turbines’ foundations. By comparing the onshore and offshore foundations, it can be seen why; offshore foundations and structures have to [Houlsby, 2010]:

- support a taller tower (due to the water depth the height of the structure is significantly higher)
- withstand greater forces and moments coming from not just the wind but waves and currents as well
- be capable of constructed offshore

Despite the higher construction costs offshore wind turbines are gaining popularity as they can make use of the stronger winds (up to 40% stronger at sea than on the land [Schwägerl, 2016]), the transportation of the parts are easier on sea as ships can handle large cargo without the possibility of traffic jams and the noises of operation and construction as well as the landscape-ruining effects can be avoided. Among the disadvantages of offshore construction noise polluting should be mentioned as it can disrupt the natural habitat of the wildlife in the sea (for example the extreme noise during pile driving). Another undesirable aspect is the cost of construction and difficulty of maintenance of offshore structures (for example the maintenance of scour protection) as all the parts are located far away from the land or underwater.

As most countries are planning to cut down the amount of CO_2 emission and making efforts to achieve a bigger share of wind generated electricity of the total energy supply (a good example of such is Denmark or the UK, of which the former aims to switch the total energy supply to renewable energy by 2050), several wind farms have been constructed in the past years; North Hoyle, Scroby Sands, Kentish Flats near the shores of the UK, the Nysted and Anholt farms near Denmark, the Burbo Bank and its extension, with its 32 pieces of 8 MW turbines, just to mention a few and several upcoming project are due in the following years [Schwägerl, 2016]. According to Benj Sykes ([Schwägerl, 2016]), there is a debate if wind energy will be able to meet the demands or not, as the grid and energy storage infrastructure is not expanding (has not expanded) fast enough to store the surplus wind energy, which can put a halt to the rapid expansion of the wind energy sector in the future.

In some countries the non-renewable energy industries are trying to sabotage this transition from coal and nuclear energy to renewable energy, which also has a bad impact on the expansion and flourishing of the wind energy sector. If governments starts to finance projects to support new storage technologies and to expand the grid connections and capacity so that the increasing amount of electricity produced by the wind turbines can be taken up, then wind will be able to overcome other energy sources and cover most of the world's energy needs [Schwägerl, 2016].

As offshore wind turbine projects are being built further and further away from the shore, in deeper waters and with stricter requirements regarding regulations on underwater noise emission, the overall cost of the projects increase even though the aim is to decrease the cost of wind energy. To obtain such goals, new design considerations should be established to tackle the aforementioned challenges. To lower the costs of construction the rehabilitation of existing foundation techniques is needed, hence companies came up with the idea to use a more economical foundation type, suction cassions, the so-called bucket foundations, for offshore wind turbine plants as well.

It can be concluded that wind energy has a bright future and should not left neglected. Therefore civil engineers should focus on improving the already existing techniques, come up with more economical design codes and installation methods (suction caissons) for the foundations of such structures. In the following chapters a detailed discussion of the existing foundation types will be discussed, with special focus on the suction caisson foundation, which will be examined further in the project.

1.1 Project overview

The project consists of two main parts: a literature review and a numerical analysis part. The whole project revolves around one certain foundation type, namely the suction caisson or i.e. bucket foundation. This foundation method has a long history in the oil and gas industry, however the offshore wind industry has started to use it as well and is becoming more and more popular recently. This is mostly due to the easy and economical installation and uninstallation methods compared to the more complicated but also the most popular monopile foundation. This foundation has a shape of a bucket, closed on top and open at the bottom, consisting of skirt and lid elements. Additionally, the lid is connected to the substructure by stiffeners. In chapter 2.4. a more detailed presentation is given for the bearing behavior and installation of suction caissons.

The aim of the literature review is to give answers to the following questions:

- what are the most commonly used offshore foundation types and what are the differences between the bearing behavior and installation of those?
- what are the available design codes, guidelines for geotechnical engineers for suction caisson design?
- how do suction caissons behave under different loading conditions (monotonic and cycling loading - compression, tension and combined loading)?

The aim of the numerical study is to give answers to the following questions:

- what model size and element number should be use to reach convergence for the models?
- is the constructed model able to reproduce results of a previously validated model?
- how is the caisson response affected by changes in the geometry (both for uniaxial and combined loading) and vertical loading rate (different V/V_{max} values for combined loading)?
- how is the caisson response affected by using different constitutive models? In a broader sense - what kind of precision can be obtained using more time-consuming models?

Part I

Literature review

Foundation types 2

In the following chapter the most commonly used offshore foundations are to be presented and compared with a focus on the technologies, installation procedures, bearing behavior, transportation methods and loading conditions. Special focus will be given to the suction caisson, in other words bucket foundation, in this chapter as the rest of the thesis will revolve around problems related to the suction caisson. Given the huge amount of already built monopiles and the fact that monopile is the most commonly used and the most popular form of foundation so far, a detailed description of it can be found in this chapter as well. The contents of the chapter is based on [Lesny, 2010],[Gourvenec, 2011],[Czapp, 2014] and [Józsa, 2014].

The concepts of foundations used nowadays for offshore wind turbines were borrowed from the oil and gas industry [Lesny, 2010]. These foundations (see: Fig.2.1) include: steel framework structures such as jacket or tripod foundations, the most popular and widely used monopiles, gravity based structures and suction bucket foundations. Depending on the water depth, load and soil conditions, the foundations shown in fig. 2.1 can be chosen for the different design cases. Flexible guyed structures which facilitate more favorable dynamic behavior and screw piles which can dramatically increase the achievable tensile capacity are not going to be mentioned in detail.

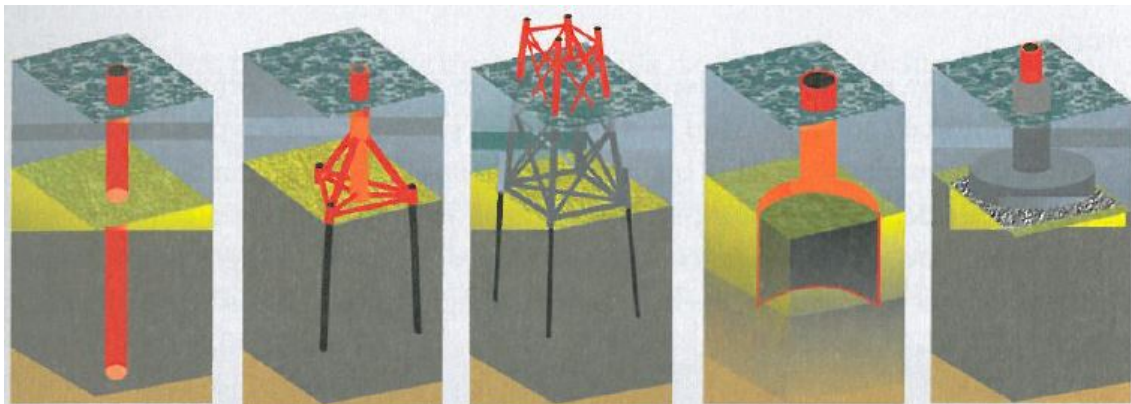


Figure 2.1. The most commonly used foundation types for offshore wind turbines. From left to right: a, monopile b, tripod c, jacket foundation d, suction caisson (bucket foundation) e, gravity based foundation [Lesny, 2010].

2.1 Gravity-based foundations

Shallow foundations such as gravity based structures are mostly used in not too deep waters where the soil conditions are favorable, meaning either highly OC clay or dense sand is encountered under the seabed, as deep, piled foundations are not required and not economical for soils able to provide enough capacity. The classical gravity based foundation can be made of reinforced concrete, steel or a composite materials. They rely on their footprints' size, high volume and weight to withstand the horizontal and moment

loading coming from the environmental effects and to ensure the required floating stability. Ballasting is also needed so that the foundations can be sunk later. For this sand, gravel, water or concrete can be used [Lesny, 2010; Józsa, 2014].

The height/diameter of these foundations range from 10 to 19 m in water depths of 3 to 8 m. However way bigger gravity foundations have been constructed before in the oil and gas industry with heights starting at 70 m and footprints at 50×50 m often in a region of 500 m below water level [Gourvenec, 2011].

2.1.1 Bearing behavior

The loads from the upper structure are transferred into the seabed at the bottom of the foundation by normal and shear forces. A very important factor in the design of gravity based structures is the presence of heave forces between the bottom of the foundation and the seabed. These heave forces become important in intermediate to deep waters therefore gravity based foundations should be used in shallow waters only. Skirts are not only increasing overall capacity of the foundation against uplift, horizontal, vertical and overturning moments but also against tension loads [Gourvenec, 2011].

Because of the aforementioned and to avoid excessive scouring, gapping is not allowed without the use of skirts for gravity based foundations. In order to achieve this the seabed must be cleaned of soft layers and stones. A bedding layer can also be used or if needed the gap can be grouted as well. Because it is harder and more expensive to prepare the contact area of the upper soil in offshore environment, the use of skirts are more preferred. The skirts has to be designed so that a sufficient embedment is reached by self weight penetration only, similar to the suction caisson installation. The usual length of such skirts are from 0.5 to 30 m, depending on the softness of the underlying soil and size of the upper structure [Gourvenec, 2011]. The mentioned preparations are even more important for ballasted structures, which lie on the seabed without any embedment and even more susceptible to the scouring and excessive shearing under themselves [Lesny, 2010].

2.1.2 Construction and transport

Gravity based foundations can be constructed fully or partly in dry docks, floating docks, on a floating pontoon or in the so called earth docks, which are excavated sites near the seashore, out of which the foundation is towed out after the removal of the protective dam between the excavated site and the sea [Lesny, 2010].

In order to transport these structures from the construction site to their ordered place first the construction dock needs to be flooded so that the structures can be towed out by tow boats. If the structure is non-floating, barges can be used as means of transportation. According to [Wagner, 1990], the towing stability, meaning the hydrostatic and hydrodynamic stability, needs to be ensured during transportation. Hydrostatic floating stability is ensured if the floating body has the ability to right itself after leaning, tilting from the self-weight and buoyancy. When verifying hydrodynamic stability, the possibility of resonance must be checked. [Lesny, 2010] suggests to increase floating stability by ballasting but making sure that the ballast isn't placed too low as it not enhances but decreases overall floating stability.

2.1.3 Installation and operating

As mentioned before in section 2.1.1, in some cases proper seabed preparation is indispensable. The soft top layers and rocks need to be removed, the seabed surface needs to be leveled and aligned, for some cases a base layer needs to be placed and even preloading or compaction can be necessary. Similar to slope and retaining wall design, geotextile or coarse base layers can be used which act as additional drainage to accelerate consolidation.

After the seabed is aligned, the structure is positioned with the help of GPS by anchors, hawsers or winches placed on the structure and the tow boats. Another possibility is to use pontoons. The structure is anchored to the pontoons which pull the structure in the desired position [Lesny, 2010].

Then comes the sinking process. Sinking can be controlled by ballasting or flooding of the caisson cells. The number, the size and layout of the caisson cells need to be designed so that the sinking speed is optional and the structure touches the upper layer of the seabed gently, avoiding any local stress peaks at the bottom of the foundation [Lesny, 2010]. This is essential for concrete structures which lack sufficient tensile capacity, as tension in the concrete caused by the stress peaks can severely damage or even break them. Therefore the distance between the seabed and the structure is continuously monitored by echo sounders. It is also very important to begin the sinking process in favorable weather conditions to avoid unpredictable movement and thus unwanted damage of the structure.

According to [Lesny, 2010], the following need to be monitored and measured during installation:

- the water pressure to control the depth and ballast
- the loading on the skirts
- the normal stress on the base
- and the tilting of the structure.

After the structure is placed the gap between the base and the seabed can be grouted if necessary and the caisson cells can be filled with gravel, sand or other materials to push the water out [Lesny, 2010].

As there is a lack of experience in the construction of offshore energy plants and the prediction of the long term soil behavior (based on boreholes, CPTs) and the actual design methods are not reliable, monitoring during the operation of such structures are essential. Regular examinations of the foundation and the scour protection are important. The monitoring part is part of the design during operation, obligatory and needed to obtain certification [Lesny, 2010]. During long-term monitoring foundation tilting, displacements and settlements, dynamic movements, normal stresses at the base of the foundation and pore water pressures need to be measured and monitored [Lesny, 2010].

2.2 Monopiles

If gravity based foundations can't be used due to the bad soil conditions (reduced capacity) and/or high loading caused by excess water depth, then the preferred choice is the monopile foundation. These steel pipe piles are embedded in the ground and extend above the seawater level. As the verticality is not ensured during pile driving (unlike installation of suction caissons), a transition piece is used on the top of the monopile to allow alignment between the upper structure and the monopile, in between which the gap is grouted.

Monopiles have become the most popular foundation types for offshore wind turbines [Lesny, 2010]. There's only experience with monopiles built in shallow water and piles subjected to moderate wave loading [Gourvenec, 2011]. As deeper water and thus higher wave loads would result in the need of bigger diameter and embedment depth, using a single pile foundation in deep water is usually not the most economical solution. As monopile foundations for wind turbines are usually very slim structures, meaning that the vertical forces are small compared to the horizontal forces, the governing load is the overturning moment at the top of the seabed. As a result of this, monopile foundations are short and stubby compared to the piles used for jacket structures, usually with a diameter around 4 m [Gourvenec, 2011]. Some examples for the used diameter/embedment length for various water depths and soils can be seen in Table 2.1.

Table 2.1. Monopile foundation dimensions for existing offshore wind energy plants [Lesny, 2010].

| Location | Soil type | Water depth [m] | Diameter/ embedment length [m] | Installation |
|-------------------------|-------------------------------|-----------------|--------------------------------|----------------|
| Lely/NL | clay/sand | 4 to 5 | 3.7/21 to 24 | driven |
| Dronten/NL | - | 1 to 2 | - | driven |
| Bockstigen/SWE | rock | 6 | 2.1/21 | drilled |
| Utgrunden/SWE | rubble/rock | 7 to 10 | 3/19 | driven |
| Blyth/GB | rock | 6 | 3.5/15 | drilled |
| Yttre Stengrund | rock | 7 to 9 | 3.5/8.5 | drilled |
| Horns Rev/DK | sand/rubble | 6 to 14 | 4/21.7 to 24.3 | driven |
| Samso | soft clay/rock | 11 to 18 | 4.5/18 to 26 | driven |
| Arklow Bank/IRE | sand | 2 to 5 | 5.1/32 | driven |
| North Hoyle | sand/clay | 5 to 12 | 4/33 | driven/drilled |
| Scroby Sands/GB | sand | 2 to 10 | 4.2/to 31 | driven |
| Kentish Flats/GB | sand/soft clay | 5 | 4/28 to 34 | driven |
| Barrow/UK | sand/clay/mud-stone/siltstone | 15 to 20 | 4.75/ 49.5 to 61.2 | driven/drilled |
| OWEZ/NL | sand | 18 | 4.6/30 | driven |
| Burbo/GB | - | 1 to 8 | 4/35 | driven |
| Q7-WP/NL | sand | 19 to 24 | 4/54 | driven |
| Lynn & Inner Dowsing/GB | - | 6 to 13 | 4.74/- | driven/drilled |

The monopile can either be a conventional, driven pile or a drilled/grouted pile. The more favorable and most commonly used is the driven pile, although grouted piles are

more desired in hard subsoil; such as in rock and in calcareous, cemented sediments (the Australian shoreline and the Middle-East is a good example for the use of grouted piles) [Gourvenec, 2011].

2.2.1 Bearing behavior

As mentioned before the loading is mainly transferred into the ground by lateral bending. It is because a distinct feature of offshore structures are the loading conditions, meaning high horizontal forces and overturning moments compared to the vertical forces acting on the seabed level. As a result of this the upper layer of the soil is very important for the bearing capacity of foundations, if necessary the weak upper layer can be removed and replaced. The pile can encounter layers that doesn't have sufficient capacity (soil strength). In such cases the pile length needs to be increased until sufficient resistance is achieved and the displacements and rotations are acceptable in the serviceability limit states [Lesny, 2010].

Figure 2.2 shows the pile response to the axial and lateral loading. It can be seen that the axial resistance consists of two components: the base (q_b) and shaft (τ_s) resistance, while the lateral resistance comes from the normal and shear stresses (P , earth pressure) acting on the pile shaft. Lateral failure of the pipe can occur in two ways [Gourvenec, 2011]:

- geotechnical failure, meaning that the ult. horizontal soil resistance is exceeded causing the pile to fail as a rigid body or
- the pile fails while bending causing a structural failure.

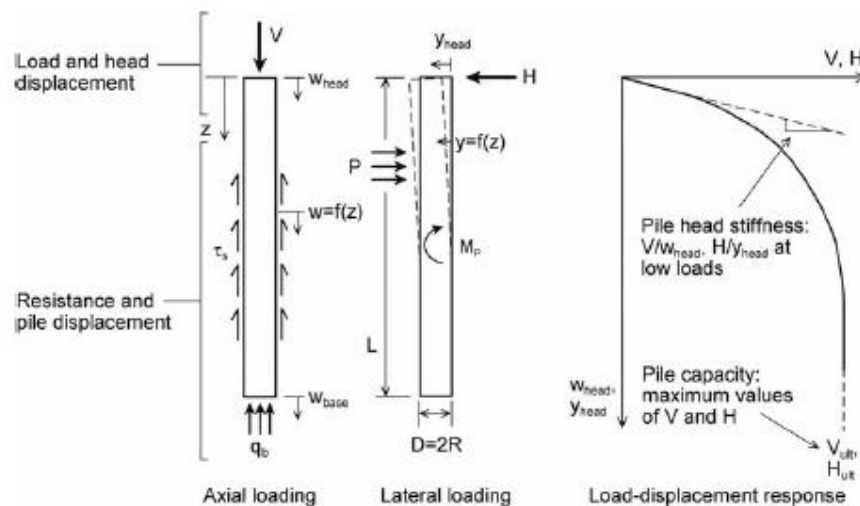


Figure 2.2. Pile response to both axial and lateral loading [Gourvenec, 2011].

During the design of pile foundations the followings might need to be considered [Gourvenec, 2011; Czapp, 2014]:

- Installation, which is depending on the piling method; for driven piles: drivability (detailed description can be seen in Chapter 2.2.4) - the control of damages and driving stresses, checking the possibility of buckling and directional stability; for

grouted driven piles: thermal effects and loss into formation; for drilled and grouted piles: the hole stability needs to be ensured and checked

- Axial capacity and response including the analysis of group effects, overall structure stiffness, and the analysis of the foundation's performance (cyclic loading - stiffness degradation) under axial cyclic loading.
- Lateral capacity and response ($p-y$ analysis, group effects, short and long pile failure mechanisms) including performance analysis under lateral cyclic loading.
- Seismic response
- Scour protection
- Local seabed stability analysis (landslides, seabed movements)

It is important to note that there is different behavior observed for short ($L/R < 2$) and long ($L/R > 4$) piles. The former moves as a rigid body around a point of rotation when laterally loaded giving approximately linear or constant soil reaction (cohesionless or cohesive soils), while the latter results in a more complicated, non-linear soil reaction, while behaving in a more flexible way [Czapp, 2014]. As most of the piles in the offshore industry have a long and slim shape, the latter behavior is of importance. The design of piled foundations are different than of the shallow foundation as it is really hard to describe the exact failure mechanism of piles (specifically at the based of the piles). As a result of this the formulas linking soil strength and pile capacity are more empirical and non linear analyses for the strength, stiffness of piles (especially in layered soil) often demands numerical analysis due to the varying soil properties across the layers [Gourvenec, 2011]. The insignificant interaction between vertical capacity and horizontal loading (and vice versa) somewhat simplifies the design of piled foundations compared to the shallow ones. The reason for this lies in the size and slender shape of the foundation; the horizontal load is absorbed in the upper parts of the pile while that vertical load is resisted around the pile base [Gourvenec, 2011].

2.2.2 Transport

The prefabricated steel pipe piles are towed to the construction site on transport barges or in some cases the open ends are sealed and the pile(s) are floated to the installation site. Arriving at the installation site, floating cranes are used to lift the piles and position them. Another method can be a combination of driving and drilling with the support of vibration or flushing [Lesny, 2010]. The detailed explanation of the piling methods can be read in Chapter 2.2.4.

2.2.3 Monitoring

As monopiles are considered relatively flexible structures compared to other foundation types, the control and monitoring of such structures under operation is crucial. Especially the monitoring of deformations, such as the measurement of inclination as too much tilting can have an effect on the whole structure's dynamic behavior. On the other hand the deformations of the pipe wall needs to be monitored and controlled by strain gauges. And as mentioned before, scour protection needs to be established and checked continuously throughout the lifetime of the structure as insufficient protection can impair the soil capacity [Lesny, 2010].

2.2.4 Installation, piling

Driven piles

The most popular offshore foundation is the open-ended, driven displacement (displacing the soil, rather than removing it) pipe [Gourvenec, 2011]. The piles are driven open-ended, so that the soil can flow into it to form a 'plug'. Nowadays these pipes are installed using modern underwater hydraulic hammers, however in the past diesel, compressed air or steam driven hammers were used as well. Unlike in deep water, in which piling requires underwater hammers, in shallow waters these hammers can still be used, as they can be mounted on pile extensions (followers) and operated above the water level [Lesny, 2010].

To prevent the damage of the pile head, a so-called pile helmet is used to protect the head by distributing the energy evenly. Another important design consideration to prevent damage is to choose the piling equipment so that the ratio of the hammer to pile weight is at least 1:1, but 2:1 is more favorable [Lesny, 2010]. Choosing the hammer accordingly, the transfer of the generated kinetic energy to the pile head is smooth. The previously mentioned followers don't have to be used in deep water piling.

To determine the energy (impulse) needed to drive the pile into the subsoil, a driving analysis is conducted so that the suitable equipment can be selected [Czapp, 2014]. The drivability study is an important part of the design process to check if pile refusal might be encountered or not. This study is based on the Smith model, which depicts all the pile components as an array of lumped massed and springs and is based on the one-dimensional wave propagation theory [Lesny, 2010]. The base resistance and shaft friction contribute to the penetration resistance, both of which consists of a static and dynamic part. The former is triggered by the self weight of the model, while the latter considers the velocity proportional damping taking place in the soil from the driving. To simulate the dynamic loading part more advanced, numerical softwares were developed, of which the most widely used is GRLWEAP [Gourvenec, 2011; Lesny, 2010].

The drivability study has to make sure that [Gourvenec, 2011]:

- the pile wall is not failing under static load (bending caused by the weight of the hammer),
- and that the fatigue capacity of the pile is not depleted.

According to [Lesny, 2010], in the analysis either the available driving capacity needs to be compared with the driving resistance or the maximum number of impacts allowed is calculated for 25 cm penetration. Drivability is mainly affected by the pile's base resistance, in addition to the wall thickness and the cross-section of the steel pipe. Larger cross-section results in higher driving performance, but combined with a high base resistance, it might be more beneficial to reduce the size of the cross-section so that the driving resistance can be reduced [Lesny, 2010]. [API, 2000] recommends to use a minimum wall thickness defined by the following formula to prevent buckling of the pipe [Det Norske Veritas]:

$$t = 6.35 + D/100 \tag{2.1}$$

,where both D and t are in mm. Complications that can emerge during the driving procedure [Lesny, 2010]:

- If the soil is plugged (plugging phenomena) when driving an open pile pipe, increasing the size of the cross-section will result in the increment of the driving resistance and thus probably will cause the pile to fail. This phenomena will most possibly happen if the pile passes from a stronger to a weak material (from dense sand to clay).
- Should the self-weight of the pile exceeds the allowable soil stresses, the pile can sink.
- The effect of soil-setup, a consolidation process that leads to higher adhesion of the soil to the pile, only occurring in cohesive soils and mainly happening when the driving process is put to a halt for some moderate amount of time (higher driving force is needed to continue the installation).
- High stressing at the bottom of the pile in non-cohesive, cemented soils or rocks, leading to a significant increase of the base resistance.

Drivability can be impaired by refusal or sufficient damage of the pile tip [Gourvenec, 2011]. The former happens when the penetration resistance exceeds the capacity of the hammer, meaning that the design depth can not be reached. Two solutions are available in such situations: a higher performance can be used or the accumulated soil inside the pile can be removed, for example by flushing, resulting in reduced mass and penetration resistance (the possibility of piping failure and the loss of bearing capacity at the tip of the pile must be checked). Should these methods don't help, a pipe with a smaller diameter can be chosen [Lesny, 2010]. Damage or collapse of the pile tip may result in reduced capacity, refusal or failure of the pile. As mentioned before, driving in cemented soil or rock can generate high stresses at the tip and low stresses along the shaft, thus drilling is the preferred construction method in such soils [Lesny, 2010].

The problems caused by acoustic noise can't be overlooked in the design. Noise levels generated by the hammers are up to 200 dB, which can pose a risk to the marine environment, especially to the ones using biosonars (dolphins) for navigating. This threat can be reduced by the use of vibrating hammers or bubble curtains. The mentioned problem can lead to delayed construction times because it can restrict the allowed number of simultaneously driven piles [Lesny, 2010].

Drilled piles

As discussed before, certain soil environments can demand the use of drilled pipes. These pipe "systems" usually consist of a steel tubular pipe placed in a pre-bored hole, which is then filled with concrete (grouted) and named soil replacement piles.

The installation procedure can be seen in Figure 2.3, and consists of the following phases [Gourvenec, 2011]:

1. A primary, standard steel pile is driven through the soft sediments, which guides the rotary drill, inhibits the collapse of the hole (necessary for unstable boreholes) and acts as the foundation pile later.
2. Then with the use of a rotary drilling rig a hole is excavated to the designed penetration depth.
3. After placing a steel (insert) pile in the hole, the area between the pile and hole is grouted with the continuous lifting of the drilling rig.

Being a quite expensive and time consuming piling method is another reason for driven piles being preferred to the grouted ones. The design of drilled piles should consider [Gourvenec, 2011]:

- The stability of the hole: if the hole needs support or not.
- The need for primary pile.
- The grouting procedure.
- The grout pressure: higher grout pressure ensures that the space around the inserted pile is continuously filled (increased shaft resistance), but too much grout pressure can cause fracture in the formation.
- The base stability: excess flushing or soft drill cuttings fall to the base can impair base stability.

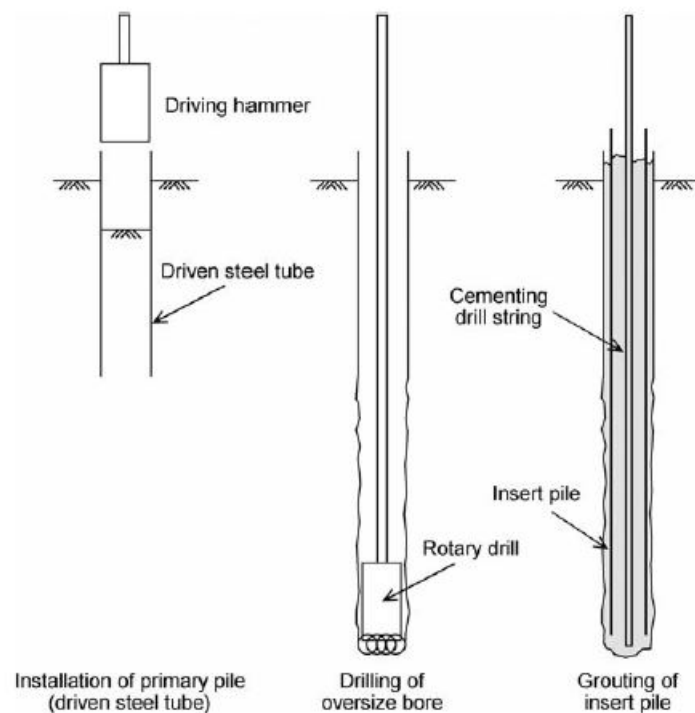


Figure 2.3. The installation phases of a bored and grouted pile [Gourvenec, 2011].

2.3 Steel frame structures

Steel frame structures are highly customizable, allowing different kinds of structures to be fabricated. The most common, already existing types include: jackets, tripods (3 inclined legs welded at the top), tetrapods (4 legged structures) or even tripiles (main connection node can always be found above the water level and the legs are vertically positioned). Anchoring can be done with piles and shallow foundations including suction caissons as well (see: chapter 2.4). As it can be seen in Fig. 2.6 the outer legs are often inclined to reduce reaction forces and to boost vibration behavior. Advantages of these structures include lowered overall mass compared to gravity-based foundations, reduced loads and better applicability in deeper waters and in thick soft clay layers [Lesny, 2010].

Based on research conducted by [Lesny, 2010] the first demonstration project for jacket supported wind turbines was called project Beatrice, and two 5 MW turbine was installed on steel framed jackets in approximately 45 m deep water in 2007. Following this 6 tripod and 6 jacket supported turbine were installed at the Alpha Ventus test site in 2009. A tripile has been also installed as part of a demonstration project in 2008 near Hooksiel, Germany.

2.3.1 Bearing behavior

The elements of the frame structure need to withstand alternating tensile and compression loadings caused by the bending moments acting on them. In case of pile supported jackets the loading is transferred in the classic pile way, by shaft friction and base resistance. For tension piles it is by the former, for compressed piles it is by both. This behavior can be seen in Figure 2.4. Same as for piles, the horizontal loads are carried by lateral bending of the piles [Lesny, 2010].

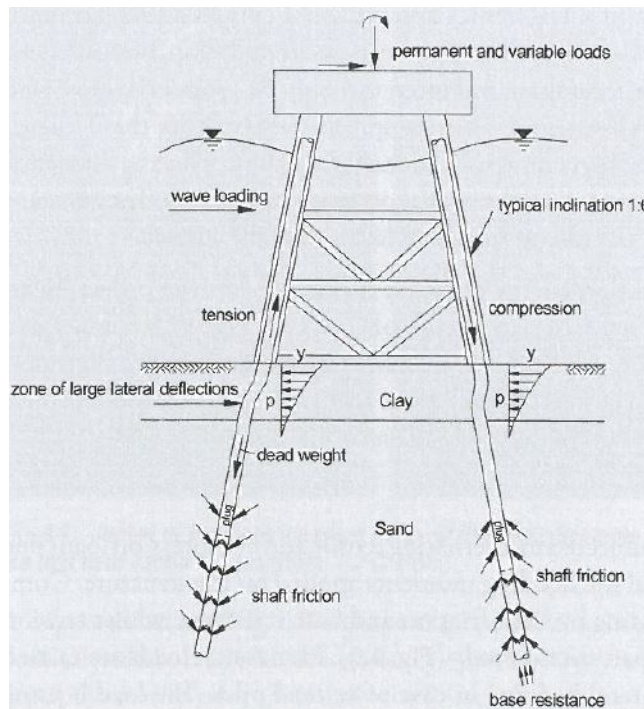


Figure 2.4. Behavior of pile founded jacket structures under operation [Lesny, 2010].

In addition to the problems with the bearing capacity due to tensile loading, the continuous altering of tension and compression results in a decrease of the soil stiffness (see chapter 4). Suppression of the tensile forces can be necessary and according to [Houlsby, 2010], tension can be avoided by either increasing the overall deadweight of the structure (additional ballasting), or the footings can be placed further away from each other.

2.3.2 Fabrication and transport

The steel frame structure is completely fabricated on land. Three or four sided jackets are the most common in commercial use. After the narrower sides are made lying on the ground, they are lifted, positioned vertically and then cross-beams and stiffener are used to stabilize the frame. As the nodes are subjected to high loading, they can be prefabricated (cast or welded) and placed afterwards to ensure excellent load transfer [Lesny, 2010].

Following fabrication, the frames are towed to the design sites on barges or by self-floating in a laid-down position. In case of the latter flotation aids are required. Tripods are usually transported in a standing position for which floatability need to be ensured by buoyancy aids [Lesny, 2010].

2.3.3 Installation and monitoring

The installation methods based on [Lesny, 2010] for smaller and larger frames are as follows: The smaller frame structures in shallow water are lifted from the barges with the cooperation of floating cranes and the controlled flooding of the flotation aids and legs. The structure is then placed on the seabed with further flooding, positioned by the crane. The barge stability has to be ensured and controlled during the installation process by flotation aids. Larger frames has to be launched off the barge. During the launching process the frame is pushed forward by a hydraulic press, after which a tilting mechanism turns the frame into the water. Then the structure is erected and placed on the seabed in the same way as smaller frame structures.

Similar to jackup rigs, the structures are put on mudmats to ensure temporary stability on the seabed. The permanent piles are driven at the same time for smaller steel structures to prevent eccentricities, as for larger structures, the driving of two diagonally opposite pile is preferred to achieve a better control of loads during installation [Lesny, 2010].

Similar to gravity-based foundations regular monitoring of the inclination and displacement of the foundation elements, as well as the monitoring of scour protection is necessary [Lesny, 2010].

2.4 Suction caisson foundations

As it was mentioned in the introduction, building in deeper waters demands a bigger project budget, which is not convenient given the fact that the aim is to decrease the overall prices of offshore wind turbine projects. Therefore the prices of construction need to be decreased. With the use of suction caissons, in other words bucket foundations, the overall construction time and construction costs can be drastically lowered thanks to the unique installation technique.

The suction bucket in principle is an upturned bucket steel cylinder, closed on top and open at the bottom, embedded in the seabed (see Figs. 2.5 and 2.8). The foundation can be perceived as a combination of the key features of a gravity based foundation and a monopile. Based on the geometry and the loading conditions it can correspond either to a shallow foundation, a pile or an anchor. The installation method makes the structure really unique. After utilizing the gravity-facilitated lowering of the bucket into the seabed, negative pressure (suction) is created inside the caisson skirt which causes the foundation to sink to the design depth.

2.4.1 History of suction buckets

Suction bucket foundations have a more than 30 year old history, most of them used as anchors specifically for floating structures for the offshore oil and gas industry. According to [Wikipedia, 2017], the first, relatively small diameter caissons (12 pieces) were first used in the North Sea at the Gorm Field in 1981, commissioned by Shell in a water depth of 40 m. Several tests and field investigations have been conducted on the first ever built suction caisson-supported jackets at the Draupner E platform in 1992 which laid down the foundation of suction bucket design [Gourvenec, 2011]. The caissons proved to live up to expectations and 18 years later in the Gulf of Mexico in 1999, part of the Diana project suction caissons 30 m high and 6.5 m in diameter were installed almost 1500 m deep. The project counted as a technology breakthrough of the 20th century. A great example for the cost effective attribution of suction buckets is the construction of the Snorre-A platform in the Norwegian Sea. According to the design, piles of 90 m should have been used as foundation for the tension-leg platform, but as a result of disadvantageous soil conditions, suction buckets with a skirt length of only 12 m has been installed instead of the piles. Statistics from 2002 show that 485 caissons have been planted worldwide in more than 50 different locations [Wikipedia, 2017]. According to [Universal-foundations, 2017], more than 2000 suction-technology based foundations have been completed by 2016, in the offshore and oil industry.

Monopods

The concept used in the offshore oil and gas industry is quite new as foundation for offshore wind turbines. Two types of suction buckets are being made available for wind turbines; monocaissons by Universal Foundations and suction jackets by DONG Energy. There are a few already built examples of wind turbines with suction buckets [Universal-foundations, 2017][4C-offshore, 2016][Lesny, 2010]:



Figure 2.5. Monobucket foundations used in the Horns Rev 2 project [Universal-foundations, 2017].

- The very first prototype has been built in 2002, in Frederikshavn, Denmark, as a support for a Vestas V90 3MW wind turbine. The buckets had a diameter of 12 m and a height of 6 m weighing a total of 135 tonnes. Tests have been conducted on the prototypes and they are still being monitored so that the collected data can be analyzed and further researched.
- The Horns Rev 2 project consisted of the installation of a suction bucket for a mobile meteorological mast in 2009. The project was a test for a floating installation and proved the precision that can be achieved by the suction installation method; the bucket was installed 0.1 degree from true vertical position. As it was no longer needed, the structure has been removed in 2015.
- In 2011 two meteorological masts has been installed at the Dogger Bank's wind farm near the UK with suction bucket foundations. The project proved that the foundation can live up to the expectations by achieving cost and time savings, as well as noise reduction goals (see Fig. 2.5).
- In 2014 trial installations of suction buckets have been conducted at three different offshore wind farms (Dogger Bank, Dudgeon, Hornsea) near the shores of the UK. 29 installations have been executed in 24 days. The trials were conducted to assess suction bucket performance in soils with different characteristics, verticality, penetration, and to monitor forces and stresses along the skirt of the foundations. The results were positive and excellent, further proving the suction caissons' ability to replace conventional monopile foundations. Two different buckets have been used with a diameter-skirt length of 8/6 and 4/6.



Figure 2.6. Installation of suction bucket jackets at the Borkum Riffgrund 1 project area [4C-offshore, 2016].

Spread-out structures (jackets/tripods/tetrapods)

Another version of the suction bucket foundation is a spread-out truss structure placed on either three (tripod) or four (tetrapod) suction buckets. The suction bucket jackets behavior is similar to the pile jackets': the caissons are alternately loaded; some of them in tension, some of them in compression. The detailed behavior of jacket structures can be read in chapter 2.3.

Suction bucket jacket(s) has very little history: based on [4C-offshore, 2016], there is only one example of such structures so far. The jacket was built in 2014 at the Borkum Riffgrund 1 project in Germany as a support for a Siemens SWT-4.0-130 turbine by DONG energy. The designers were trying to create a challenging installation situation, and as previously trial tests on caissons were mainly conducted in clay environment, they decided on a location where dense sand is the underlying soil to improve the evaluation of the concept. Some specs of the structure are: the total weight of the structure including the buckets was 752 t with a total height of 56.6 m and bucket dimensions of 8x8 m [4C-offshore, 2016]. The suction bucket jacket foundation can be seen in Figure 2.6. Based on the positive and satisfying test results on the Borkum Riffgrund 1 project, suction bucket jackets are to be used in future projects as well, namely: the Hornsea Wind Farm, expected to be completed in 2020, and the Aberdeen Bay Wind Farm projects [Wikipedia, 2017].

2.4.2 Bearing behavior

As mentioned before it is essential to mention that the behavior of monopods and tripods/tetrapods are quite different, they resist the loads in a quite different way. Monopods resist the overturning moment caused by the winds and waves directly, while tripods/tetrapods resist the moment loading by a so-called push-pull action, meaning the alternation of tension and compression in the caissons Houlsby [2010]. As a result of this response of monopods subjected to moments and response of tripods/tetrapods subjected to cyclic loading are of main importance.

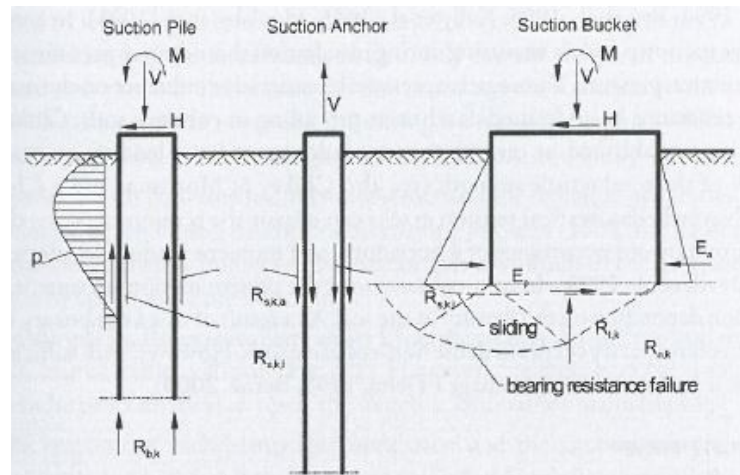


Figure 2.7. The bearing behavior of suction buckets [Lesny, 2010].

Whether monopod or a spread-out structure is the subject of the question, bucket foundations behave like a combination of the classical gravity-based and pile foundation or as suction anchors, as it can be seen in Fig.2.7. Meaning that the loads are transferred by shaft friction and base resistance or by self weight and shaft friction (suction anchor). Horizontal loads and overturning moments are converted into the seabed by lateral bedding [Lesny, 2010].

A similar behavior of suction buckets to gravity based foundations is that the base area is subjected to load transfer as well, but a huge advantage of the former is that the base level is located embedded, deeper in the subsoil and is used for load transfer hence the increased safety against sliding and bearing capacity failure. But if full contact is assumed between the bucket and the soil in the calculations, grouting may be necessary [Lesny, 2010].

Even though the base area is protected from erosion because of the deeper penetration, protection against scour during the operation must be implemented, especially if the bearing capacity of the upper layers has been used in the calculations [Ibsen, 2010].

2.4.3 Transportation and installation

The real uniqueness and biggest advantage of the suction caissons lies in the excellence of their installation process. Unlike for all the previously mentioned foundation methods, no heavy duty equipment is needed for the suction buckets, except a pump with sufficient capacity. The complicated preparation of the seabed can be neglected as well, so no divers

are needed. All of these resulting in significantly decreased installation times and cost of installing. The spread-out structures including the buckets are made onshore and floated to the place of sinking. The buckets can be sealed and operate as floats or pontoons can be used as flotation aids [Lesny, 2010].

The installation procedure according to [Lesny, 2010] and [Ibsen, 2010] is as follows: after the caisson is placed on the seabed, the uncontrolled self penetration phase, caused by the gravity, is utilized. To utilize the most of the self penetration controlled ballasting can be used. It is important to place the skirts perpendicular to avoid the local overstressing of them. The control of the sinking speed is important as well, as being too slow can make the perpendicular positioning even harder, while being too fast prevents the water to escape between the skirts, resulting in excess erosion of the seabed around the them.

The second phase is when controlled suction is created inside the bucket by the continuously pumping the water out of the bucket. The phenomena created by this process can be seen in Fig. 2.8. An explanation of the figure based on [Lesny, 2010] is the following; the phenomena is different in cohesive or non-cohesive soils. In non-cohesive soils the applied suction generates water movement from the outside to the inside of the bucket which leads to the drastic reduction of the effective stresses inside the bucket including the base area and the reduction of the friction on the inner skirt wall (friction is only reduced in the presence of high hydraulic gradients). The suction also creates a hydrostatic pressure difference, which is of inferior importance for non-cohesive soils. However with cohesive soils a no-flow rule develops, meaning that the only "driving force" is the hydrostatic pressure difference, hence it is of major importance for cohesive soils [Lesny, 2010].

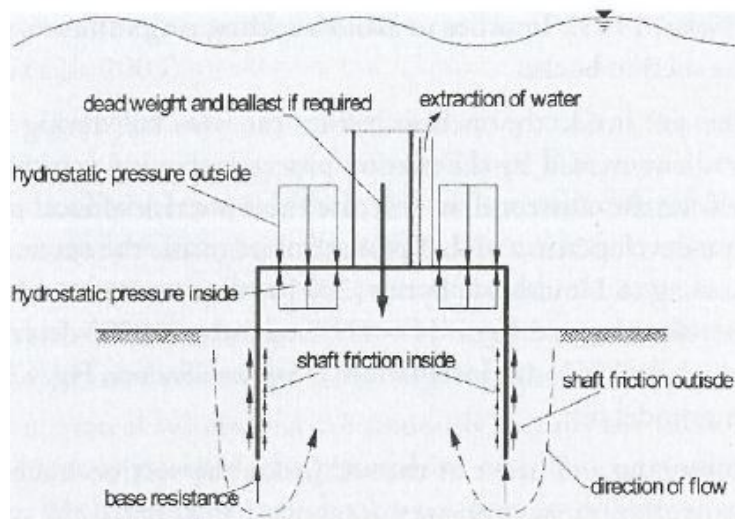


Figure 2.8. Behavior of suction buckets during installation [Lesny, 2010].

Transition piece is not required as the virtual alignment of the foundation is fully controlled during the installation. As the foundation doesn't require heavy duty equipment, the installation can be considered noise-free [Lesny, 2010].

Failure modes and problems during installation

In non-cohesive soils the downward flow created by the applied suction on the outside of the skirts results in the increase of vertical stresses (compaction), which leads to the increase of shaft friction and horizontal stresses as well. The horizontal stress difference between the two sides of the skirt raises the possibility of buckling caused by improper positioning of the bucket on the seabed and manufacturing imperfections in the skirts, against which ring stiffeners are placed on the inside of the skirt [Lesny, 2010].

Another way of failure is when the soil fails inside the caisson during the installation. This can happen if the hydraulic gradient generated by the suction outstrips a certain critical gradient. Eventually the local piping channels can cause a global failure of the soil inside the bucket [Ibsen, 2010]. The phases of such failure mechanism can be seen in Fig. 2.9. According to Houlsby and Byrne (2005b) this limits the maximum attainable penetration depth to approximately $H \approx D$. To avoid loosening and forming of heave plugs the suction pressure need to be controlled carefully during installing [Lesny, 2010].

In cohesive soils soil failure take place if the undrained shear strength of the layer is smaller than the suction applied. In this case the base area is compromised in which a soil plug detaches. The phenomena is called plugging and can also happen when adhesion between the skirts and soil is too big resulting in caisson refusal (no further penetration)[Ibsen, 2010].

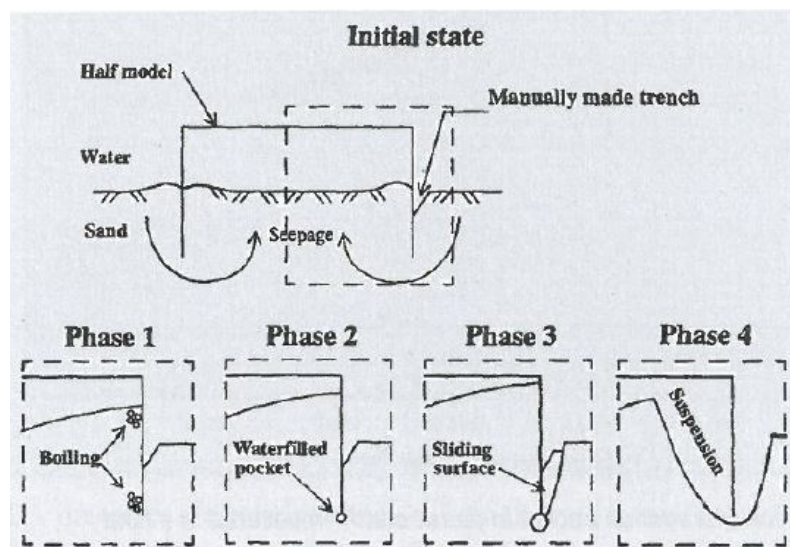


Figure 2.9. Phases of global piping failure inside the bucket on model tests conducted by Vangelsten (1997) [Lesny, 2010].

Problems can arise during installation in layered soils, in particular when a cohesive layer is penetrated after a non-cohesive layer as because of the no-flow rule there is no other pressure component present but the hydrostatic pressure difference to aid penetration, which might not be enough for the caisson to reach the design depth [Ibsen, 2010].

To summarize installation failures can occur due to:

- insufficient pump capacity,

- buckling of the steel skirts,
- piping failure in non-cohesive soils due to the rapid increase of the applied suction (hydraulic gradient exceeds the critical gradient) or
- plug heave failure in cohesive soils.

Monitoring

During installation several things needs to be monitored [Lesny, 2010]:

- the applied suction pressure,
- the water quantity pumped,
- the rate of penetration,
- the penetration resistance,
- and the inclination.

Deviations in the verticality of the foundation of monobuckets can be corrected either by assigning an eccentric vertical load on the top or by separate control of the suction pressure (by breaking up the caisson into a handful of sections). To fix the problem for spread-out structures, different suction pressure can be applied to the different suction caissons [Lesny, 2010].

Design codes and guidelines for shallow offshore foundations

3

In order to determine the capacity, the achievable factor of safety and the penetration curves of shallow foundations, in most cases designers choose to rely on deterministic methods. Such methods do not account for the statistical distribution and randomness of each parameter used in the formulas. Semi-probabilistic approaches try to treat some of the uncertainties present in the calculations with the so-called partial safety factors, each guideline offering different safety factors to be used. Deterministic overall safety factors can result in uneconomical or unreliable final designs, while semi-probabilistic partial safety calculations yield more precision. In the following chapters the nature and course of the existing calculation methods; deterministic, semi-probabilistic and probabilistic approaches, and the existing guidelines will be reviewed and studied through a common engineering problem with a focus on the achievable precision for bearing capacity equations and penetration curves of each method.

3.1 Introduction

The most common approach to determine the capacity and thus the load-penetration curve of a foundation is deterministic. In deterministic systems specific values are assigned to each parameter without taking into account the heterogeneity and complexity of the underlying soil which leads to untreated uncertainties. While the approach itself is convenient, deterministic approaches do not take into account the uncertainties related to the inherent, random variations (the natural spatial variability) of the soil parameters, geometric dimensions and loads and their effect on the response of the the structure (capacity) [Omar, 2014]. These uncertain parameters can include the damping or stiffness (important for dynamic analysis), friction angle, cohesion, undrained shear strength, soil unit weight, or the width of the foundation and the depth.

Semi-probabilistic approaches using total/partial safety factors and limit states can predict most of the uncertainties thus giving more precise results but are not advised to use in dynamic analysis as the assessment of the uncertainties related to the modal properties and excitation loads directly induced by the stochastic soil properties can be problematic and difficult [J.D.Sørensen, 2015]. Due to the natural variability and uncertainties related to the parameters, they should be represented as random variables, and treated with probabilistic methods to achieve better precision. Taken FE models as example, the spatial variability of the soil can be modeled by creating random field representation of the soil parameters [Omar, 2014].

3.2 Guidelines of practice

During the design of an offshore wind turbine the following three (plus one) limit states need to be analyzed [Det Norske Veritas]:

- Ultimate limit state: refers to the maximum, ultimate strength and stability of the foundation and subsoil, which must not be reached in any case. Loss of equilibrium (for example toppling), yielding or fracture of the material, buckling or corrosion can cause exhaustion of the capacity of structures. Calculations based on elastic or plastic theory can validate if the structure comply with the requirements.
- Serviceability limit state: refers to the deterioration of normal operation (without reaching the maximum capacity) by excessive deformation, vibration, leakage or corrosion. To comply with this limit state, the stiffness of the structure and foundation should be high enough to minimize the effect of vibration and to keep the displacements below a certain level [J.D.Sørensen, 2015]. For offshore wind turbines the long-term effects of smaller cyclic loads should be minimized to inhibit excess rotation of the foundation.
- Fatigue limit state: the welded details should be checked for fatigue failure, which is extremely important for offshore wind turbines, as the dynamic frequency of the structure is really close to the excitation frequencies caused by environmental harmonic loads [J.D.Sørensen, 2015].
- in addition to the previously mentioned the limit state of progressive collapse is also of importance, which is related to the post-accidental damage (collisions, explosions and earthquakes) collapse of the structure.

Obviously, the partial safety factors used for the different limit states are different as well. Generally there are 3 guidelines in use for stability calculations of offshore shallow foundations. Based on the codes of practice used (working stress design (WSD) or ISO standards) these 3 are the following according to [Gilbert, 2015; Gourvenec, 2011]:

- API RP 2GEO guideline (WSP,2011), in which the ultimate limit load is modified by an overall factor of safety. The American Petroleum Institute(API) recommends a value of 2 and 1.5 for bearing capacity and sliding failure respectively. The factor of safety accounts for measurement errors, statistical and model uncertainty and variations in live and dead loading and the variability of the soil environment.
- API RP 2GEO-LRFD (ISO), the Load and Resistance Factor Design(LRFD) approach, i.e. the partial safety factor approach, in which different factors are applied for soil strength parameters and loads. The guideline has been developed to adjust the original 2GEO to the ISO 19901-4 standard. API recommends to reduce the capacity by multiplying with the factor of 0.67.
- ISO 19901-4 guideline (2003), using the same, LRFD approach, as the API RP 2GEO-LRFD. The ISO recommends to use a material safety factor of 1.25 (drained) or 1.5 (undrained) to reduce the shear strength, and a load factor of 1.1 and 1.35 for dead loads and live loads respectively.

With the use of partial safety factors an attempt is made to separate the different forms of uncertainty. The material factor (used to reduce resistance) accounts for the uncertainties associated with the soil properties and calculation and testing models, while the load

factor considers the uncertainties related to the loads [Gilbert, 2015]. Even though the LRFD method can be considered as a semi-probabilistic method, implementing the better consideration of uncertainties, advanced probabilistic methods, like the Monte Carlo simulation, can yield more precise results. Despite the more precise results, according to [Det Norske Veritas]: "Probabilistic methods may be used in special cases only, after consultation with GL". As probabilistic methods are still not widely used in geotechnical design (except modern geohazard assessment), the partial safety method is preferred to the WSD, overall safety method, because of its ability to quantify uncertainties better [Gourvenec, 2011].

3.2.1 Bearing capacity equations for deterministic and semi-probabilistic calculations

The most widely used approach for stability analysis of shallow foundations are deterministic or semi-probabilistic. The bearing capacity of a foundation is of utmost importance in the ultimate limit state. Ultimate bearing capacity formulas are used to determine the maximum allowable load that can be transferred from the upper structure and foundation to the soil without shear failure in it. These formulas are based on the classical limit equilibrium methods established by Terzaghi (1943), Taylor (1948), Meyerhof (1951) and Vesic (1973) [Omar, 2014]. The model used can alter the results of the calculations as they vary in the shape of failure surfaces and normal stress distributions [Omar, 2014]. The design methods used for shallow offshore foundations are set out by the previously mentioned API, ISO and DNV (Det Norske Veritas) and are all based on the classical Terzaghi (1943) equations (vertically loaded strip foundation on top of a uniform Tresca soil), with several modifications accounting for load inclination and eccentricity, shape of the foundation and soil strength profile [Gourvenec, 2011].

The following bearing capacity formulas are based on [Gilbert, 2015; Det Norske Veritas; Gourvenec, 2011] for each of the different guidelines mentioned in Chapter 3.2:

API RP 2GEO guideline

The undrained bearing capacity formula for soils with linearly increasing shear strength over the depth is the following [Gilbert, 2015]:

$$Q_d = F \left(N_c s_{u,0} + k \frac{B'}{4} \right) K_c A' \quad (3.1)$$

where,

| | |
|----------|---|
| Q_d | Bearing capacity (ultimate vertical load) |
| s_{u0} | The undrained shear strength of the soil at the base of the foundation |
| N_c | Bearing capacity factor (for vertically loaded strip foundations on top of homogeneous soil deposit. For undrained cases $N_c = 5.14$) |

| | |
|-------|---|
| k | The gradient of the shear strength profile (in case of homogeneous deposits it is equal to zero) |
| K_c | Modification factor accounting for load inclination, penetration depth, foundation shape and surface/foundation base inclination |
| F | Modification factor accounting for the degree of shear strength heterogeneity and it is a function of the dimensionless degree of heterogeneity $\kappa = kB'/s_{u0}$. K can be obtained using fig. 3.1 |
| B' | Minimum effective foundation width |
| L' | Minimum effective foundation length |
| A' | Minimum effective foundation area, which is depending on the eccentricity of the load, the dimension of the foundation (B' , L' or radius) and if the foundation is circular or rectangular |

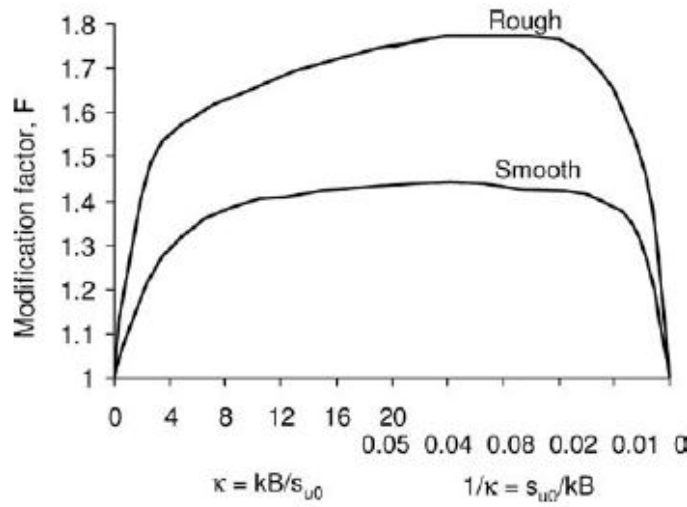


Figure 3.1. Diagram created by (Davis and Booker, 1973) to determine the F modification factor.

While the formula for shallow foundations in drained soils is [Gilbert, 2015]:

$$Q_d = \{p'_o(N_q - 1)K_q + 0.5\gamma'B'N_\gamma K_\gamma\}A' \quad (3.2)$$

where,

| | |
|-----------------|--|
| p'_o | The effective overburden pressure at the base of the foundation |
| γ' | The effective unit weight of the soil |
| N_γ, N_q | Bearing capacity factors accounting for self-weight and surcharge |
| K_γ, K_q | Modification factor accounting for load inclination, penetration depth, foundation shape and surface/foundation base inclination |

API RP 2GEO-LRFD guideline

This guideline can be perceived as a combination of the API RP 2GEO with the partial safety factors applied on the capacity ($\phi = 2/3$ factor times calculated capacity) [Gilbert, 2015].

ISO 19901-4 standard

The undrained ultimate bearing capacity is as follows [Gilbert, 2015]:

$$Q_d = \{F(N_c s_{u,0} + kB'/4)K_c/\gamma_m + p'_0\}A' \quad (3.3)$$

Compared to Eq. 3.1 there is only one new parameter to be introduced, which is the material factor (γ_m) taking the value of 1.25 for drained and 1.5 for undrained cases [Gilbert, 2015].

The drained ultimate bearing capacity equation is [Gilbert, 2015]:

$$Q_d = \{(p'_o + a)N_q K_q + 0.5\gamma' B' N_\gamma K_\gamma - a\}A' \quad (3.4)$$

where, a is the soil attraction and $a = c' \cot \phi'$

The difference between the API GEO2 and ISO standard is that the bearing capacity factors also contain the partial safety, material factors [Gourvenec, 2011]:

$$N_q = \exp(\pi \tan \phi'/\gamma_m) \tan^2(45^\circ + 0.5 \arctan(\tan \phi'/\gamma_m)) \quad (3.5)$$

$$N_\gamma = 1.5(N_q - 1)(\tan \phi'/\gamma_m) \quad (3.6)$$

[Gourvenec, 2011] observed the followings:

- the drained ultimate bearing capacity of soils subjected to compression is usually larger than of the undrained capacity, as the foundation loads contribute to an increase in the shear strength due to friction,
- however for dilatant sands the negative pore pressure induced by dilatation can lead to a drastic increase in the undrained shear strength of the soil. Because of suction effects, for tensile loads undrained conditions can be more beneficial.

3.2.2 Deterministic models

With the use of the bearing capacity theories and by making some modifications to the ultimate bearing capacity equations, according to [Houlsby, 2015] the vertical load acting on a spudcan foundation in clay at any penetration depth can be calculated as:

$$V = (N_c s_u + \gamma h)A \quad (3.7)$$

By substituting for the bearing capacity factor (N_c), undrained shear strength (s_u), soil unit weight (γ), penetration depth (h) and foundation area (A), the vertical loads can be easily defined for each depth after which the penetration curve can be drawn, which will serve as a prediction of the actual field behavior [Houlsby, 2015].

The undrained shear strength is usually determined by either laboratory shear tests, cone penetration tests (CPT) or by high amount of measurements using penetrometers, torvanes and/or minivanes, which means that the design strength profile is usually attained by fitting on a fairly high amount of scattered data [Houlsby, 2015]. In practice usually two fittings are made; a best fit and a lower bound fit, i.e. the most probable (expected

penetration values) and the worst case (maximum penetration values) fittings respectively. The worst case prediction will determine if it is safe to continue with the installation or not. In the end the field behavior can be compared with the model behaviour (predictions) [Houlsby, 2015].

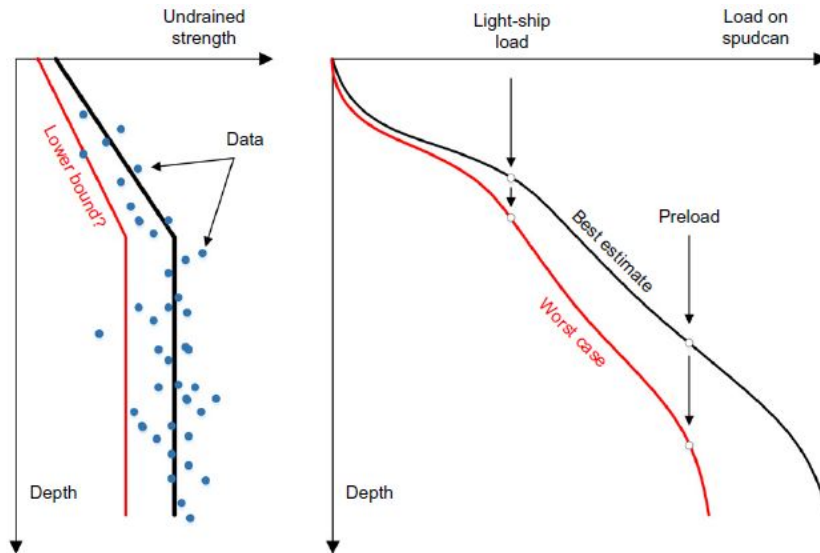


Figure 3.2. Lower bound and best estimate design strength profiles and penetration curves [Houlsby, 2015].

Problems of deterministic models

The biggest problem with deterministic methods like this is that they don't account for the spatial variability of the soil parameters (suggests an unreal soil environment). [Gourvenec, 2011] explains the problem thoroughly:

There are a variety of stress paths below a foundation, therefore the shear strength of the soil will differ in different locations. Depending on the location the shear strength and thus the behavior of the soil can be similar to either the triaxial compression, triaxial extension or simple shear (shear box) tests (difference can be as big as a factor of two). In addition to this the variation of the cyclic shear stresses' amplitude over the potential failure mechanism can again affect the available shear strength or lead to an increase in shear strain. The problem can be treated by using a soil constitutive model which accounts for the anisotropy of the shear strength and the effects of the cyclic loading. This behaviour can give different laboratory test results from the different soil samples, which leads to a wide scattering of the data. Hence CPT and other methods will also give wide scattering of the obtained soil parameters.

The other problem lies in how the designer engineer chooses the lower bound to the scattered strength data. Based on real-life designs and field tests [Houlsby, 2015] describes the problem: Being too cautious can result in completely wrong, large penetrations and can put a halt to the project for the wrong reason. To treat this issue standards suggest adopting strength characteristic values. To complicate the problem even more standards have different perception of this characteristic value. The commonly used Eurocode suggests to use the 5th percentile characteristic value, meaning only 5 out of

100 measurements happen to be below the characteristic value. However hoping the characteristic values to match the worst case fitting of the data is not expectable and not necessarily valid. By using probabilistic methods considering the statistical variations of the design parameters the problem can be treated.

3.2.3 Probabilistic methods

As mentioned before, now all the necessary variables can be statistically distributed, so that the uncertainties related to them can be represented as well. According to [Houlsby, 2015], such uncertainties can include:

- Boundary positions of the different soil layers can be subjected to uncertainties and errors in case the borehole measurements don't collect samples at the exact same position as the foundation is going to be placed. The depth of each layer thus can be statistically distributed to represent the uncertainties.
- The geometry of the foundations can be subjected to uncertainties as well.
- And most importantly the bearing capacity theory is subjected to errors as well. These uncertainties are mostly related to the idealization of the problem (for example when a spudcan is idealized as circular conical footing) or to the assumptions made.

Based on the assumed significance of the errors, uncertainties of each statistically distributed variable, different bias and coefficient of variation (COV) can be assigned to each parameter to statistically quantify the mentioned uncertainties [Gilbert, 2015]. These distribution parameters (bias, COV) are usually based on the comparisons of observed and predicted behaviour of foundations from previous design calculations (which depend on the foundation type, load conditions, etc.). Common values for statistical distribution parameters can be seen in Table 3.1. It can be seen in Table 3.1 that for example a horizontal load carries more uncertainty due to the randomness of the environmental loads, than a vertical deadload due to self-weight.

Usually either normal or lognormal distribution is chosen for the random variables. The latter is preferred as first, it is considered simple by using only two parameters, the second and most important aspect is that by using the lognormal distribution it can be guaranteed that the variable will be positive and third, based on many citations and field evidence, by using lognormal distributed variables a reasonable model can be constructed [Omar, 2014].

Based on the desired accuracy, methods with different complexity and cost can be chosen as a basis of the probabilistic calculations. These methods include the point estimation method (PEM), Taylor's series expansion method, like the so-called FOSM (first order second moment) and FORM (first order reliability method), the exact methods and the Monte Carlo simulation [Omar, 2014].

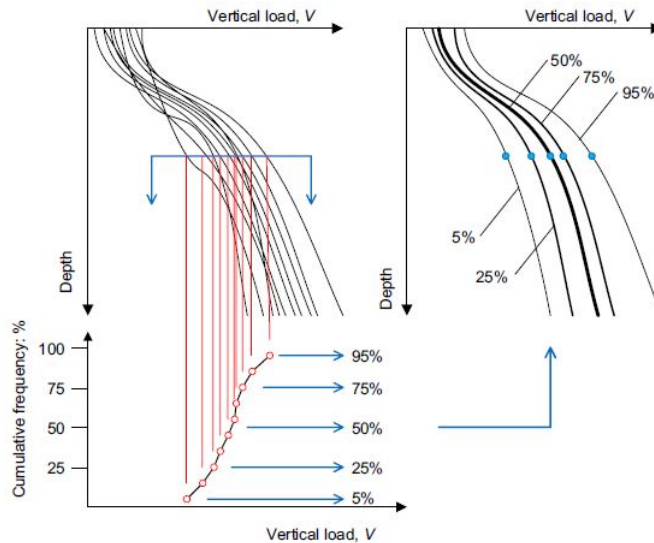
Table 3.1. Commonly used statistical distribution parameters for random variables for cases of shallow foundations [Gilbert, 2015]

| Random variable | Bias | COV |
|------------------------------------|------|-----------|
| Vertical load (V) | 1.0 | 0.05 |
| Undrained shear strength (s_u) | 1.1 | 0.15 |
| Horizontal load | 0.9 | 0.15 |
| $\tan \phi'$ | 1.2 | 0.05 |
| γ | 1.0 | 0.02-0.15 |

Site assessment using probabilistic methods

On the other hand in probabilistic calculations predefined, deterministic values are not used for the undrained shear strength at any depth. The method is based on the same calculation as mentioned before, but in this case the undrained design strength profile consists of the probabilistic distribution of potential strengths at each depth [Houlsby, 2015].

In this example the Monte Carlo simulation was used. The simulation technique chooses independent random values from the probability distributions of the variables within ranges limited by mean value and standard deviation [Omar, 2014]. It is not easy to determine the required (suitable) number of calculation cycles and thus the simulation usually involves hundreds of calculations with tens of thousand or more created variables.

**Figure 3.3.** Monte carlo simulation and their interpretation [Houlsby, 2015].

The load penetration curves in Fig. 3.3 were obtained by substituting the randomly generated variables produced by the Monte Carlo simulation in the deterministic Eq. 3.7. Then a method invented by Houlsby is used. These curves will serve as predictions of possible load-penetration curves. Then by slicing the curves at each depth, the loads need to be put in an ascending order by constructing a cumulative distribution curve (see: Fig. 3.3). Then the 5th, 25th, 50th, 75th and 95th percentile values are determined at each depth and put together to form a 5th, 25th, ... etc. percentile curve. Having used the

correct statistical parameters it can be concluded that 50% of the measurements should fall between the 25th and 75th percentile and 90% of the measurements should fall between the 5th and 95th percentile [Houlsby, 2015].

According to [Houlsby, 2015], using these percentile lines an engineer can assess if the actual measurements correspond to the understanding of the site, i.e. to the predictions. If the trend of the measurements follow the trend of the predictions and the measurements fall in between range of the predictions, then it can be concluded that the model captures the real response adequately. Assessing the model behaviour like this can only be considered reliable if the chosen statistical variation certainly seize the variability of the site accurately, meaning appropriate COV and distribution type for the site parameters should be chosen (the statistical parameters can be gathered based on the site investigation data) [Houlsby, 2015]. If the chosen deterministic model and statistical distribution is appropriate and correct, the data set obtained from the Monte Carlo simulation can be perceived as a set of experimental data [Omar, 2014].

3.3 Conclusion

Based on a reliability analysis of the guidelines for bearing capacity calculations conducted by [Gilbert, 2015] on a well manifold subjected to vertical load and placed on NC clay, it could be concluded that the achievable probability of failure (or reliability index) with the different guidelines using different safety factors are quite close to each others'. The probability of failures using a safety factor of 2 for the API 2GEO method, using a resistance factor of 0.67 for the API 2 GEO-LRFD and using a material factor of 1.5 for the ISO 19901-4 method are $4.1 \cdot 10^6$, $9.0 \cdot 10^6$ and $8.0 \cdot 10^6$ respectively. Three probabilistic methods were used in the aforementioned reliability analysis; FORM, FOSM and Monte Carlo simulation, all of which yielded similar results.

In case of a vertically and horizontally loaded valve placed on sand, the calculations yielded slightly different probability of failures for the guidelines. The different probability methods gave different results as well. While the FORM and Monte Carlo results were similar, in the case of sand the FOSM method overestimated the probability of safety by a factor of 4-6 due to the non-linear limit state function [Gilbert, 2015].

According to results from another research conducted by [Omar, 2014], the guidelines using the safety factor methods may not be appropriate in case of highly varying soil parameters. In the probabilistic calculations of all parameters the internal friction angle was the main contributor to the variation of the soil and thus the FOS (factor of safety), while the cohesion, loads and soil unit weight had a neglectable effect [Omar, 2014].

Based on the results it can be seen that the reliability of the design guidelines is case-sensitive, depending on the soil environment and loading conditions as well and that with the introduction of probabilistic methods by representing the uncertainties with statistical distributions of the parameters, a more reliable, economical and safe design solution can be achieved.

Suction caisson behavior under different loading conditions 4

In this chapter the behavior of suction caissons subjected to different loading conditions in sand will be reviewed to give an overview of the expected caisson behavior before constructing the numerical model. As requirements against the foundation are different in each limit states, in addition to the capacity and bearing behavior under a one-time, ultimate loading event, serviceability limit states (sufficient stiffness) related to the long-term behavior will be examined as well, with a focus on the caisson behavior under tensile loading and the achievable pull-out resistance. The chapter concerns caisson behavior in drained conditions, i.e. in sands.

There are still many unclear issues related to the design of offshore suction caissons. Several studies, including both model tests and field tests (only a few) have been carried out, most of which planned to lay down the foundations for design guidance addressing issues like performance under cycling loading (capacity after n number of cycles-including the degradation of stiffness), pullout resistance, and an assessment of the soil types in which they can be possibly installed [Houlsby, 2015]. Researches have been conducted on both monopod and multipod foundations. Monopod foundations are the main choice for shallow water conditions and the response under moment(/horizontal) and vertical loading has been the purpose of such tests.

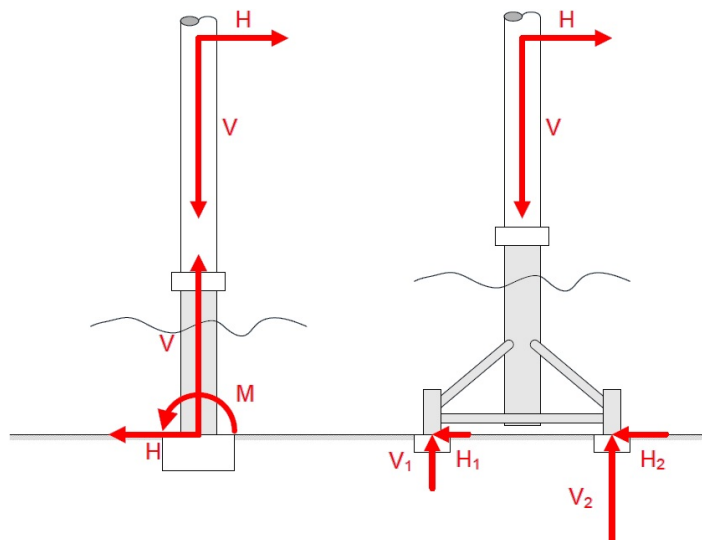


Figure 4.1. The loads to which a monopod or tetrapod/tripod caisson foundation are subjected [Houlsby, 2015].

The following figures were created based on tests conducted by Houlsby and Byrne. A summary of their work and the key results of many of their articles to asses offshore

foundation options can be read in [Houlsby, 2010] and [Houlsby, 2015]. According to [Houlsby, 2010] the following factors are very important to be analyzed for monopod foundations:

Capacity:

First of all the foundation must resist the ultimate, one-off large event without suffering any significant deformation [Houlsby, 2010]. The typical loads on a monocoisson and tripod/tetrapod foundation can be seen in Fig.4.1. The horizontal wind loads range from 1 to 2 MN, the vertical load is approximately 6 MN, while the environmental loads caused by the waves, tides and ice range from 3 to 8 MN usually, all of which depend on the actual size of the wind turbine and the water depth [Houlsby, 2015]. As for offshore wind turbines the loads are very uni-directional, it is important to design the foundation with sufficient margin that the cyclic loading won't cause degradation of response over a large number of cycles and thus won't result in the tilting of the foundation/structure (which can dramatically impair dynamic behavior) [Houlsby, 2010]. Using lab or field test data, relationships between the allowable moment, horizontal (environmental loads) and applied vertical load (dead weight) of the foundation can be developed. Figure 4.2 shows the relationship between the non-dimensional moment capacity and the applied vertical load, in other words a part of the yield surface based on results of tests conducted by Houlsby and Byrne.

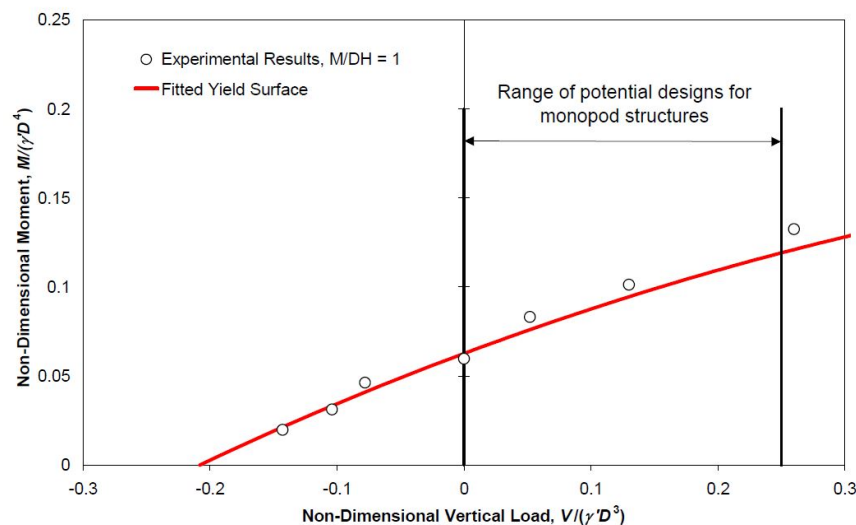


Figure 4.2. Experimental yield surface showing the relationship between the moment capacity and the applied vertical load based on the test data [Houlsby, 2010].

As mentioned before there is an interaction between the H , V forces and M moment, hence the need to create reliable 3D failure and yield envelopes. Meaning that Fig. 4.2 is only applicable for a particular ratio of moment to horizontal loading. So with further assessment of the test data Houlsby and Byrne focused on developing yield surfaces for a larger range of moment/horizontal load ratios. The ellipses can be seen in Fig. 4.3, in which the relationship between horizontal and moment load can be seen for tensional, 0 and compressive vertical loads. It is important to notice in both figures, that depending on the level of horizontal loading, considerable moment capacity can be achieved even in

tension [Houlsby, 2010].

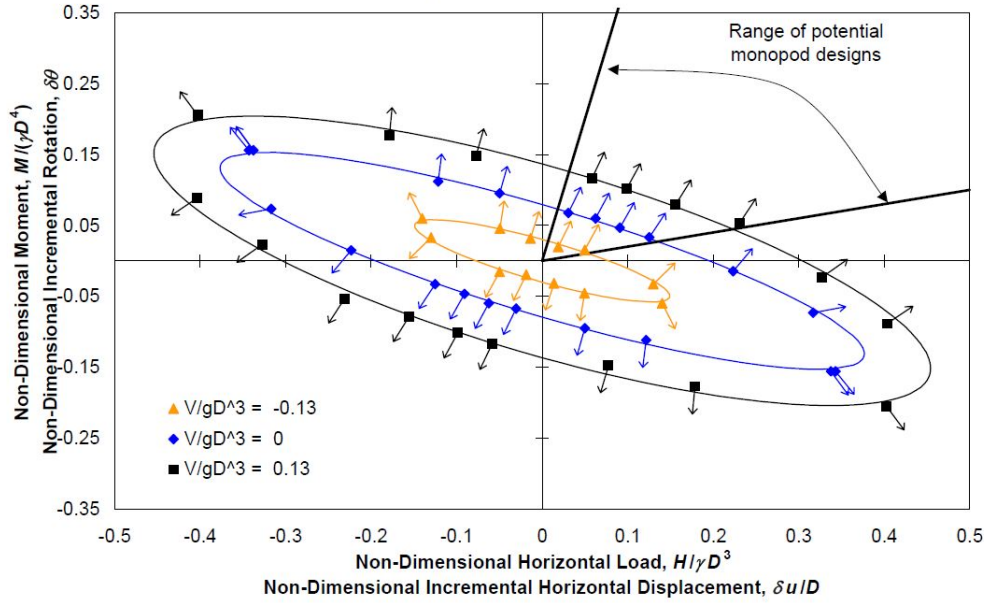


Figure 4.3. Experimental yield surfaces showing the relationship between the moment/horizontal loads and the applied vertical load based on the test data [Houlsby, 2010].

Stiffness:

In addition to the ultimate capacity, a more important design issue is related to the foundation stiffness. The stiffness of the structure dramatically contributes to the dynamic behaviour of the structure. The frequency of the foundation depends on the stiffness and by the degradation or improvement of the stiffness the decreased or increased frequency can interfere with the excitation frequencies, even though the structure was dynamically designed to avoid those frequencies. The frequencies to be avoided are the rotational and blade-passing frequencies (0.3 and 1.0 Hz, respectively) [Houlsby, 2015]. It is essential to model these changes in stiffness and several attempts have been made already, unfortunately all of them lacking the ability to model degradation or enhancement of response over thousand or hundreds of thousands of cycles [Gourvenec, 2011], especially for suction caissons (there are some reliable formulas available for monopiles). These advanced models are based on a new theory called continuous hyperplasticity and use the basic "force resultant" models, hence allowing engineers to take the cyclic response into account [Houlsby, 2010].

Several tests have been conducted to study the behavior of suction caissons subjected to cyclic moment and vertical loads. These tests and their interpretation will be reviewed later in Chapter 4.2.

Scaling of models, response:

As field tests are very expensive compared to model tests, it is easier and more economical to conduct such tests in the laboratories. Laboratory tests at model scales allow the detailed understanding of the behavior of the foundation under different loading conditions, therefore it is of utmost importance to be able to properly scale the laboratory results so that a comparison can be made between different tests with different geometries [Houlsby, 2010].

So to compare laboratory and field tests, dimensionless, normalized parameters are used, so that the stiffness and strengths are similar in equivalent tests. Based on the lab and field tests, [Byrne, 2006] have concluded the results and came up with several scaling relationships for OWT caissons. In case the densities are the same in the field and lab so that the same bearing capacity factors can be used for both cases [Byrne, 2006]:

- in clays for vertical and horizontal loads and for moments a scale factor of $s_u \cdot R^2$ and $s_u \cdot R^3$ should be applied respectively,
- while in drained sands, $\gamma' \cdot R^3$ and $\gamma' \cdot R^4$ should be used for loads and moments scales, respectively,
- and for displacements in drained soil the following scale factor should be used: $(w/D) \cdot (p_a/\gamma' D)^{1/2}$, in which the second part elucidates for the stress dependent change of the shear modulus.

The applicability of the normalizing techniques described above were proved by [Houlsby, 2015]. The results of the cyclic tests conducted on models of different sizes with different installation methods can be seen in Fig. 4.4. The remarkable similarity of the hysteresis loops from each model test can be seen in the figure as well. Fig. 4.4 proves that if proper normalization techniques are used on the results of laboratory model tests (like the ones proposed by [Byrne, 2006]), field results can be precisely predicted [Houlsby, 2015].

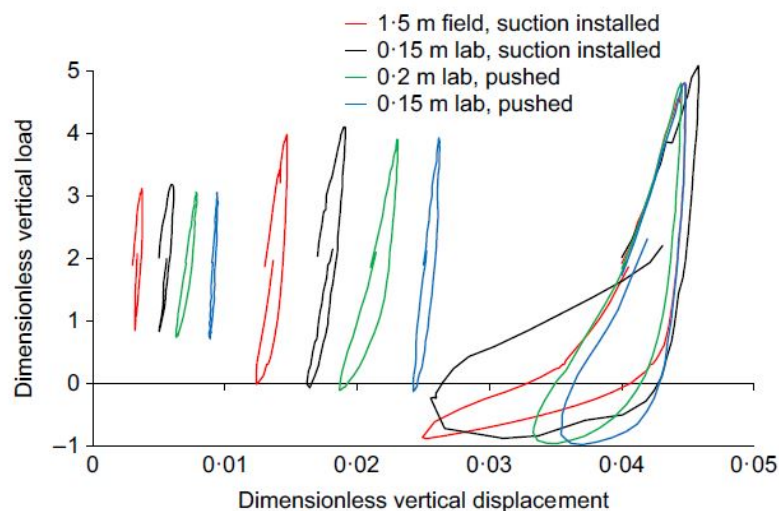


Figure 4.4. Applicability of normalization techniques to compare different models [Houlsby, 2015].

Interpretation of results for models with different scaling will be reviewed in the following sections.

4.1 Monotonic loading

In this section the bucket behavior under moment/horizontal and vertical loads (both compressive and tensional) will be reviewed. As the pull-out resistance and caisson behavior during tension is important for the design of multicaisson foundations, special focus will be given to vertically pulled caisson behavior in drained sand.

4.1.1 Compression

The following results and their interpretation were obtained by a finite element analysis conducted by [Collin and Charlier, 2016].

First [Collin and Charlier, 2016] considered the case when the caisson was subjected to compression loading. The applied vertical load is balanced by the reactions that can be seen in Fig. 4.5. A drained and a partially drained case have been reviewed.

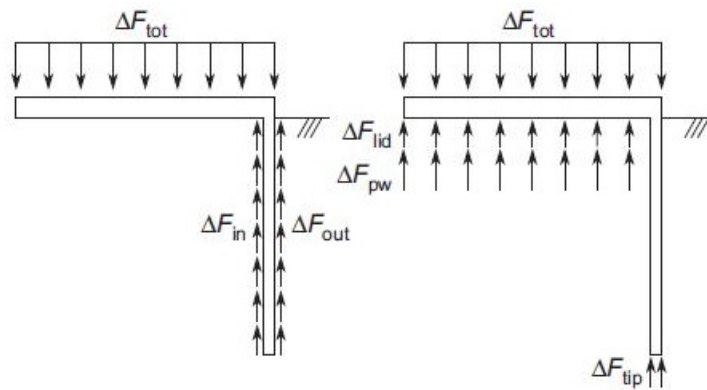


Figure 4.5. The reaction components during compression [Collin and Charlier, 2016].

Drained case

In the calculations the loading rate is considered very slow according to the rate of the pore water pressure (u) dissipation, meaning that in the drained case the u doesn't differ from the initial value (constant u).

In Fig. 4.5 ΔF_{tot} is the variation of the applied total load on top of the bucket lid, ΔF_{pw} is the integral of variation of u at the bottom of the lid, ΔF_{lid} is the integral of effective contact stresses at the bottom of the lid, while ΔF_{in} and ΔF_{out} are the integral of variation of the shear stresses along inside and outside of the caisson skirt, respectively. In the study ΔF_{tot} was increased until the global failure of the system including the soil or until the failure of a single point in the material [Collin and Charlier, 2016].

Results from the drained compression simulation can be seen in Fig. 4.6 and Fig. 4.7, in which the relative displacement (Δy) is calculated from the top center point of the bucket lid.

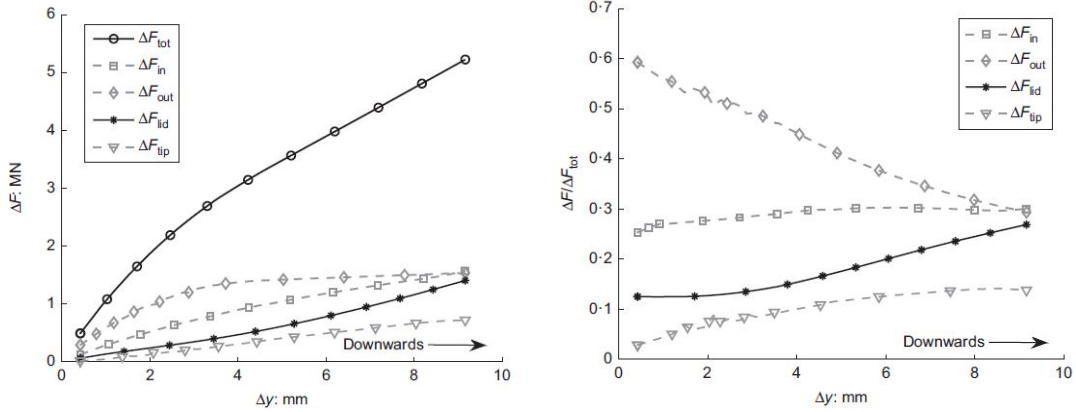


Figure 4.6. Variations of the components of reaction for drained compression simulation [Collin and Charlier, 2016].

Figure 4.7. Variations of the components of reaction normalized by the total load for drained compression simulation [Collin and Charlier, 2016].

Initially 60% of the total load is sustained by the component ΔF_{out} . Because of the relative displacement between the soil and caisson, ΔF_{out} is continuously decreasing as the friction starts to get mobilized along the outer skirt (see: Fig. 4.7) and reaches a constant value after about 2/3 of the total displacement (Fig.4.6). With the increase of the total load, and thus the increase of the load transferred to the soil by the lid (ΔF_{lid}) the relative movement between the inside of the caisson and soil is decreased resulting in increased confinement and thus increased shear stresses along the inside of the skirt, ΔF_{in} . The tip and lid are showing dependent behavior. The share of the lid shows a significant increase after the friction starts to get mobilized along the skirt resulting in the plastification of the soil under the tip and the decrease of the tip stiffness (almost a flat line in Fig. 4.7) [Collin and Charlier, 2016].

Partially drained case

In this case the total load is increased to 4.3 MPa at a higher rate, after which it is held constant. This is identical to the case of a consolidation process. As a result of this the generated pwp doesn't remain constant but given that it is a partially drained configuration and not undrained, the pwps are allowed to dissipate.

The increased stiffness compared to the drained configuration can be seen immediately by taking a look at Fig. 4.8. In this case the pore water dissipation is quite limited as the water is trapped inside the bucket, and pwp (ΔF_{pw}) is generated (until the beginning of the dissipation process, after which it decreases constantly by being "consumed" by the shear, lid and tip shares of the total load) in the soil surrounding the caisson, resulting in the decrease of effective stresses. This behaviour is similar to the one that is happening during the real installation, when suction is applied to sink the caisson. However due to the aforementioned effect, initially the share of ΔF_{out} is lower than in the drained case. After the share of ΔF_{out} is fully mobilized, it shows a steep increase (reaching the drained resistance) as soon as the total load is not increased anymore and the pwp dissipation is allowed to happen [Collin and Charlier, 2016].

Even though the case is partially drained, an almost undrained behavior can be noticed, as the soil acts like a plug and the share of ΔF_{lid} , ΔF_{in} and ΔF_{tip} is almost zero of the total load during the pushing phase.

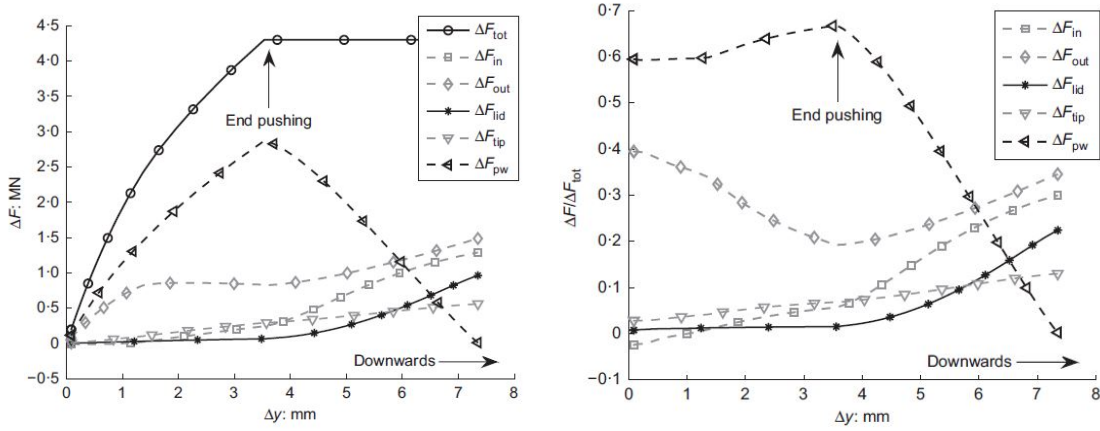


Figure 4.8. Variations of the components of reaction for partially drained compression simulation [Collin and Charlier, 2016].

Figure 4.9. Variations of the components of reaction normalized by the total load for partially drained compression simulation [Collin and Charlier, 2016].

4.1.2 Tension

One of the most important questions in tripod/tetrapod design is the pull-out capacity and the behavior of such foundations subjected to tensile loads (especially cyclic behavior under tensile loads, which will be discussed in the following section). First lets take a look at the caisson behavior in the same finite element analysis as before conducted by [Collin and Charlier, 2016].

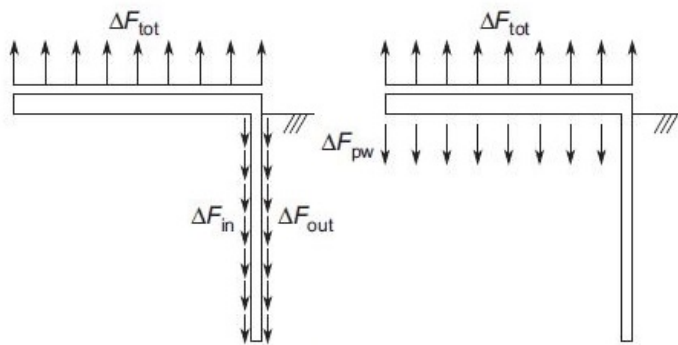


Figure 4.10. The reaction components during tension [Collin and Charlier, 2016].

Drained case

It can be seen in Fig. 4.11 that only two components of the reaction is active against the tension, ΔF_{in} and ΔF_{out} , meaning that the tension is sustained only by friction along the

caisson skirt. As contact is lost as a result of the tension between the soil and lid/tip of the bucket, ΔF_{lid} and ΔF_{tip} equal to zero [Collin and Charlier, 2016].

The stiffness of the inner friction component is lower because the soil inside the bucket moves with the skirt wall to some extent, i.e. the relative movement between the soil and skirt inside the bucket is smaller, than outside of it, which results in lower share of the reaction against the applied load. After a deformation of about 1.8 mm is reached, the outer component of friction is completely mobilized and the total load is only sustained by the inner friction component until failure occurs [Collin and Charlier, 2016].

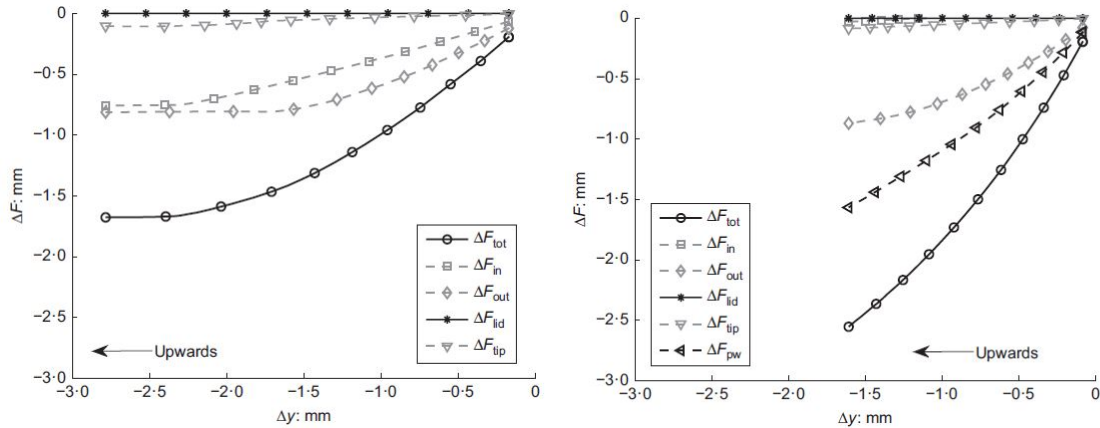


Figure 4.11. Variations of the components of reaction for drained tension simulation [Collin and Charlier, 2016]. **Figure 4.12.** Variations of the components of reaction for partially drained tension simulation [Collin and Charlier, 2016].

Partially drained case

Unlike in the compression simulation, this time the tension load has been increased until failure with a constant speed of 0.4 MN/s. The results of the simulation can be seen in fig. 4.12. By comparing the results of the drained and partially drained cases, the difference in the achievable capacity due to the fluid flow around the suction caisson is well-marked. This induced fluid flow results in the negative variations of the pwp resulting in an increase of the effective stresses along the caisson skirt, directly leading to higher available friction (higher values of ΔF_{out} compared to the ones in drained simulation). Other experimental and numerical tests prove the increase in the overall capacity due to the presence of pore water, ΔF_{pw} components, sustaining at least 50% of the total applied traction load [Collin and Charlier, 2016].

Caisson behavior under traction loading (both monotonic and cyclic) will be further analyzed in the upcoming sections.

Laboratory pull-out test

Results of model tests conducted by [Houlsby, 2015] give a better overview of the factors affecting the pull-out resistance of caissons.

As it can be seen from the previous results it can be concluded that pull-out resistance in ULS of a suction caisson subjected to tensile load is relatively high, but depends on many factors. Three different model tests have been conducted in sand under drained conditions by [Houlsby, 2015], with different loading rates and pressure conditions. The results of the test can be seen in fig. 4.13.

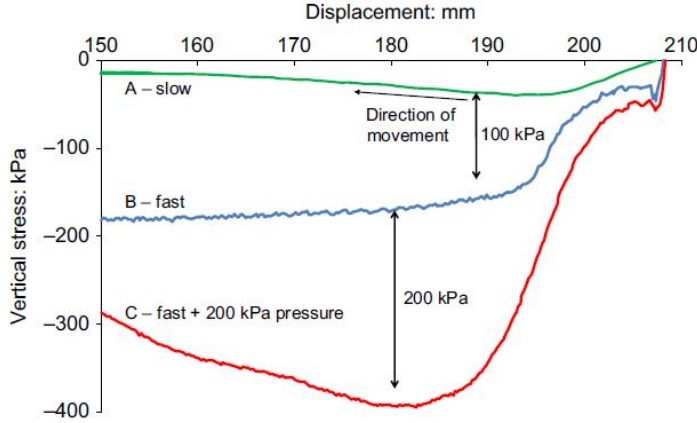


Figure 4.13. Results of tensile loading of a model caisson under different conditions [Houlsby, 2015].

In case A the load was applied very slow and the overall vertical stress acting on the caisson was small. As discussed above, these stresses equal to the inner and outer component of the induced friction, as the negative pore pressures are allowed to dissipate due to the slow rate of loading. In case B the caisson was pulled very fast, allowing suction effects to develop due to the presence of negative pore pressures, leading to an increase in the effective stresses and thus the pull-out capacity of the caisson. According to [Houlsby, 2015] the capacity is limited by an important phenomena, the cavitation of the fluid in the pores under the caisson. This event strongly depends on the pressure to which the test specimen is subjected. In case B the cavitation occurs around -100 kPa gauge pressure and the increase in capacity compared to case A is also approx. 100 kPa. In case C the rate of loading was very fast as well, but Houlsby performed the test in a pressure chamber subjected to an elevated pressure of 200 kPa. By doing so, the "real-life", water pressure conditions at the bottom of the sea could be simulated. The 200 kPa increase in capacity compared to case B proves that the pull-out capacity depends on the onset of cavitation (which is determined by the available water pressure) and the amount of pressure the test specimen or the caisson is subjected to [Houlsby, 2015].

Even though the ultimate tensile resistance of caissons in field conditions thought to be high, the deformations related to such high levels of loading are restricted by serviceability limit states [Houlsby, 2010, 2015]. According to [Houlsby, 2015], just by considering the initial part of the curves in fig. 4.13, and scaling the deformations up to field dimensions, they wouldn't comply with the SLS requirements and would definitely cause operational problems. First of all, Houlsby suggest as a solution, that the caissons shouldn't be subjected to significant tension loads in order to limit excessive deformations. Secondly, on serviceability grounds only the frictional component of the pull-out resistance should be taken into account and the cavitation limited end bearing component of the capacity

shouldn't be considered [Houlsby, 2015].

4.2 Cycling loading

As the environmental loads the offshore structures subjected to are cyclic in nature, the analysis of caissons under such loads are crucial. In this section the results from tests conducted on three model caissons with the diameter of 0.15, 0.2 and 0.3 m and two field caissons with a diameter of 1.5 and 3 m, subjected to the previously introduced cyclic loading in drained conditions will be reviewed. The results have been normalized, hence the non-dimensional values can be compared and the caissons have been loaded in a similar way in all tests. The analysis in addition to the cyclic behavior will focus on the scale of response, the comparability of the lab and field models and the differences in results obtained by pushed or sucked installation.

4.2.1 Vertical loading tests

Vertical cyclic analysis of suction caissons are important as normally the caissons of offshore wind turbines are in compression, but during the operational lifetime it is constantly subjected to cyclic vertical loads of small amplitudes and to relatively big amplitudes during extreme events [Houlsby, 2015]. The results of a vertical cyclic loading of a caisson in saturated sand conducted by [Houlsby, 2015] can be seen in fig. 4.14. (Note: the figure is not part of the aforementioned model and field tests, it was used as an example to better represent the results.) The caisson was loaded by groups of continuously increasing load cycles.

There are a number of factors need to be discussed and observed during cyclic loading [Byrne, 2006]:

- the change of stiffness,
- the accumulation of deformation,
- the size of hysteresis with the progress of loading.

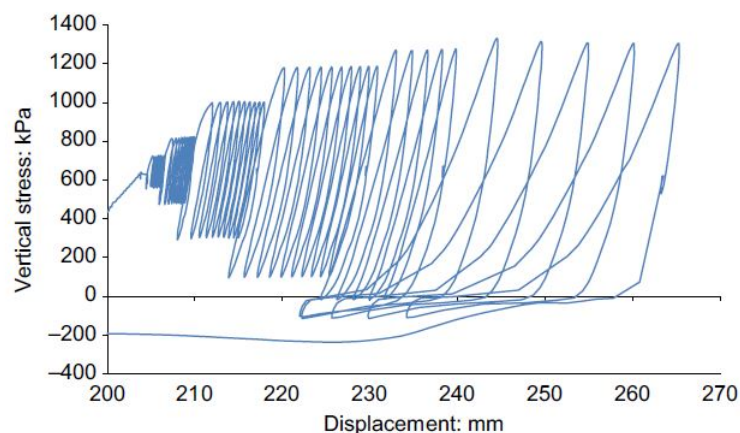


Figure 4.14. Results of vertical cyclic loading applied on a model caisson installed in sand [Houlsby, 2015].

It can be seen in the figure that initially a pretty stiff response with little hysteresis is obtained for the small amplitude cyclic loads. By increasing the amplitudes (the vertical load), a more flexible response (decreased stiffness) can be observed with increasing sizes of hysteresis. The size of the hysteresis refers to the amount of frictional damping [Houlsby, 2015]. With the increase of cyclic amplitude, these hysteresis become more and more open, resulting in an increase of damping. The accumulation of downward deformation with the progress of loading is observable as well. With the onset of tensile loading, the response greatly changes in all three tests [Houlsby, 2015; Byrne, 2006, 2010]: the foundation moves upwards significantly and as compression is reapplied, it moves back an equal distance, giving the load cycles a unique, "banana shape". It is the tensile load that triggers the residual downward movement with each cycle, which can lead to the weakening of the soil structure and thus the overall capacity. This leads to a quite paradoxical phenomenon for multipad foundations; the tripod/tetrapods will tend to lean towards the main wind direction. [Houlsby, 2015]. [Houlsby, 2015] emphasizes that the aforementioned residual downward movement is only valid unless the mean(!) vertical loading is compressive.

The observations made in the previous paragraph can be examined on models of different size and installation method. The following model and field tests and the interpretation of results are based on [Byrne, 2006, 2010].

It can be seen in fig. 4.15 that almost $9\times$ larger accumulated deformations occurred for the suction installed lab caissons than for the pushed specimens. The phenomenon has been described before, when suction is applied in the soil a local disturbance is created and the effective stresses decrease due to the loosening of soil fabric. By comparing fig. 4.15 with fig. 4.16 it can be seen that the suction installation didn't have a significant effect on the field caisson. Based on this it was concluded by [Byrne, 2006] that the effects of suction do not increase with the caisson diameter. Laboratory tests on lab caissons with different diameter also showed that the amount of accumulated deformation reduces with scaling (bigger models give less accumulated deformation) [Byrne, 2006].

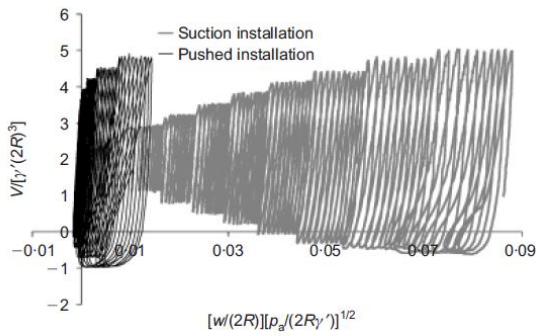


Figure 4.15. Lab test data of vertical cyclic loading of a 0.15 m diameter caisson [Byrne, 2006].

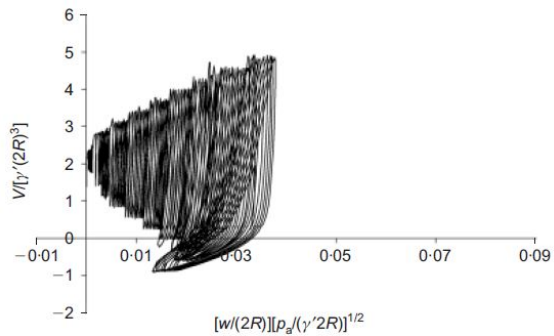


Figure 4.16. Field test data of vertical cyclic loading of a 1.5 m diameter caisson [Byrne, 2006].

The decrease of the secant stiffness with the increase of the amplitudes of loads can be observed in fig. 4.15 and fig. 4.16. The variation of the normalized secant unloading stiffness with the increasing cycles can be seen in fig. 4.17. It should be noted that

variation of the stiffness doesn't occur within cycles of the same load amplitude, but after each load increment. [Byrne, 2010]

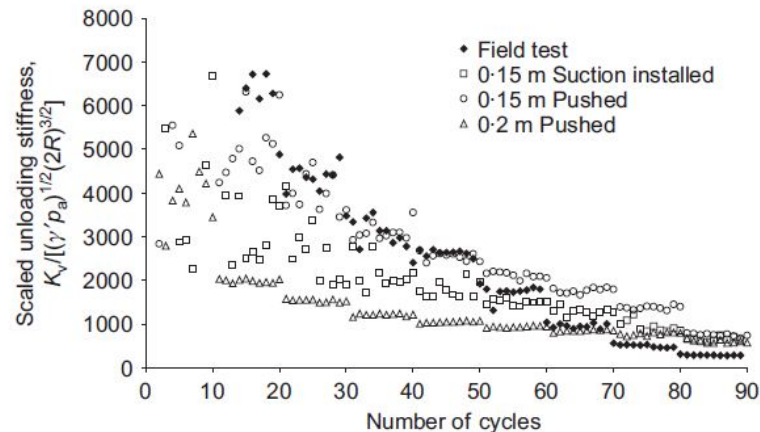


Figure 4.17. The normalized secant unloading stiffness against the number of cycles [Byrne, 2006].

4.2.2 Moment loading tests

Field and laboratory test results from the moment loading tests (moment-rotation curves) can be seen in fig. 4.18 and fig. 4.19. The data show increasing cycles of strain amplitude. The interpretation of results are similar to the one obtained from the vertical loading tests. But the response is slightly different for low/moderate and high/very high strains for the field case. For the former: initially the response is stiff with a small hysteresis. With the increase of strain amplitudes the results show a more flexible (less stiff) response with increasing hysteresis [Houlsby, 2010; Byrne, 2006]. The same thing happens during unloading; an initially high stiffness at smaller strains is followed by a reduced stiffness with the increase of strains [Houlsby, 2010].

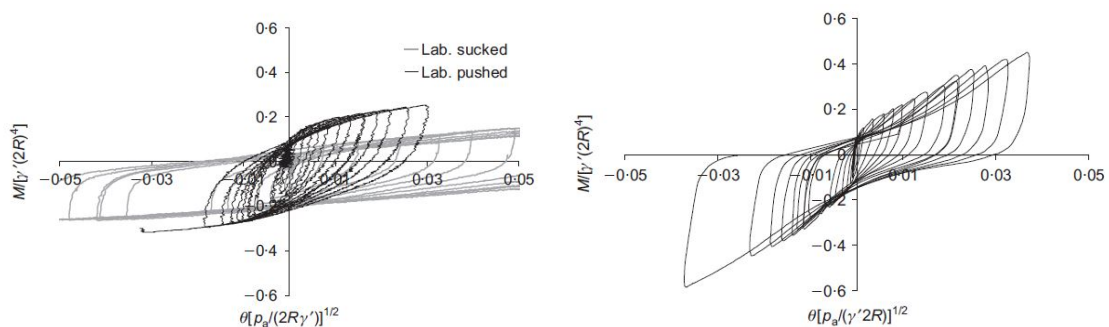


Figure 4.18. Laboratory test data of moment loading of a 0.2 m diameter caisson [Byrne, 2006].

Figure 4.19. Field test data of moment loading of a 3 m diameter caisson [Byrne, 2006].

At very high strains a unique behavior occurs, which is often called "gapping" [Byrne, 2006, 2010]. This can be seen in fig. 4.19. Initially there is a stiff response, followed by a weakening of stiffness, after which a slight stiffening of response is observed once

again. The gapping effect at the larger amplitudes, can not be observed in the laboratory tests results, probably because the measured rotations weren't large enough to capture the effect. At larger amplitudes the lab and field tests may give different results, but at smaller amplitudes, which are relevant for offshore wind turbine design, the two tests give very similar results (very similar achieved moment loads for the same rotation). As it was already observed in the case of vertical loading the installation method has a huge influence of the lab test results. The same happens for moment loading, the moment loads for the sucked lab specimen are substantially lower (approx. 50%) than for the pushed specimen [Byrne, 2006].

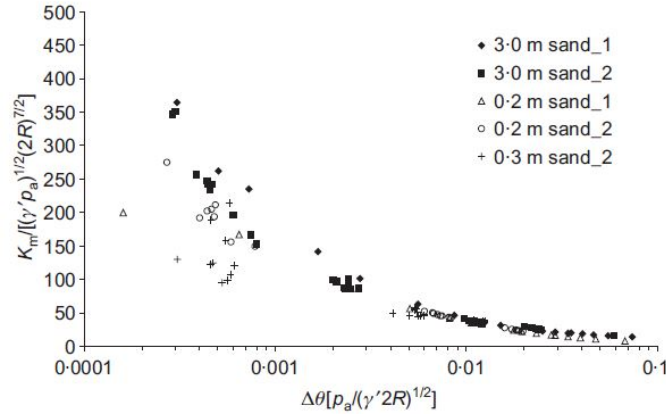


Figure 4.20. The normalized secant unloading stiffness against the number of cycles [Byrne, 2006].

Fig. 4.20 shows the change of the normalized unloading secant stiffness for all tests. The similarity of the results obtained from the different tests can be clearly seen, once again showing the applicability of the formulas presented by [Byrne, 2006]. When using eq. 4.1 to predict the stress dependency of the stiffness, the accurate choice of the n parameter is significant in order to obtain acceptable comparison between the data of different model tests. In the tests conducted by [Byrne, 2006], a factor of 0.5 was used for n .

$$\frac{G}{p_a} = A \left(\frac{\sigma'_v}{p_a} \right)^n \quad (4.1)$$

where,

| | |
|-------------|--|
| p_a | The atmospheric pressure (reference pressure, kPa) |
| σ'_v | The effective vertical stress level |
| A | A dimensionless constant |
| G | The shear modulus |

4.3 Summary of results

The unique behavior of caissons under monotonic and cyclic, both moment and vertical loads in sands (drained and partially drained cases) have been reviewed based on studies,

lab tests and their interpretation conducted by [Byrne, 2006, 2010; Collin and Charlier, 2016; Houlsby, 2015]. In this section the results obtained by the mentioned authors are summarized and grouped.

It has been observed in the monotonic compressive test that the response in drained and partially drained conditions are different. In the latter case the presence of u doesn't allow the other reaction components to take bigger share of the total load, which completely changes once the dissipation of pwp begins and the load is set to a constant value.

The caisson behavior under traction load was of main importance in this chapter. The main difference in the drained and partially drained case is that in the former the tension load is sustained by the progressive mobilization of both components of the friction along the skirt, while for the latter only the outer friction is mobilized, as the inside of the caisson acts similar to undrained conditions, i.e. as a plug. It is very important to make a distinction between low and high rate of loading. It was observed that when the specimen was subjected to a higher rate of tensile loading (partially undrained case), underpressures (suction) were generated, which affected the tensile capacity dramatically. Laboratory pull-out tests proved that the pull-out resistance depends on the cavitation phenomenon in addition to the rate of loading, the onset of which is determined by the pressure that the caisson is subjected to (i.e. height of water). The significant change of behavior (accumulation of downward deformations) once tensile vertical load is applied to the caisson has been observed, which lead to the conclusion that tension should be limited and the cavitation phenomenon shouldn't be taken into account, i.e. the capacity should only be determined by the frictional component in order to comply with the SLS requirements and to avoid interference with operation (even though the tests show significant tensile capacity).

The key observations in cyclic tests included: the decrease of stiffness, accumulation of deformation and the increase in the size of the hysteresis with the progress of both vertical and moment loading. Normalization techniques proved to be accurate for cyclic tensile tests and for low rotation amplitudes for cyclic moment tests (more divergence at higher amplitudes). The method of installation greatly affected the laboratory results, and it has been concluded that the accumulation of determination decreases with scaling.

Other tests and results of the tests conducted by the authors of the analyzed articles [Houlsby, 2010; Byrne, 2006, 2010; Collin and Charlier, 2016; Houlsby, 2015] have shown that the response of caissons subjected to both monotonic and cyclic loading can depend on the following factors:

- the speed of loading (development of suction - depending if it's low or high),
- the rate of vertical loading the caisson is subjected to,
- length of the caisson (embedded ratio, L/D),
- friction coefficient of the walls,
- applied pressure - onset of cavitation,
- method of installation (for lab tests, it doesn't have a significant effect on field caissons),
- soil properties, including the relative density of sands,
- permeability of the soil (drained/partially drained or undrained case),
- and if numerical modelling is considered, the choice of the constitutive soil model.

For cyclic loading it is important to take into account the direction of loading (one or two way loading?). This hasn't been mentioned in detail, as tests have only been made for piles and the submitted formulas are only applicable for piles [Houlsby, 2015]. Other problem in the design is related to the fact that the change of stiffness and accumulated deformations in the cyclic tests depend on the amount of cycles. This leads to a problem as test data is usually available for a few hundred (or less) cycles, from which is really hard to predict for the long term behavior of foundations, which can be, in reality, subjected to millions of cycles.

The effect of some of the mentioned factors on the capacity and response of suction caissons will be assessed in the following chapter in the numerical analysis.

Part II

Numerical analysis

Model validation and soil constitutive models 5

In this chapter the validation of a reference suction caisson is to be conducted. First a general overview of the most relevant material models and the parameters used in them is given. Consequently a validation of the model is done by constructing a model previously analyzed by [Thieken, 2013] and obtaining similar results. Then a convergence study is conducted, meaning comparing results and achieved failure modes obtained from different model sizes and element numbers.

As guidelines are still not entirely available or too complex to use in general design and also the ones which consider general combined loading are unable to cope with several issues (soil permeability, rate of loading) especially when it comes to dynamic analysis of suction caissons (stiffness degradation, damping), finite element calculations and numerical modelling are an indispensable tool in the analysis of the response of such foundations. These methods yield more reliable results than analytical calculations and can imitate the real foundation behavior better. For this first a model is calibrated based on [Thieken, 2013] to get the same (very similar) results obtained in the article, after which a convergence analysis must be conducted to make sure that the constructed model can be reliable for further studies.

The aim of the numerical analysis in this project is to conduct a parametric study after the model calibration. For this the Mohr-Coulumb model is used as a first estimation of real sand behavior, after which results are going to be obtained using more advanced soil constitutive models, such as the hardening soil model, allowing a comparison between the foundation responses. Therefore a detailed explanation for the used constitutive models is given in the following sections.

5.1 Soil constitutive models

As the numerical analysis will deal with foundations in sand environment, only the constitutive models used by Plaxis and relevant for sands will be discussed further on and be used in Plaxis for the comparison of results.

The first thing is to determine the input parameters based on the chosen soil constitutive model. Based on the desired accuracy and material type (rocks, metals, undrained or drained soils) the user can choose from several material models to use for the calculations.

The number of parameters needed for each model is different hence the complexity of the models differ as well.

The most commonly used constitutive models, starting from the least complex one, are [Kumarswamy, 2016]:

- linear elastic model both for stiff and soft soils (see: fig. 5.1 a.),

- Mohr-Coulomb model both for stiff and soft soils (see: fig. 5.1 c),
- hardening soil model both for stiff and soft soils /Plaxis soil model/(see: fig. 5.1 d),
- hardening soil model with small strains both for stiff and soft soils /Plaxis soil model/,
- cam-clay and modified cam-clay models for clays,
- soft-soil model for clays,
- jointed rock model for rocks and
- the Hoek-Brown model for rocks.

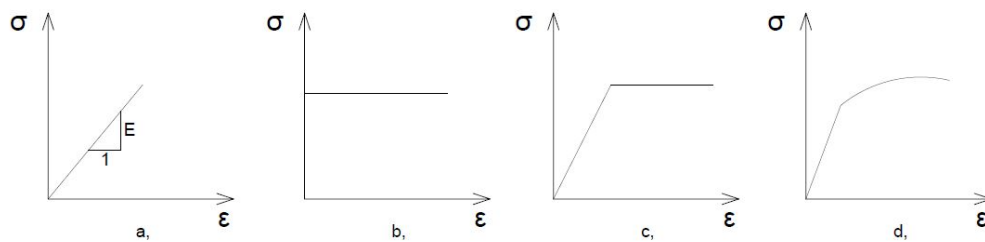


Figure 5.1. Material behavior for the different constitutive models by means of stress-strain curves: a, linear elastic behavior b, perfectly plastic behavior c, linear elastic - perfectly plastic behavior and d, hardening behavior (with softening).

It is the aim of the modelling which determines the constitutive models to be used. For example for a simple convergence analysis the linear elastic model (see Fig. 5.1) can be chosen, which only relies on two input parameters, namely the Young's modulus and the Poisson's ratio.

Poisson's ratio

The Poisson's ratio is used to describe the phenomena when the material experiences deformation in directions normal to the main direction of stretching or compression (axial) and can be quantified as the ratio of the strain in the normal direction and strain in the axial direction [Gourvenec, 2011]:

$$\nu = \frac{-\Delta\epsilon_3}{\Delta\epsilon_1} \quad (5.1)$$

It is important to note that the relation is only true in uniaxial stress states. For the most commonly used materials the Poisson's ratio ranges from 0-0.5; for sands 0.1 to 0.3-0.4, for unsaturated clay 0.1 to 0.3, for saturated clay 0.4 to 0.5 [Bowles, 1996].

Stiffness parameters

The Young's modulus is a parameter showing the relation between the stresses and strains, describing the elastic behavior of materials. As it can be seen in Fig. 5.1 a, E is the steepness of the stress-strain curve in the elastic region, given by the following expression in cases of uniaxial stress states:

$$E = \frac{\Delta\sigma}{\Delta\epsilon} \quad (5.2)$$

It is very important to note that the stiffness of the material is described by the Young's modulus, i.e. the slope of the stress-strain curve. For the linear elastic and Mohr-Coulomb

models only two stiffness parameters, the Young's modulus and the Poisson's ratio, needs to be defined, while some more advanced models like the hardening soil model needs more stiffness parameters. It is crucial to carefully choose the stiffness parameters, especially when the used model uses only one stiffness parameter, as in some cases materials exhibit non-linear behavior right from the onset of loading [Kumarswamy, 2016].

According to [Kumarswamy, 2016] these additional stiffness parameters can be (see Fig. 5.2):

- E_0 , the initial slope of the σ - ϵ curve, i.e. the tangent modulus (can be used if the material has an immense linear elastic range [Kumarswamy, 2016]),
- E_{50} , the stiffness at 50% of the strength of the material, i.e. the secant modulus (often used for primary loading instead of E_0),
- E_{ur} , the unloading-reloading modulus (mainly used for tunnels/excavations),
- E_{oed} , the oedometric modulus, determined from a special oedometric test and can be calculated as follows [Kumarswamy, 2016]:

$$E_{oed} = \frac{(1 - \nu)E}{(1 - 2\nu)(1 + \nu)} \quad (5.3)$$

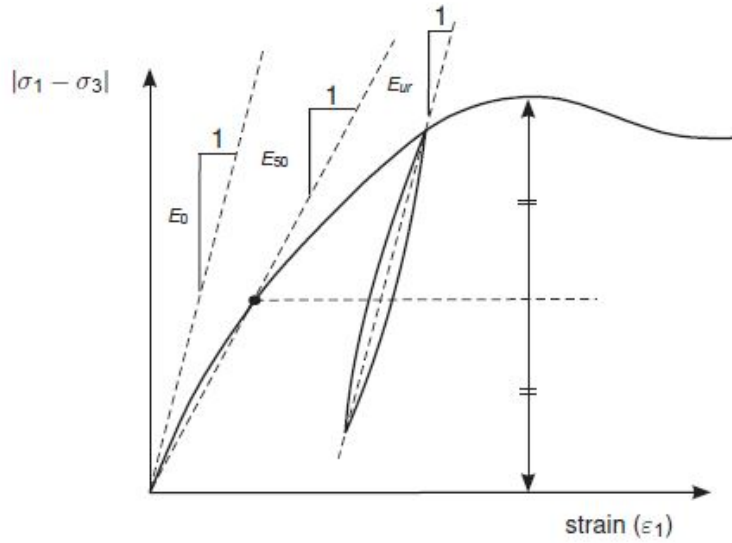


Figure 5.2. Different stiffness and their explanation [Kumarswamy, 2016].

As mentioned before the choice of constitutive model depends on the aim of the investigation. In case of the dynamic analysis of the constructed model, it is of main importance to be able to model the change of stiffness which first and foremost needs a precise determination of the stiffness parameters. In such cases models with one stiffness parameter will not be able to grasp the real-life behavior of soils. In addition to the multiple stiffness parameters, advanced models also account for the stress/strain level and stress path dependent nature of the stiffness [Kumarswamy, 2016], which is another crucial phenomena to take into account during design. This will be further discussed in the Hardening soil model chapter.

5.1.1 Mohr-Coulumb model

Soils subjected to moderate to high loading tend to behave in a non-linear way as significant plastic behavior occur. To model such behavior, the linear elastic model isn't suitable, models that take into account the non-elastic behavior of soils need to be established.

As a first approximation the Mohr-Coulumb model is commonly used in geotechnical designs thanks to ability to deliver results with sufficient accuracy and reliability while keeping the amount of input parameters needed for the model minimal. The model requires 5 parameters, which are easy to obtain from basic soil sample tests [Kumarswamy, 2016]. These parameters are:

- E , Young's modulus [MN/m^2],
- ν , the Poisson's ratio [-],
- c , cohesion [kN/m^2],
- ϕ , the friction angle [$^\circ$],
- ψ , the angle of dilatation [$^\circ$].

The model approximates the real soil behavior assuming linear elastic - perfectly plastic behavior with the Mohr-Coulumb failure criterion implemented in the model as well. For smaller loads the model shows elastic behavior assuming Hooke's law, while for load levels over the point of yielding the model shows non-associated perfect plastic behavior [Andersen, 2017]. The Mohr-Coulumb failure criterion can be seen in Fig. 5.3.

In the elastic region before the yielding point in Fig. 5.1 c, reversible strains develop, meaning that in case of an unloading inside the elastic region the material doesn't suffer irreversible deformation, the original, unloaded state can be regained. Unloading a material is always an elastic process. As the yield point is reached and plasticity begins, irreversible plastic strains start to develop. As the MC model doesn't account for hardening, it has a fixed yield surface in the principal and deviatoric stress space [Andersen, 2017].

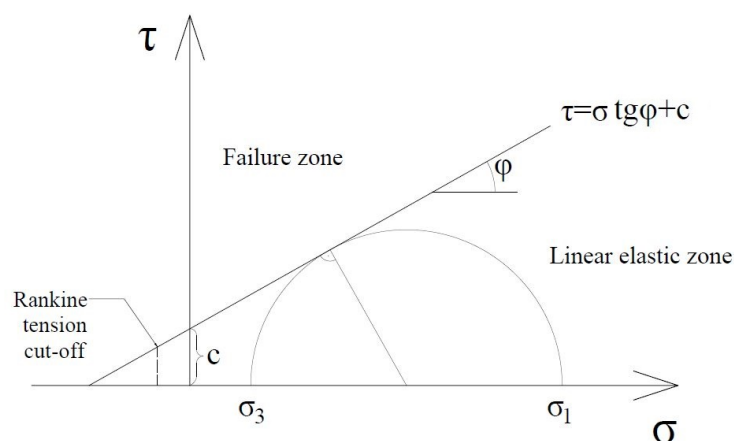


Figure 5.3. The Mohr-Coulomb failure criterion.

As it can be seen in Fig. 5.3, the elastic zone can be found inside, allowing purely elastic behavior and the development of reversible strains. The expression $\tau = \sigma \tan \phi + c$ gives the

shear strength (τ) based on the applied normal stress (σ), friction angle (ϕ) and cohesion (c). σ_1 and σ_3 are the biggest and smallest principal stresses, components of the stress tensor in a state when the shear stress components equal to zero. As mentioned before the Coulomb failure criterion assumes non-associated plasticity in shear failure, meaning that the friction angle does not equal to the dilatation angle ($\phi \neq \psi$). Even though in general soils have little or almost no tensile strength both in drained and undrained conditions (both for sands and clays), the MC failure criteria allows a small tensile strength for soils (see: Fig. 5.3). By implementing the associated Rankine failure line criteria, the tension cut-off, this tensile strength can be limited. Doing so two failure criterion are created; one assuming associated, the other non-associated criteria. The value for the tensile strength, σ_t is set to 0 by default, as soils can't withstand significant tension. As for the dilatation angle, according to [Bolton, 1986] and [Houlsby, 1991] for sands with a friction angle greater than 30° the following expression should be used to determine the dilatation angle:

$$\psi = \phi - 30^\circ \quad (5.4)$$

Limitations

Due to the simplicity of the model, the MC model is suitable for initial or feasibility studies and can be used in a limit state analysis used in design situations. But to capture important features of the real soil behavior for more complicated load conditions the model is insufficient [Kumarswamy, 2016]. The model doesn't account for [Kumarswamy, 2016]:

- Shear and compression hardening, as the yield surface is fixed in the deviatoric and principal stress plane and hence cannot be expanded.
- Stress, strain and stress-path dependency of the stiffness or anisotropic stiffness (for an explanation for the anisotropic stress problem see: chapter 3.2.2). It is to be noted that in the Plaxis MC model linearly increasing stiffness with the depth can be implemented, giving more precise results than by assuming constant stiffness.
- Increase of shear strength with the depth.

5.1.2 Hardening soil model

This model is a more advanced Plaxis model compared to the previously mentioned, and the calibration requires 13 parameters in total. Several reference values of different stiffness parameters are needed because unlike the MC model, the HS model accounts for the stress-dependency of the stiffness. These parameters are [Kumarswamy, 2016]:

- E_{50}^{ref} , secant stiffness [MPa],
- E_{ur}^{ref} , unloading/reloading modulus [MPa],
- E_{oed}^{ref} , oedometer/tangent modulus [MPa],
- m , power for stress-dependency of stiffness [-],
- ν_{ur} , Poisson's ratio of unloading-reloading, by default $\nu_{ur}=0.2$ [-],
- p^{ref} , reference stress, usually set equal to 100 [kPa],
- R_f , failure ratio, by default $R_f=0.9$ [-],
- c , cohesion [kPa],
- ϕ , the friction angle [$^\circ$],
- ψ , the angle of dilatation [$^\circ$].

In plaxis by default $E_{ur}^{ref}=3E_{50}^{ref}$ and $E_{50}^{ref}=E_{oed}^{ref}$ in case the user only defines E_{50}^{ref} [Kumarswamy, 2016]. As it can be seen the HS model uses reference values of the stiffness. For example the reference secant stiffness can be obtained in the following way from the triaxial test results according to [Kumarswamy, 2016]: the value of the minor principal stress is set equal to the reference stress, $-\sigma'_3=p^{ref}$, after which the secant stiffness can be obtained in the same way as before (see: section 5.1) at a cell pressure equivalent to p^{ref} , the reference stress. The procedure is similar for obtaining E_{oed}^{ref} , but the oedometer tests results are used and instead of σ'_3 , σ'_1 is set equal to the reference stress as we consider primary loading. Knowing the reference values Plaxis can calculate the updated stiffness values at the different stress levels based on the following formula [Kumarswamy, 2016] (note that the same formula applies for the unloading/reloading stiffness parameter, as for the oedometer stiffness σ'_3 changes to σ'_1 in the equation):

$$E_{50} = E_{50}^{ref} \left(\frac{c \cos \phi - \sigma'_3 \sin \phi}{c \cos \phi + p^{ref} \sin \phi} \right)^m \quad (5.5)$$

where m is the power of stress dependency and ranges from 0.5 to 1. 1 is used for soft, while 0.5 is used for hard soils. The shape of the failure surface also depends on the parameter: with $m=1$ the MC failure line stays straight, for smaller values it is curved [Andersen, 2017].

The model can also account for the so called dilatancy cut-off, meaning if the option is checked and both the minimum and maximum void ratio is given as input parameters, once the maximum void ratio is reached and the soil reaches a state of critical density, the dilatation angle is set equal to 0 as the dilatancy comes to an end [Kumarswamy, 2016].

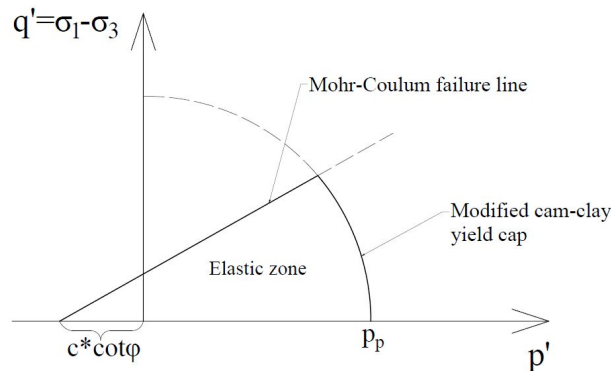


Figure 5.4. The yield surfaces present in the Hardening soil model.

A big difference between the MC and the hardening soil model is that the latter can account for both shear and compression hardening due to the fact that it couples two yield surfaces together (see: Fig. 5.4): the Mohr-Coulomb's and the modified cam-clay's (introducing a yield "cap" surface), of which the former accounts for the previously mentioned shear hardening and non-associated plasticity, while the latter accounts for the volumetric hardening and associated plasticity [Andersen, 2017]. Shear hardening models the irreversible plastic strains due to primary deviatoric loading, while volumetric (compression) hardening models the irreversible strains caused by primary loading due to

oedometer and isotropic loading [Kumarswamy, 2016]. The model uses isotropic hardening, meaning the yield surface expands to the same extent in all directions.

The plastic behavior of materials mentioned in section 5.1.1 still applies; both the elastic nature of the unloading/reloading (between points B and C) and the irreversible plastic strains (ϵ^p) once the yield point has been passed (A) can be seen in Fig. 5.5. An explanation for the hardening phenomena can also be seen in Fig. 5.5. After the elastic loading the material yields in point A (σ_{y0}), after which, unlike in the MC model, hardening occurs, meaning the yield surface expands (not fixed in the deviatoric space anymore), therefore in case of an unloading and then reloading the yield stress increases (to σ_y , point B) [Ottosen, 2005].

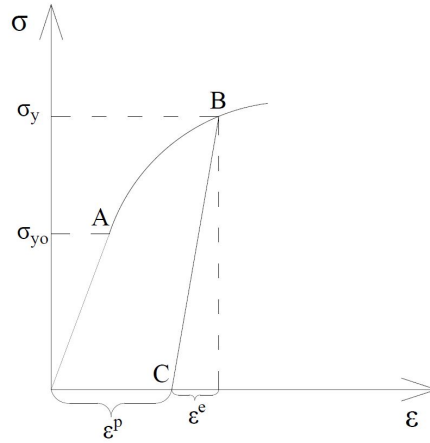


Figure 5.5. Explanation of the hardening phenomena, based on [Ottosen, 2005].

Limitations

Even though the HS model gives a more precise reproduction of real soil behavior, it misses many important features, like [Kumarswamy, 2016]:

- softening due to soil dilatancy,
- the modelling of hysteric and cyclic behavior,
- the ability to distinguish between small stiffness at large strains and large stiffness at small strains.

5.1.3 Hardening soil model with small strain stiffness

The HS small strains model treats some of the problems of the HS model, as it can be used to model cyclic loading as well and accounts for the strain-dependency of the stiffness, the loading history and most importantly the non-linear dependency of the small-strain shear stiffness on the strain amplitude [Kumarswamy, 2016]. In addition to the parameters needed for the HS model, two additional parameters are used in the HS small strain model to model the strain-dependency of the stiffness [Kumarswamy, 2016]:

- G_0^{ref} , the initial shear modulus (at very small strains) [MPa],
- $\gamma_{0.7}$, the shear strain level at which $G_s=0.722G_0$

By implementing these additional parameters in the model, a non-linear unloading-reloading, i.e. a hysteretic behavior can be observed, as the shear stiffness is dependent on the strain level. The reduction of the shear stiffness at small and large strains is different. In case of the former the secant shear modulus (G_s) is normalized with the initial stiffness (G_0), while at large strains the unloading/reloading shear modulus (G_{ur}) is normalized with the initial stiffness. The initial shear modulus is depending on the void ratio of the soil, while the reference initial shear modulus is calculated using eq. 5.5.

Limitations

The Hardening soil model with small strain stiffness is the most advanced material model of the mentioned four, but still lacks the ability to account for the following during cyclic loading [Kumarswamy, 2016]:

- gradual softening and similar to the HS model, softening due to dilatancy effects and debonding,
- the accumulation of irreversible plastic strains,
- liquefaction behavior.

5.2 Model validation based on convergence analysis

5.2.1 Soil parameters

As it was mentioned in section 4.3, the relative density of the soil can greatly influence the response therefore three kinds of sand will be considered in the numerical modelling, namely: loose, medium and dense sands. The soil parameters for each type of sand for the Mohr-Coulomb model can be seen in Table 5.1. The soil unit weight, friction angle and stiffness values were obtained from [GeotechnicalInfo, 2012] and chose according to the soil type.

Table 5.1. The soil and interface parameters inputted for the Mohr-Coulomb model in Plaxis 3D.

| Parameter | Symbol | Loose | Medium | Dense | Unit |
|--|----------------|-------|--------|-------|-------------------|
| Wet soil unit weight | γ | 15.5 | 17 | 18.5 | kN/m ³ |
| Saturated soil unit weight | γ_{sat} | 19 | 20 | 21 | kN/m ³ |
| Young's modulus | E' | 20 | 40 | 70 | MPa |
| Unloading/reloading modulus | E'_{ur} | 60 | 120 | 210 | MPa |
| Poisson's ratio | ν | 0.25 | 0.30 | 0.35 | - |
| Strength reduction factor for interfaces | R_{inter} | 0.68 | 0.68 | 0.68 | - |
| Cohesion | c'_{ref} | 0.2 | 0.2 | 0.2 | kPa |
| Friction angle | ϕ | 30 | 35 | 40 | ° |
| Angle of dilatation | ψ | 0 | 5 | 10 | ° |

Note that the sand layers were assigned 0.2 kPa of cohesion, because Plaxis can predict failure, wrongly, for sand layers with a cohesion of 0 kPa. The additional parameters for the HS and HS small strains model can be seen in Table 5.2 and was chosen based on [Benz, 2007] and [Penzes, 2016].

Table 5.2. The soil parameters inputted for the HS and HS with small strain stiffness model in Plaxis 3D.

| Parameter | Symbol | Loose | Medium | Dense | Unit |
|---------------------------------------|-----------------|--------|---------|--------|------|
| Reference secant modulus | E_{50}^{ref} | 12 | 20 | 28.5 | MPa |
| Reference oedometric modulus | E_{oed}^{ref} | 16 | 25.5 | 35.2 | MPa |
| Reference unloading/reloading modulus | E_{ur}^{ref} | 60 | 72 | 85.6 | MPa |
| Poisson's ratio /unloading-reloading/ | ν_{ur} | 0.2 | 0.2 | 0.2 | - |
| Power of stress dependency | m | 0.75 | 0.65 | 0.55 | - |
| In-situ earth pressure coefficient | K_0^{nc} | 0.44 | 0.42 | 0.4 | - |
| Reference small-strain shear modulus | G_0^{ref} | 168 | 220 | 270 | MPa |
| Shear strain level at $G_s=0.722G_0$ | $\gamma_{0.7}$ | 0.0001 | 0.00015 | 0.0002 | - |

5.2.2 Model set-up

The next phase for the design is to construct the finite element reference model. The cylindrical symmetry of the structure were used, therefore only half of the caisson was modelled to decrease computational times.

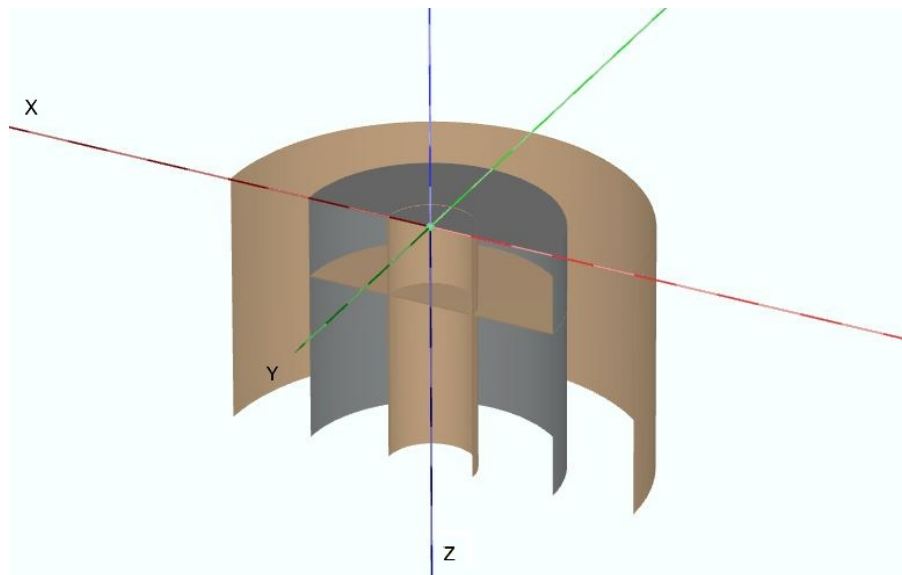


Figure 5.6. The constructed finite element model of the foundation in Plaxis 3D.

The constructed suction caisson model can be seen in Fig. An aspect ratio (L/D ratio) of 1 was used for the validation with $D=6\text{m}$. As the buckling of the foundation is not among the aim of the thesis, the caisson consists of two rigid body elements: one is the bucket lid and the other one is the skirt with a reference point of both at the symmetry line (center) of the caisson. Both positive and negative interfaces for the skirt and only negative interface have been created for the caisson lid to allow the appropriate modelling of the interaction between soil and structure. The strength of the interfaces were reduced by applying a value of 0.68 for R_{inter} , hence reducing both the cohesion, friction angle and the stiffness of the interfaces' [Kumarswamy, 2016]. After the model is constructed, the boundary conditions for the structure need to be set. The defined translation and rotation conditions in Plaxis are summarized in Table. 5.3.

Table 5.3. Translation and rotation boundary conditions for the rigid bodies.

| Direction | Translation condition | Rotation condition |
|-----------|-----------------------|--------------------|
| x | Free | Fixed |
| y | Fixed | Free |
| z | Free | Fixed |

The accuracy of results strongly depends on the mesh configuration of the model. It is essential to study the necessary size of the model, as a model boundary close to the analyzed structure can lead to a wrong, undeveloped failure mechanism, while too wide boundaries can result in large computational times. In addition to the model size, the size and amount of the elements should be controlled, adjacent to the structure, as well as in

the rest of the model. I.e. the size of the area around the foundation which needs finer mesh and the refinement factor of those should be studied and determined.

For the validation of the model dense sand (see Table 5.1) with the linear elastic perfectly plastic model incorporating the Mohr-Coulomb failure criteria will be used. The model is subjected to combine (V, H, M) loading. The aim of this convergence analysis is to validate the model and to check the amount of finite elements (mesh coarseness round the caisson) and size of the model area needed for the results to converge and the failure modes to correspond to the real-life failure behavior under combined loading. For this the expected failure mode has to be known and the obtained bearing capacities need to be plotted against the number of elements to check for convergence .

To determine if the failure modes are correct, already existing test results should be studied. According to [Randolph, 1997] and [Gourvenec, 2011] the failure mode of skirted foundations should show the so-called wedge and scoop failure mode. For skirted foundations with $D > L$, the failure mode can be seen in Fig. 5.7.

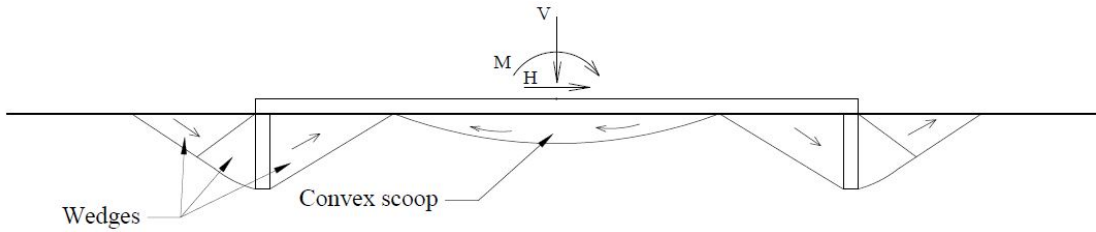


Figure 5.7. Failure mechanism for skirted foundations with $D > L$ based on [Randolph, 1997] and [Gourvenec, 2011,p. 281.].

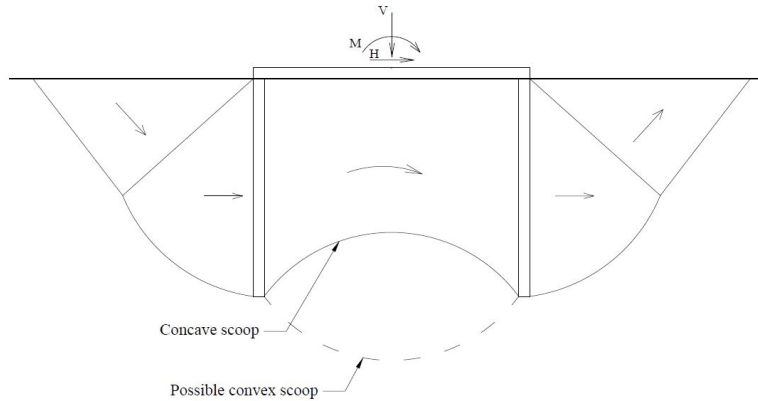


Figure 5.8. Failure mechanism for skirted foundations with $D \simeq L$ based on [Gourvenec, 2011,p. 281.].

[Gourvenec, 2011] extended the aforementioned assumption for skirted suction caissons with an aspect ratio around one ($D \simeq L$). This can be seen in Fig. 5.8. As the subject of the numerical analysis is a suction caisson foundation, the failure mechanism found by [Ibsen, 2010] is to be used as a basis for the model validation (Fig. 5.9). The failure mechanism is valid for caissons subjected to combined loading with $e > 0.3D$, where the eccentricity is calculated by $e = \frac{M}{V}$ and D is the diameter of the caisson.

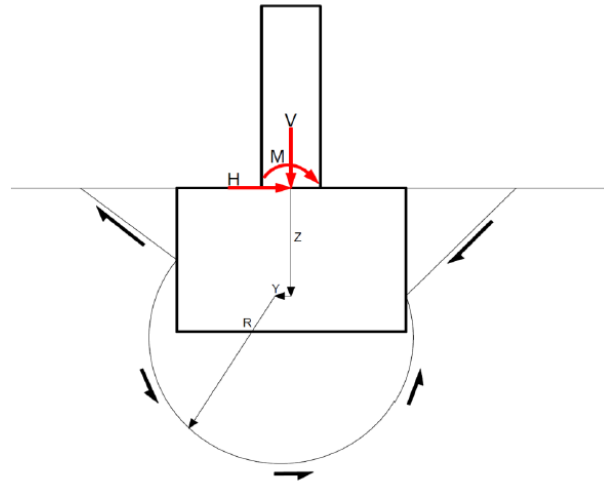


Figure 5.9. Failure mechanism for suction caissons by [Ibsen, 2010].

In order to allow the associated failure mechanism to develop in Plaxis, an additional phase needs to be added after the loading phase with the calculation type set to safety analysis. If the method is selected, the calculation of a global safety factor is conducted by means of the so-called phi/c reduction method (strength reduction method) [Kumarswamy, 2016]. The strength parameters; $\tan \phi$ and c are progressively reduced until failure occurs. Then based on the following formula, the safety of factor can be determined [Kumarswamy, 2016]:

$$\sum Msf = \frac{\tan \phi_{input}}{\tan \phi_{reduced}} = \frac{c_{input}}{c_{reduced}} = \frac{s_{u,input}}{s_{u,reduced}} \quad (5.6)$$

The safety analysis conducted on the model is used to check the effect of the model sizes on the obtained failure mechanism. Model sizes of:

- 12D in the x , half, 6D in the y direction and 3L in the z direction (based on the Plaxis tutorial for suction piles [Kumarswamy, 2016]) as a basis, which corresponds to a model size of $72 \times 36 \times 18$ in the reference case,
- then $72 \times 36 \times 36$ to check if 3L is sufficient in the z direction,
- $30 \times 15 \times 15$, $40 \times 20 \times 20$, $50 \times 25 \times 18$, $60 \times 30 \times 18$, models with smaller depth and
- $60 \times 30 \times 30$ and $100 \times 50 \times 50$

are considered. Note that the model dimensions in the y direction are half of the x directions', as only half of the foundation is modeled.

Once the sufficient model size has been studied and obtained, the second step is to determine the ultimate bearing capacities for different mesh refinement factors, so that the convergence can be studied /the shape of the failure mechanism is studied once again as well/. For this the Plastic calculation option is used in Plaxis with the value of $\sum Msf$ set to 1, which corresponds to the depletion of the capacity, the failure of the soil. The applied load has to be bigger than the ultimate bearing capacity so that the corresponding M_{stage} values can be read and the bearing capacities can be obtained.

For both the safety and plastic calculations combined loading are used, keeping the ratio of the H,V and M loads. The loads are chosen from a range of typical wind turbine loads mentioned in the introduction of Chapter 4 (Table 5.4). A ratio of 1:1:33 for H:V:M is to be used, and as the used bucket dimensions are smaller than of typical suction caissons, smaller loads are used as well.

Table 5.4. Typical and used design loads for offshore wind turbines.

| | H [MPa] | V [MPa] | M [MN m^2] |
|---|-----------|-----------|-----------------|
| Typical values | 4-9 | 6 | 150-250 |
| Used values to obtain $\sum M_{stage}$ | 1 | 1 | 33 |
| Used values to obtain maximum deformation | 0.1 | 0.1 | 3.3 |

Several loading phases are defined for the analysis. The first, initial phase, uses the K_0 -procedure, during which effective stresses are generated based on the in-situ earth pressure coefficient. The second phase is the installation phase, in which all the rigid bodies and interfaces are activated, without any loads activated. Then two phase groups are considered, both groups starting with phase 2. The first one is the plastic calculation, which is used to determine the $\sum M_{stage}$ values and the maximum deformations. The second group consists of a plastic analysis with smaller loads (so that failure is not reached) and a safety analysis to allow for the study of the failure mechanisms. In both cases only the vertical load is applied in a separate phase, after which the horizontal and moment load is applied as well.

5.2.3 Failure mechanism analysis

Comparison between the failure mechanisms is made by means of total deviatoric strains. It should be pointed out that the same colour scale is used for the compared models in the report in order to ensure comparability. In this case this means in the range of -0.05 to 1 for the total deviatoric strains. First the models are checked without applying any mesh refinement for the model (mesh coarseness=1). As for these models the failure mechanism is not developed entirely hence making the comparisons impossible, see Fig. 5.10 and Fig. 5.11, the following method is used to define a finer mesh around the foundation:

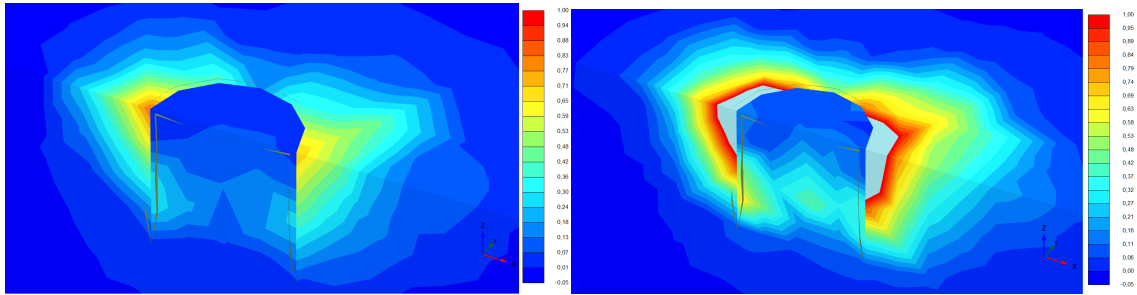


Figure 5.10. Failure mechanism without mesh refinement for $60 \times 30 \times 18$ by means of total deviatoric strains.

Figure 5.11. Failure mechanism without mesh refinement for $60 \times 30 \times 30$ by means of total deviatoric strains.

According to the tutorials manual created by [Kumarswamy, 2016], a surface should be created around the caisson, without assigning any material to it, with a diameter of $3D$ and length of $1.5L$ (see Fig. 5.12), where D and L is the diameter and length of the model caisson respectively, to create a finer mesh volume around the structure. The failure mechanism is well in between the boundaries of the created surface, so the radius of mesh refinement should be enough to provide significant precision.

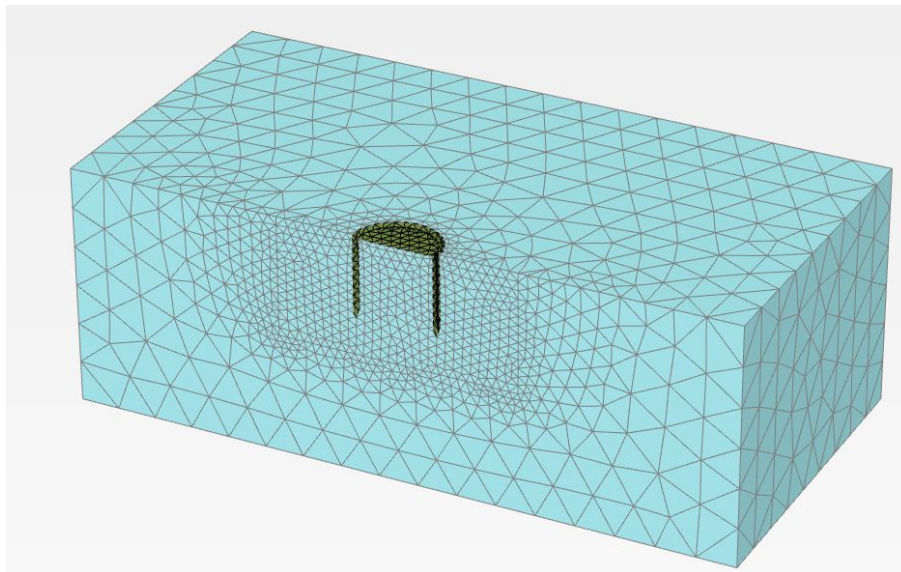


Figure 5.12. The generated mesh using medium element distribution and a mesh coarseness factor of 0.2 around the foundation for the $50 \times 25 \times 18$ model.

For the comparison of the models 4 points have been selected on the rigid body caisson: the 4 corners of the foundation on the x - z symmetry plane. The coordinates of the points can be seen in Tables B.1 and B.2 of the Appendix. Out of the 8 examined models all show the main features of the expected failure mechanism, but with different ranges for the total deviatoric strains, different values for the displacements at the corner points (using the load combination in the bottom line of 5.4) and for the bearing capacities. The results of the calculations can be seen in Tables B.1 and B.2 and in Fig. 5.14.

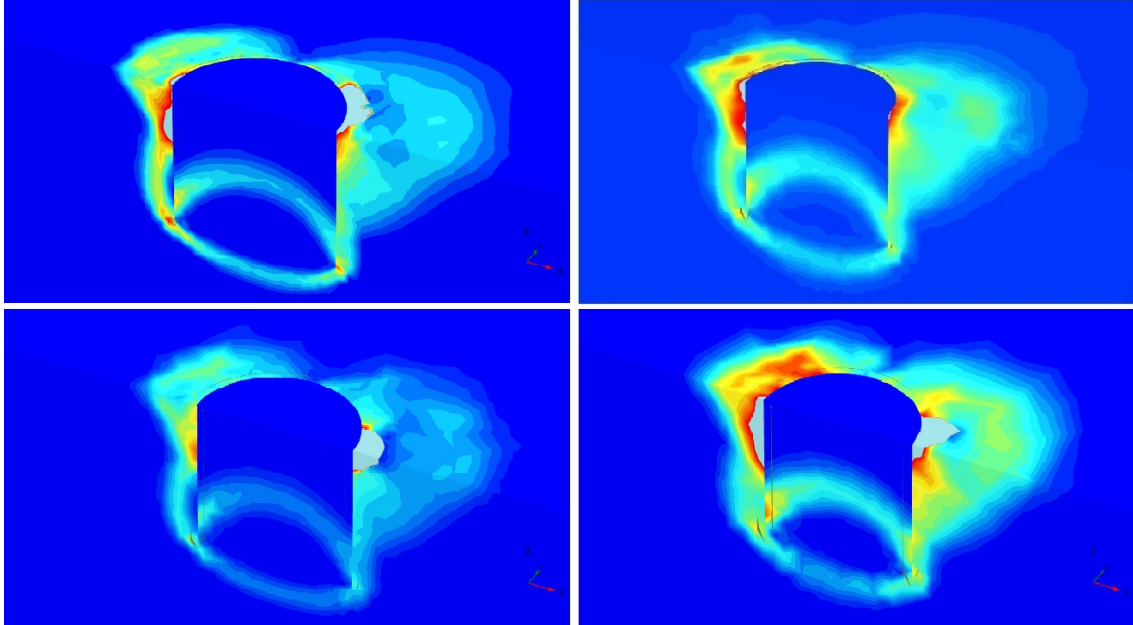


Figure 5.13. The failure mechanism given by the models by means of total deviatoric strains (the models which are to be considered based on the strain values). The corresponding model sizes from top left to bottom left clockwise are: $30 \times 15 \times 15$, $50 \times 25 \times 18$, $60 \times 30 \times 18$, $72 \times 36 \times 18$. The used color scale is the same for all models (0-0.7).

First the models will be compared by means of total deviatoric strains. The $100 \times 50 \times 50$ model give high values of strains (see Tab.B.2), while the $40 \times 20 \times 20$ and $72 \times 36 \times 36$ models give very low strain values compared to the other models. On the other hand all the models give failure mechanisms according to the expected (see Fig. 5.13). However it can be seen that models with not too wide or too narrow ranges of strains give a more detailed failure mechanism. Based on this (and Fig. 5.13) the perfect choice would be either the $30 \times 15 \times 15$, $50 \times 25 \times 18$, $60 \times 30 \times 18$ or $72 \times 36 \times 18$ model size. High maximum total strains can be observed as well, this is due to the nature of the safety analysis. Even though convergence is sometimes obtained after 15 steps, the calculations were run for 100 steps to be able to compare results. Unfortunately this resulted in unexpectedly large strain concentrations on the right side of the caisson's lid and along the upper-third of the left skirt. This made it very hard to determine a unique range of strains for each model. Also taking a look at the values for the $40 \times 20 \times 20$ model, the strain values are unexpectedly low compared to the other models' values. This implies some form of numerical error, as the model should give values closer to the values given by the $30 \times 15 \times 15$ and $50 \times 25 \times 18$ models. It has been noticed that the model is very susceptible to the mesh coarseness factors for different model sizes (and thus the element number), the error can be related to

that. The effect of the number of elements is going to be analyzed in the next, convergence analysis section. Taking a look at Fig. 5.13 the highly strained points can be noticed. Based on the figure and the strain values it can be said that the $50 \times 25 \times 18$ model has the least amount of strain deviation, and also smaller strain speaks can be noticed.

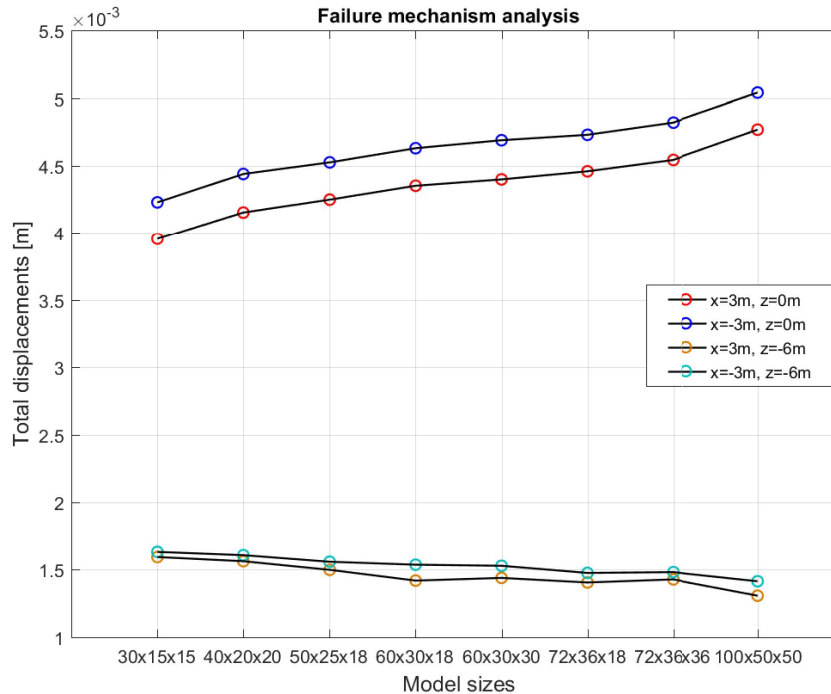


Figure 5.14. Total displacement $||u||$ values for the different model sizes.

Because of the aforementioned the analysis should be conducted based on the bearing capacities and displacements as well. The total displacements of the examined points on the caisson can be seen in Fig. 5.14. The trend is easy to see: by increasing the model size the total displacements of the points at the top of the skirt increase, while the opposite happens to the points at the bottom of the skirt. The figure can be used to pick a model size with a displacement value close to the mean value of the displacements.

Fig. 5.15 shows the obtainable bearing capacities with the different model sizes. Based on the values the $72 \times 36 \times 18$, $72 \times 36 \times 36$ and $100 \times 50 \times 50$ models give too high values compared to the other models. Again choosing a model which gives a value close to the mean value is reasonable.

Based on the comparisons it can be said that the $70 \times 36 \times 18$, $72 \times 36 \times 36$ and $100 \times 50 \times 50$ models can be considered oversized. It can be also observed that going over the suggested 3L model depth by [Kumarswamy, 2016] effects the deviatoric strains and total displacements but no noticeable effect can be noticed on the bearing capacity results. On the basis of the comparisons for the displacements, bearing capacities and total deviatoric strains, the $50 \times 25 \times 18$ model size will be used for further studies.

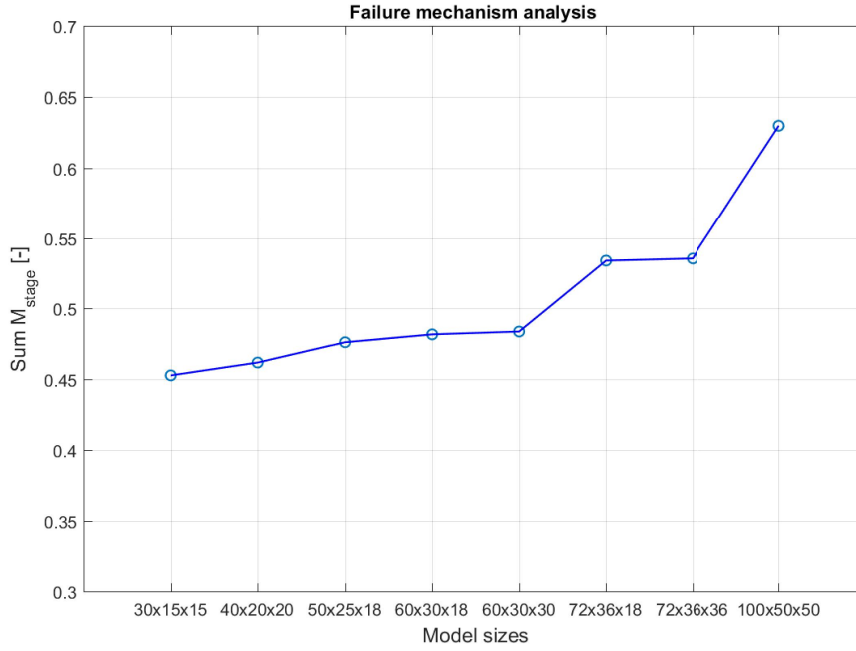


Figure 5.15. Bearing capacities of the different model sizes.

It needs to be kept in mind that the model sizes suggested by [Kumarswamy, 2016] were used for suction piles with an aspect ratio over 1. Therefore to summarize the findings, for suction caissons a model size of $12D \times 6D \times 3L$ (x - y - z direction) can be a good starting point and could give mildly precise results. but to make the calculations faster and more precise, model sizes of $\sim 8D \times 4D \times 3L$ should be used instead for caissons with an aspect ratio of 1. The used model size is in between the one suggested by [Kumarswamy, 2016] and [Thieken, 2013] / $6.67D \times 3.335D \times 3L$ /.

The model size could be even further reduced in the y direction and in the negative direction of x (behind the applied horizontal load) for this case, as the failure mechanism's magnitude behind the load in the x direction is approximately one-third of the one in front of the load, but this reduced model isn't verified and thus not going to be used later in the project.

5.2.4 Mesh convergence analysis - rigid body elements

The $50 \times 25 \times 18$ model is further analyzed for meshes with different number of elements. Mesh coarseness factors of 1, 0.8, 0.6, 0.4, 0.3, 0.2, and 0.1 are used and the corresponding $\sum M_{stage}$ values are read. The failure mechanisms for the models with the different mesh coarseness factors can be seen in Fig. 5.17 and Fig. 5.16. It is to be noted that the same scaling has been used for all models to allow the comparison between the models (strains ranging from -0.02 to 0.5 are shown).

It can be seen that the very coarse models with small number of elements are not able to capture the real life soil behavior sufficiently (see Fig. 5.16). Approximately, models with more than 10000 elements (0.3 mesh coarseness factor) give a more detailed failure mechanisms. Around 18000 elements (0.2 factor) the deviations in the total deviatoric strain values are less, however using large amount of elements (~ 78000 , factor of 0.1)

large strain concentrations can be observed along the caisson's lid.

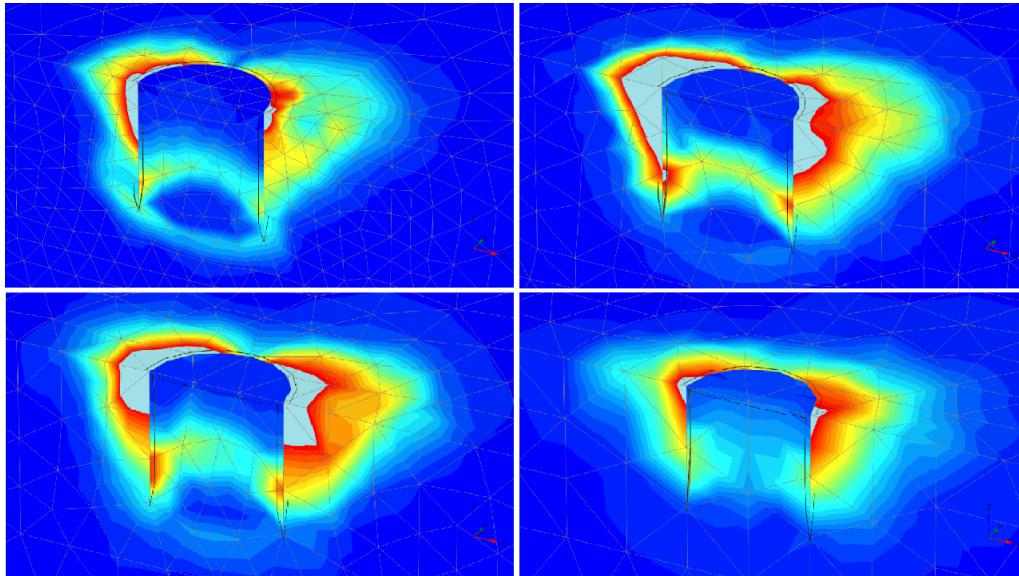


Figure 5.16. The failure mechanisms of the coarse-meshed models with the different mesh coarseness factors/element numbers. Top left: 0.4/8127, top right: 0.6/5669, bottom left: 0.8/5470, bottom right: 1/4747. The same colour scaling is used for all models /-0.02 to 0.5/.

This could be related to interface errors but the model has been checked for different values of R_{inter} and the same can be observed on other models as well. Based on the the aforementioned, the 0.2 mesh coarseness factor could be chosen for further calculations.

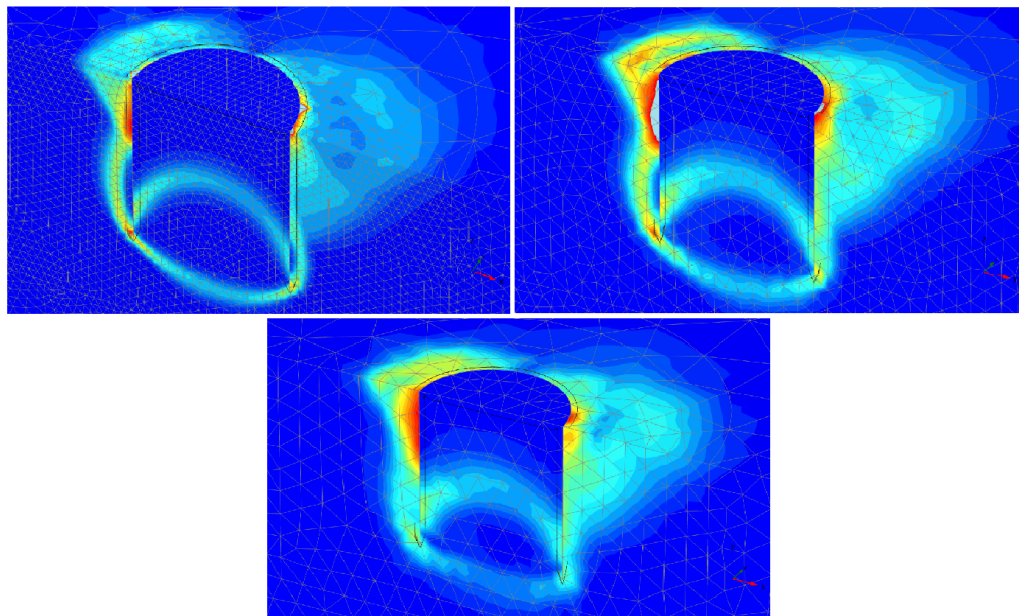


Figure 5.17. The failure mechanisms of the fine-meshed models with the different mesh coarseness factors/element numbers. Top left: 0.1/78792, top right: 0.2/18475, bottom: 0.3/10082. The same colour scaling is used for all models /-0.02 to 0.5/.

Convergence analysis based on $\sum M_{stage}$

Even though the failure mechanism is detailed to a large extent, the model is unable to converge within practical number of elements. The results from the convergence analysis can be seen in Fig. 5.18. After the initial deviation, some degree of convergence can be noticed from an element number of 18000 (mesh coarseness factor of 0.2) approximately. However the convergence is extremely slow and unacceptable. This can be due to numerical problems;

- On one hand 3D models with high number of elements containing rigid body elements can cause calculation error. To overcome this problem, the rigid body elements can be replaced by plate elements. The method is described in the following chapter.
- On the other hand in some cases loading the model until failure using large loads can produce problems as well. In this case the convergence analysis can be conducted by means of maximum displacement of the caisson subjected to a smaller load.

If numerical errors persist to happen, another "solution" can be to compare the bearing capacities obtained from the numerical calculations with capacities obtained from analytical calculations. The formulas described in 3.2 can be used for this. If the capacities show sufficient similarities, then the models can be considered safe to use for further calculations. One problem with this method can be that the "simple" analytical formulas for cases of combined loading are not reliable and accurate enough therefore even well set-up numerical models can be wrongly considered unacceptable if one chooses to validate only based on this method.

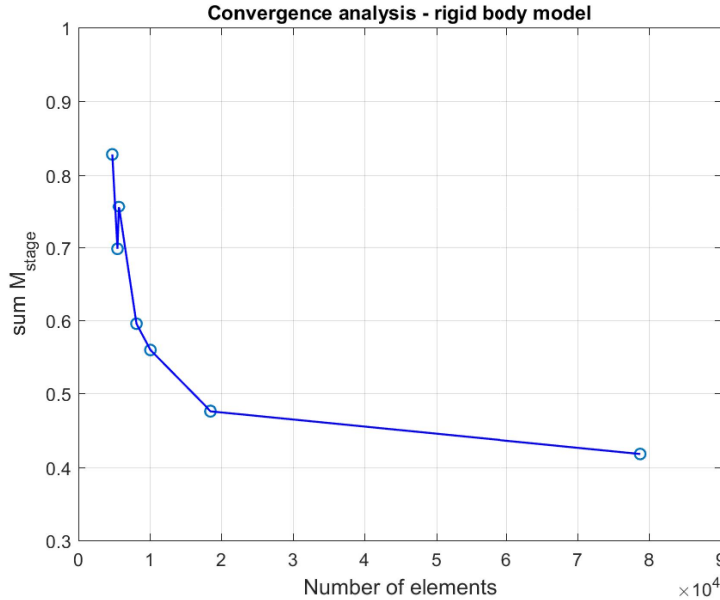


Figure 5.18. Results of the convergence analysis on the model with rigid body elements by means of $\sum M_{stage}$ values.

Convergence analysis based on displacements

As mentioned before the convergence analysis can also be conducted by means of displacements, instead of the bearing capacities. For this again, three points will be selected on the caisson. The coordinates of the chosen points and the corresponding displacement

values can be seen in Table B.3. Unlike the $\sum M_{stage}$ values, the results, which can be seen in Fig. 5.19, converge over an element number of approx. 30000 (mesh coarseness factor of 0.15). The displacement values at the center of the caisson shows a faster convergence compared to the others. The results are acceptable, however calculations can take very long with element numbers over 30000, especially when bigger loads and more complex soil constitutive models are used (as an example, the calculation with 78792 elements lasts about 30 hours).

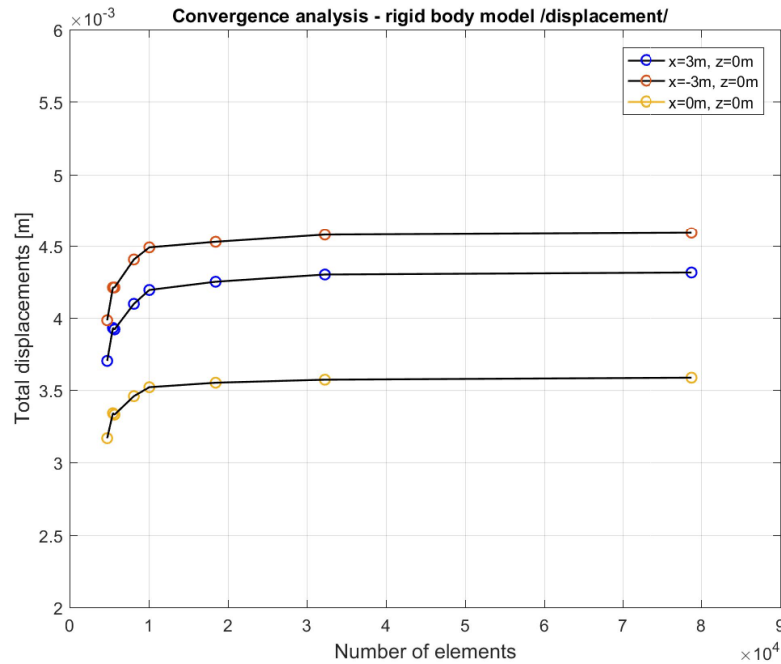


Figure 5.19. Results of the convergence analysis on the model with rigid body elements by means of total displacements $\|u\|$.

5.2.5 Mesh convergence analysis - plate elements

The new model with the plate elements can be seen in Fig. 5.20. The caisson dimensions remained the same but the rigid body skirt is considered as plate element. The material properties are: $E=210$ GPa, $\nu=0.30$, thickness, $d=0.05$ m and density of $\gamma_{steel}=0$ kN/m^3 and $\gamma_{steel}=77$ kN/m^3 . It can be seen in the figure that a 0.5 m thick massless volume is defined on top of the foundation. Without this volume numerical errors occur in the calculations. After examining the output file, the source of this error can be easily identified: the model lacks sufficient contact points between the rigid body lid and the plate skirt. To solve this error the previously mentioned volume is put on the caisson and the skirt (as well as the interfaces) is extended 0.5 m above the seabed. Apart from the thickness, the volume has the same properties as the plate element.

Plate models with different properties are considered in order to analyze the convergence issues. Models with:

- plate density set equal to $\gamma_{steel}=0$ kN/m^3 ,
 - with $E=210$ GPa (steel) and
 - with $E=21$ GPa,
- plate density set equal to $\gamma_{steel}=77$ kN/m^3 (steel) with $E=21$ GPa.

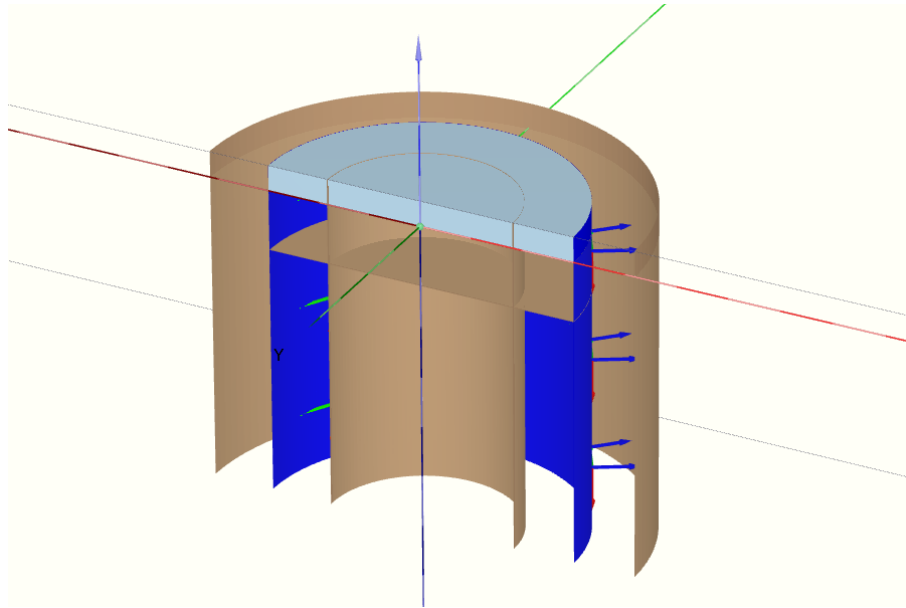


Figure 5.20. The reconstructed finite element model of the foundation with the plate elements in Plaxis 3D.

The density of the plate was set to zero to be able to compare the results with the ones obtained from the rigid body analysis as the rigid body itself is considered massless as well. The model in which the mass of the plate is considered is only used to compare the behavior of the two models with the same stiffness. Obviously the same element numbers and mesh coarseness factors are used for all models. The results of the convergence analysis for both the $\sum M_{stage}$ and maximum displacement values for all models can be seen in Appendix B.2 (Table B.4, B.5 and Table B.6).

Results and conclusions

The results of the rigid body model has been discussed in the previous section therefore this section is focusing on the results of the plate models and the comparison of the results obtained from all 4 model types. In general it can be said that the model caisson consisting of plate elements gives a better convergence rate compared to the rigid body model. Several model tests have been run with plate elements of different stiffness and density and the results show that the higher the foundation stiffness, the lower the obtained bearing capacities and displacements (see Fig. 5.21 for the bearing capacities and Fig. 5.22 for the maximum displacements). This can be used as an explanation for the differences between the capacities and displacements obtained with the rigid body and plate elements, as rigid bodies in Plaxis have very high stiffness compared to the adjacent soil's and also compared to the steel foundation's. Therefore by defining a very large stiffness for the plate elements (for example $E = 10^6 GPa$), the response of the rigid body model can be obtained, however according to [Kumarswamy, 2016] defining a very large stiffness for the plate elements compared to the soil's stiffness can result in numerical errors and can only be done so with caution.

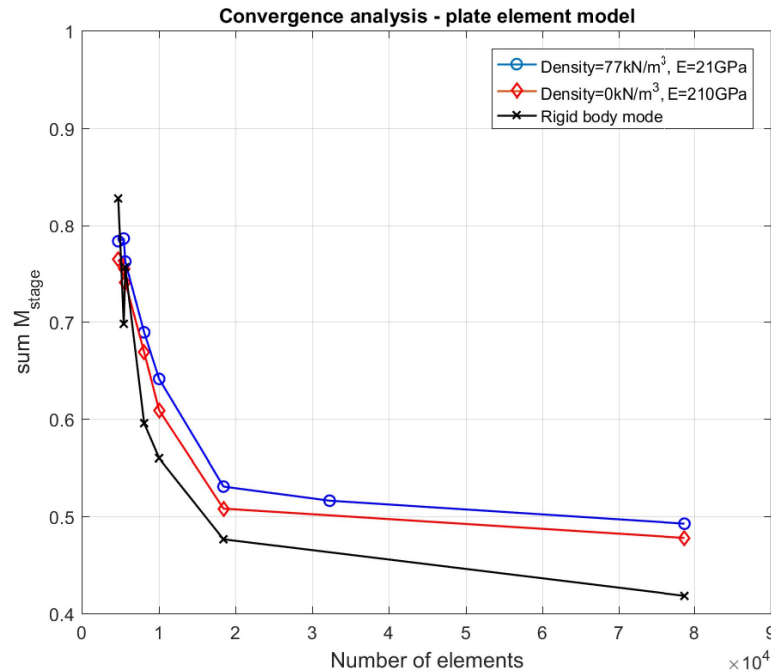


Figure 5.21. Results of the convergence analysis by means of $\sum M_{stage}$ values.

Comparing the plate models with $\gamma_{steel}=77 \text{ kN/m}^3$ and $\gamma_{steel}=0 \text{ kN/m}^3$ (for both $E=21 \text{ GPa}$), it can be seen that even though the density gives additional vertical loading, the deformations decrease at $x=-3 \text{ m}$, $y=0 \text{ m}$ and at $x=0 \text{ m}$, $y=0 \text{ m}$. However for $x=3 \text{ m}$, $y=0 \text{ m}$ the two models give approximately similar displacements. This behavior agrees with the findings of [Houlsby, 2010], that during combined loading the vertical load can enhance foundation response (Fig. 4.3 in Chapter 4).

The analysis was made in order to choose between a model with a certain element number, which will be used for further parametric studies. It can be seen in Figs. 5.23 and 5.24 that the plate model with $\gamma_{steel}=0 \text{ kN/m}^3$ and $E=210 \text{ GPa}$ starts to converge the earliest, at 18475 elements (0.2 mesh coarseness factor) out of all the plate models. The other 3 models, including the rigid body model start to converge around an element number of 32259 corresponding to a mesh refinement factor of 0.15 and fail to keep a steady convergence. Again Fig. 5.22 shows different results, there the $\gamma_{steel}=0 \text{ kN/m}^3$ case with lower stiffness converges over approx. 18000 elements.

But both the deformations and bearing capacities show steadier and faster converge rates for the model with the massless plate elements and also the obtained values are much closer to the rigid body's values while for the other cases the values show a certain amount of deviation. Based on these the massless model with $\gamma_{steel}=0 \text{ kN/m}^3$ can be used for further study with a mesh coarseness factor of 0.2, corresponding to an element number of 18475.

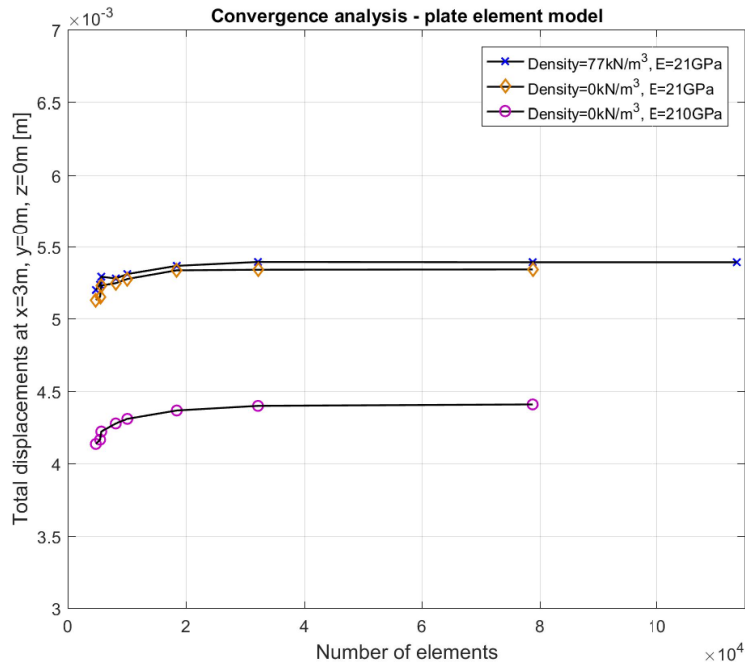


Figure 5.22. Results of the convergence analysis by means of total displacements $[[u]]$ at $x=3$ m, $y=0$ m and $z=0$ m.

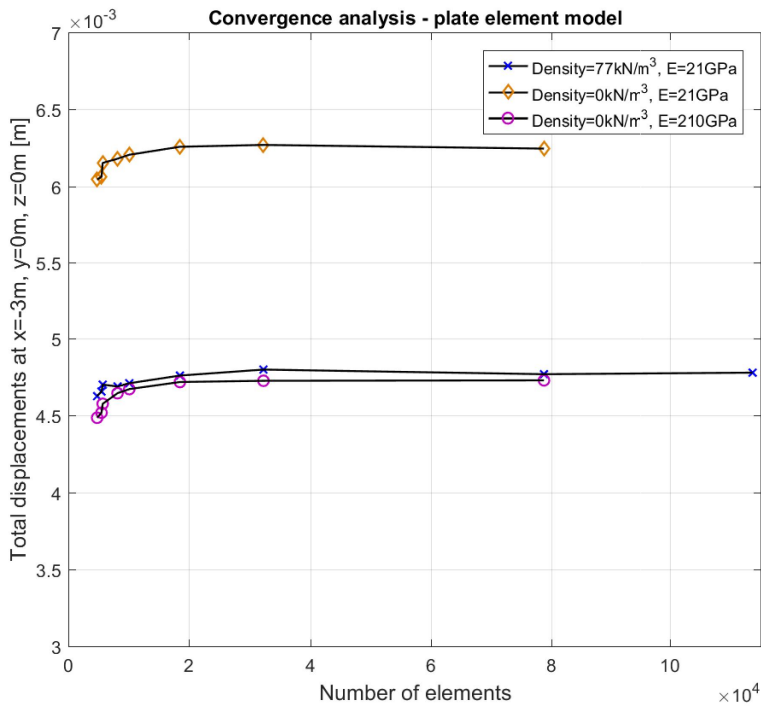


Figure 5.23. Results of the convergence analysis by means of total displacements $[[u]]$ at $x=-3$ m, $y=0$ m and $z=0$ m.

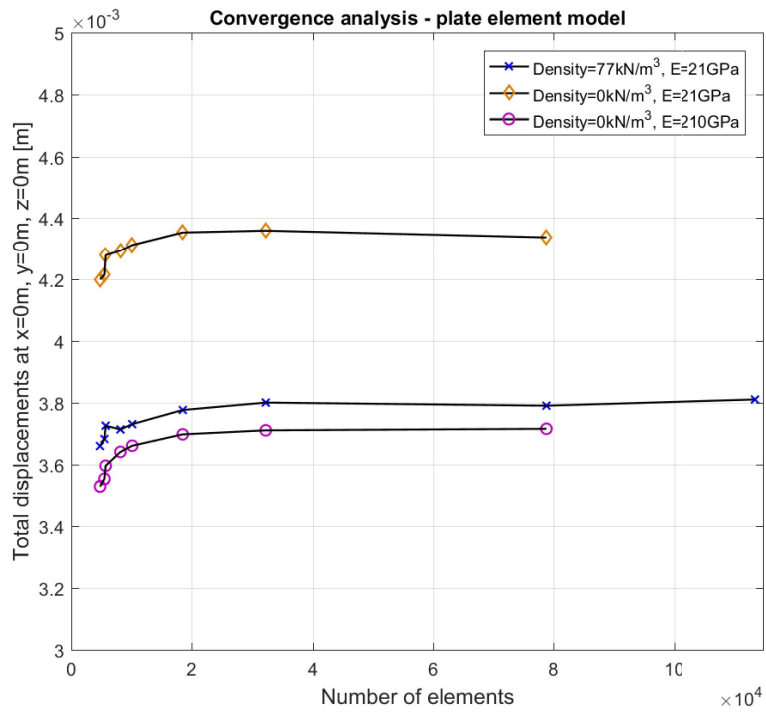


Figure 5.24. Results of the convergence analysis by means of total displacements $||u||$ at $x=0$ m, $y=0$ m and $z=0$ m.

5.3 Model validation based on already validated model

The aim of this section is to check if the model is able to reproduce the results of an already validated model or not. The reference model has been validated by [Thieken, 2013]. In the article the authors were trying to replicate a large scale test conducted in Frederikshavn with the use of numerical modeling by recreating the moment-rotation curve obtained in the field test with different soil (stiffness, friction angle, etc.) parameters. The results of the validation obtained by [Thieken, 2013] can be seen in Fig. 5.25.

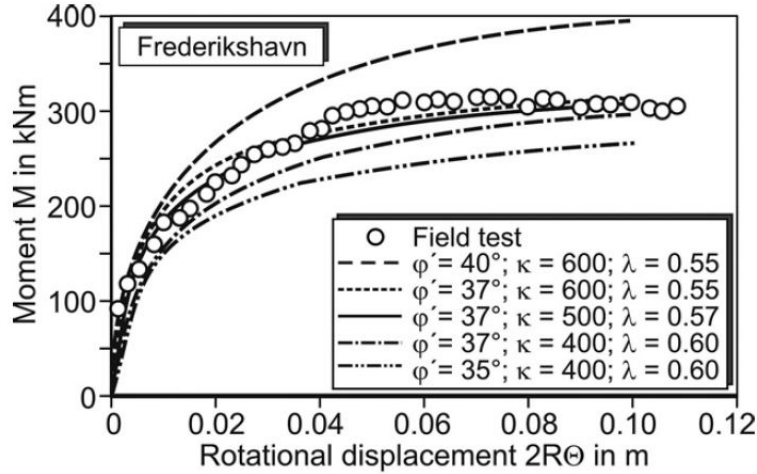


Figure 5.25. Comparison of finite element model and field test results conducted by [Thieken, 2013].

Just like in the study the caisson's geometry is 2×2 ($D=2$ m and $L=2$ m) and made of rigid body elements with a skirt thickness of 12 mm. Rigid body elements were used as the article doesn't account for the effect of the stiffeners on top of the foundation (like the plate element model), which can influence the results to a small extent. As the weight of the caisson's lid and skirt was defined in the study, here the buoyancy reduced weight of the caisson elements is added as additional vertical load. Above the caisson the water is shallow with a depth of 4 m. The test caisson was subjected to combined loading (V, H, M) with a vertical load of 37.3 kN and the horizontal load applied with a lever arm of 17.4 m.

Table 5.5. Soil parameters of the two models for the model validation based on [Thieken, 2013].

| Soil parameters | |
|-------------------------------------|---------------------------|
| Dry soil unit weight [kN/m^3] | 19 |
| Friction angle [$^\circ$] | 37 |
| Dilatation angle [$^\circ$] | 7 |
| Cohesion [kPa] | 0.1 |
| Poisson's ratio [-] | 0.25 |
| Contact friction angle [$^\circ$] | 2/3 of the friction angle |

Two models are created for the comparison using the soil parameters in Table 5.5. The model-set up is according to chapter 5.2 and the optimal, 0.2 value is used for the mesh

refinement factor giving a total of 19340 elements. The contact friction angle is defined by the interface strength reduction factor in Plaxis, which was set equal to 0.66.

Which made it hard to reconstruct the moment-rotation curves was that stress-dependent stiffness has been introduced in the calculations of [Thiicken, 2013]. Linearly increasing stiffness with the depth can be defined in Plaxis, but by doing so the obtained moment capacities are very high compared to the ones in Fig. 5.25 for the used model. As a result of this constant Young's moduli were used; 60 and 100 MPa. The results of the numerical simulations can be seen in Fig. 5.26

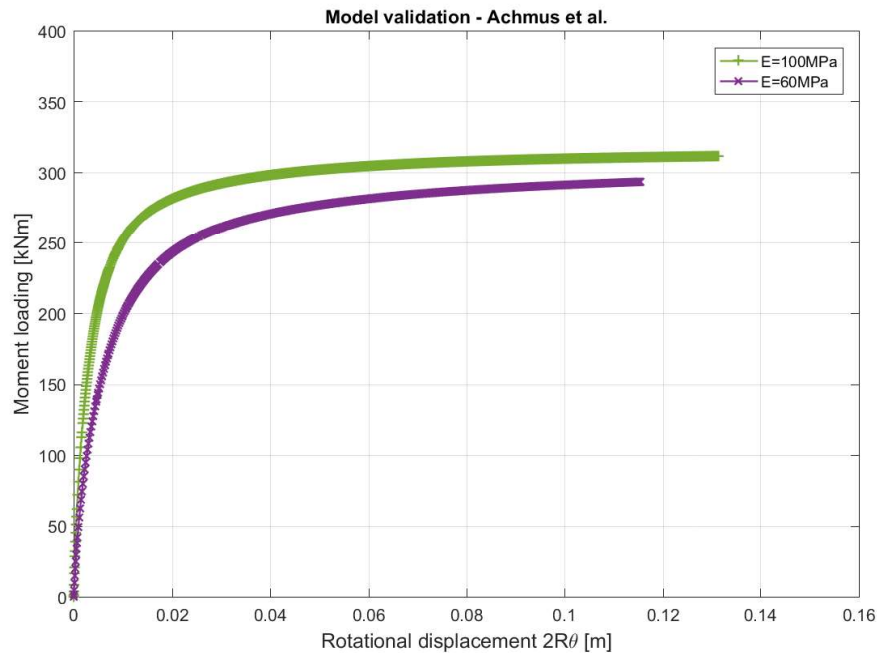


Figure 5.26. Moment-rotational displacement curves obtained from the numerical calculations for the model validation.

By comparing Figs. 5.25 and 5.26 it can be seen that the curve belonging to the model with $E=60$ MPa follows the corresponding curve in Fig.5.25 better. The obtained capacity and maximum rotational displacement, as well as the shape of the curve is very similar to the one obtained by [Thiicken, 2013]. The rotation values were calculated from the relative displacement of the two sides of the caisson lid ($x=1$ m, $y=0$ m and $z=0$ m and $x=-1$ m, $y=0$ m and $z=0$ m).

As the constructed model is able to reproduce the response of a previously validated model, the results obtained later in the study can be accepted and used to make general conclusions for suction caissons.

Numerical study 6

In this chapter a numerical parametric study is conducted based on the previously calibrated models to assess and compare the response of suction caissons subjected to uniaxial and combined loading with different geometries in different soil conditions using the Mohr-Coulomb failure criteria. The study will concern the behavior of caissons with different embedment lengths, diameters and under different vertical loads. After the calibration of the MC and HS soil models, tests will run using HS small strain soil model as well.

Based on the convergence analysis in the previous chapter, it has been concluded that the massless plate elements are to be used for further studies. The buoyancy reduced weight of the caisson elements are included in the vertical loading. Just like for the convergence study, the horizontal load is applied with a lever arm of 33.33 m. The study deals with the long-term, drained behavior.

6.1 Uniaxial loading with Mohr-Coulomb model

First the vertical bearing capacities are calculated for the different aspect ratios so that the response of models with various V/V_{max} values for all three relative densities can be obtained. As the failure mechanism is different for vertical loading and expands below the bottom of the foundation rather than on the two sides of it, the model size which was suggested for caissons with combined loading in the previous chapter has to be increased in the negative z direction (under the caisson). Optionally it can be reduced on the sides to construct a smaller model size and this cut down computation times.

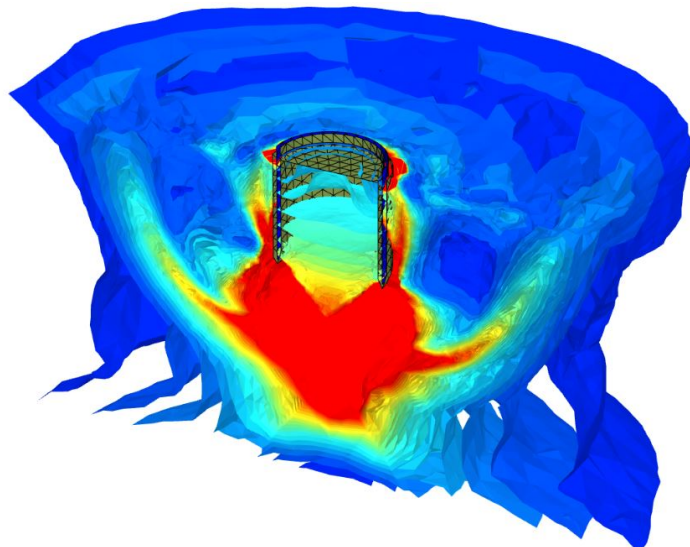


Figure 6.1. Failure mechanism for a suction caisson with an embedment ratio of 1 under vertical loading in dense sand by means of total deviatoric strains.

Fig. 6.2 shows the maximum vertical bearing capacities for the caissons with different

aspect ratios in loose, medium and dense sands. It is important to note that in this case it is the length of the caissons which are modified, meaning that the aspect ratios corresponds to the following skirt length/diameter ratios [m]: 0.25 - 1.5/6, 0.5 - 3/6, 0.75 - 4.5/6, 1 - 6/6. This allows to check the effect of the embeddment length on the response of the caisson. Taking a look at the corresponding values in Tab. 6.1 it can be concluded that the vertical bearing capacities of suction caissons highly depend on the relative density of the soil, while the influence of the aspect ratio is the most significant in dense sands, with the aspect ratio of 1 giving a 273.3 MN (3.7 fold) increase in the vertical capacity compared to the smallest, 0.25 aspect ratio. For the loose and medium dense sands this increase is approximately 3 fold.

The increase of the vertical bearing capacity in dense and loose sand for the smallest and largest embeddment length is also compared. These differences for the different aspect ratios can be seen in Table 6.1. Based on the values it can be concluded that the vertical bearing capacity is strongly influenced by both the embeddment length and relative density.

Table 6.1. Vertical bearing capacity values for caissons with different aspect ratios in loose, medium dense and dense soils.

| Aspect ratio (L/D) | Vert. capacity (loose sand) [MN] | Vert. capacity (medium sand) [MN] | Vert. capacity (dense sand) [MN] | Difference [MN] |
|---------------------------|-------------------------------------|--------------------------------------|-------------------------------------|--------------------|
| 1 | 58.56 | 143.2 | 373.65 | 315.09 |
| 0.75 | 44.28 | 109.41 | 279.12 | 234.84 |
| 0.5 | 31.46 | 79.89 | 190.0 | 158.54 |
| 0.25 | 20.06 | 49.71 | 100.35 | 80.29 |

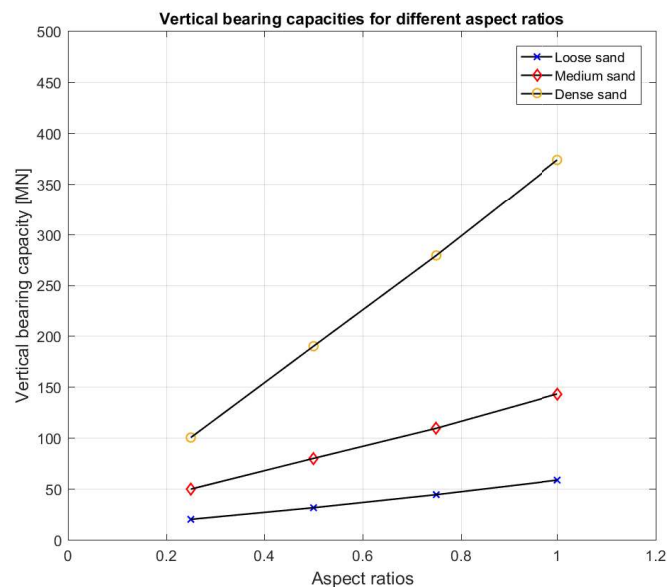


Figure 6.2. Vertical bearing capacities for suction caissons with aspect ratios of 0.25, 0.5, 0.75 and 1.

The explanation is that the shorter the skirt length (the ratio between the skirt length

and lid diameter), the smaller the share of the friction of the total load and the bigger the share of the tip and lid components. And as out of all the load components, the share of the friction is the biggest for drained cases (see: Chapter 4, Fig. 4.6 and 4.7), reducing the skirt length (resulting in smaller surface over which the friction can be assembled) can significantly decrease the bearing capacity.

Figs. C.1, C.2 and C.3 show the load-displacement curves in the Appendix. It is hard to compare the results as the soil fails relatively "early" for the smaller aspect ratios. But by zooming on the curves and checking the initial behavior at smaller load levels it is clear that for the same load level the caissons with smaller embedment lengths give higher vertical displacements. The horizontal displacement for the $H - u_x$ curves are measured at the center point of the caisson lid ($x=0$ m, $y=0$ m, $z=0$ m), while the rotations are calculated from the two sides of the lid in the $x-z$ plane.

As it is expected the caisson in the loose sand gives the highest vertical displacements compared to the caissons in medium dense and dense sands (see: Fig. 6.3). Likewise the loose case gives the least stiff response as it can be seen in Fig. 6.3. However, surprisingly, there is no significant difference between the medium dense and dense sand case regarding the maximum vertical displacements at failure (except with an aspect ratio of 0.5). This can be quite important in SLS analysis.

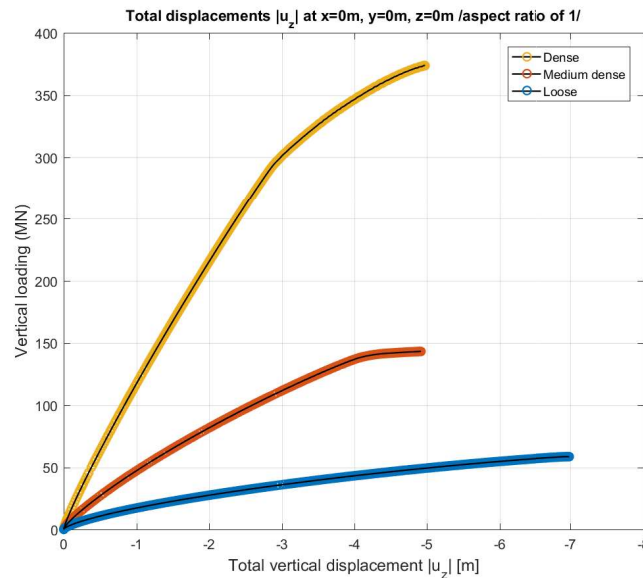


Figure 6.3. Vertical loading-total vertical displacement curves for a suction caisson with the aspect ratio of 1 in loose, medium dense and dense sands.

6.2 Combined loading with Mohr-Coulomb model

As the chapter mainly focuses on the ultimate limit states, the assessment of capacities are of main importance. First different embedment lengths are considered, just like for the vertical bearing capacity. For this the vertical load is set constant ($V=1000$ kN) for each one of the models. Later the results for V/V_{max} values of 0.01, 0.05 and 0.1 will be shown as well, thereby studying the effect of vertical loading on the response of suction

caissons. As the bouyancy-reduced weight of the caissons differ for each aspect ratio, the vertical loads are increased by the weight of the caissons.

6.2.1 Constant vertical load (varying embedment lengths)

First the bearing capacities are analyzed and compared in loose, medium dense and dense sands. The results for the horizontal and moment capacities for the different aspect ratios can be seen in Figs. 6.4 and 6.5 respectively.

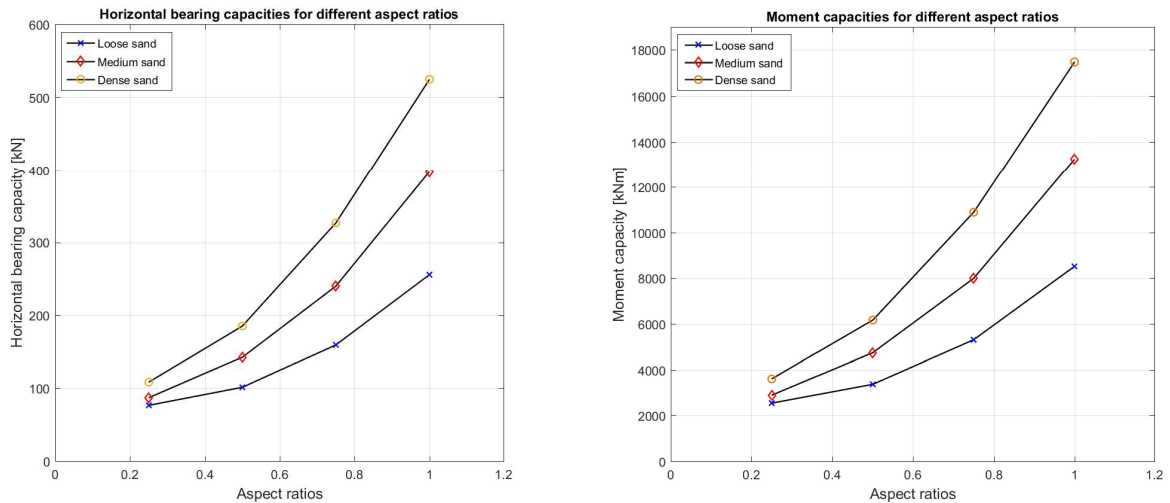


Figure 6.4. Horizontal bearing capacities for suction caissons with aspect ratios of 0.25, 0.5, 0.75 and 1. **Figure 6.5.** Moment capacities for suction caissons with aspect ratios of 0.25, 0.5, 0.75 and 1.

Fig. 6.4 shows an expected increase in the capacities both for denser sands and for bigger aspect ratios. The bearing capacity values for the caisson with an aspect ratio of 0.25 are very similar, the difference between the loose and dense sand is only 31.8 kN (141% increase compared to the). As the aspect ratio, thus the embedment length increases, the difference between the capacities obtained in loose and dense sands gets significantly higher. For the aspect ratio of 1, this difference increases to 268.8 kN (205% increase). The rest of the values can be seen in Table 6.2. Additionally, by increasing the embedment depth, the increase in the bearing capacity gets bigger and bigger; for the dense case: from 1.5 m to 3 m - 75.92, while by extending from 3 m to 4.5 m the increment becomes 141.52.

Table 6.2. Horizontal bearing capacity values for caissons with different aspect ratios.

| Aspect ratio (L/D) | Horizontal capacity (loose sand) [kN] | Horizontal capacity (dense sand) [kN] | Difference [kN] |
|------------------------|---------------------------------------|---------------------------------------|-----------------|
| 1 | 255.6 | 524.4 | 268.8 |
| 0.75 | 159.3 | 326.65 | 167.35 |
| 0.5 | 101.13 | 185.13 | 84 |
| 0.25 | 76.41 | 108.21 | 31.8 |

This leads to a conclusion similar to the case of vertical loading: both the length of the caisson and the relative density has a significant influence on the final bearing capacity also for combined loading.

By taking a look at the displacements and rotations plotted against the continuously increasing loading, the same can be observed (see: Fig. 6.6 for $H - u_x$ and 6.6 for $M - \theta$).

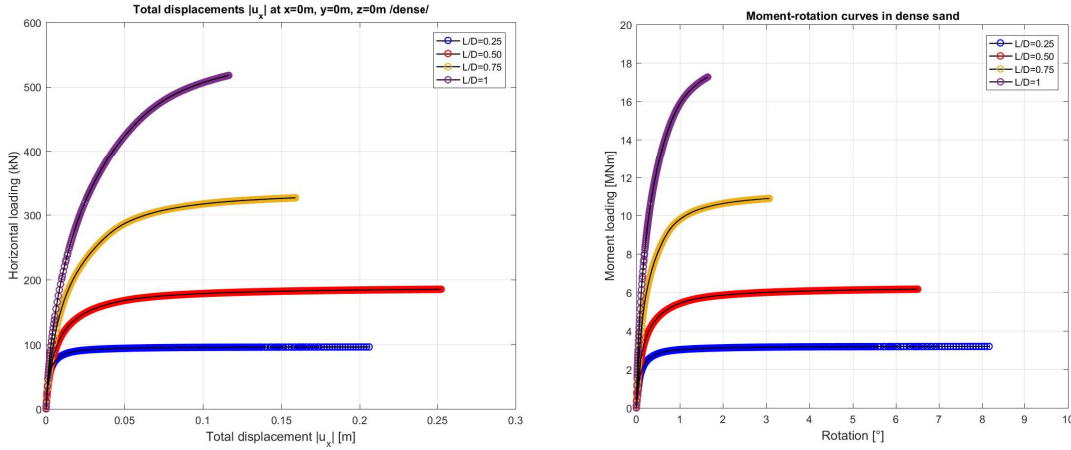


Figure 6.6. Horizontal loading-horizontal displacement curves for suction caissons with aspect ratios of 0.25, 0.5, 0.75 and 1 in dense sand measured at the center of the lid. **Figure 6.7.** Moment-rotation curves for suction caissons with aspect ratios of 0.25, 0.5, 0.75 and 1 in dense sand.

Nevertheless the stiffer response with increasing embedment length can be noticed, resulting in a quite "brittle" response for the aspect ratio of 1 and a more "ductile" for the smaller aspect ratios. Therefore just like for the vertically loaded caissons, it can be seen that for an arbitrary chosen load rate the caisson with the longer embedment depth gives smaller displacements. One explanation is that the longer skirt allows the loads to be distributed at a deeper depth, meaning at a place of higher soil resistance, thus resulting in smaller overall displacements and higher capacities. It is especially true for the caisson rotation.

6.2.2 Different V/V_{max} values

In this section the caisson responses are compared under vertical loads with V/V_{max} values of 0.01, 0.05 and 0.1. The vertical loads are varying while the caissons are still subjected to combined loading (H, M, V). First the bearing capacities are compared, after which the load-displacement, moment rotation curves are to be discussed. In this section the aim is to compare the response in loose, medium dense and dense sands for caissons with an aspect ratio of 1, as well as to check the effect of different embedment lengths in dense sand.

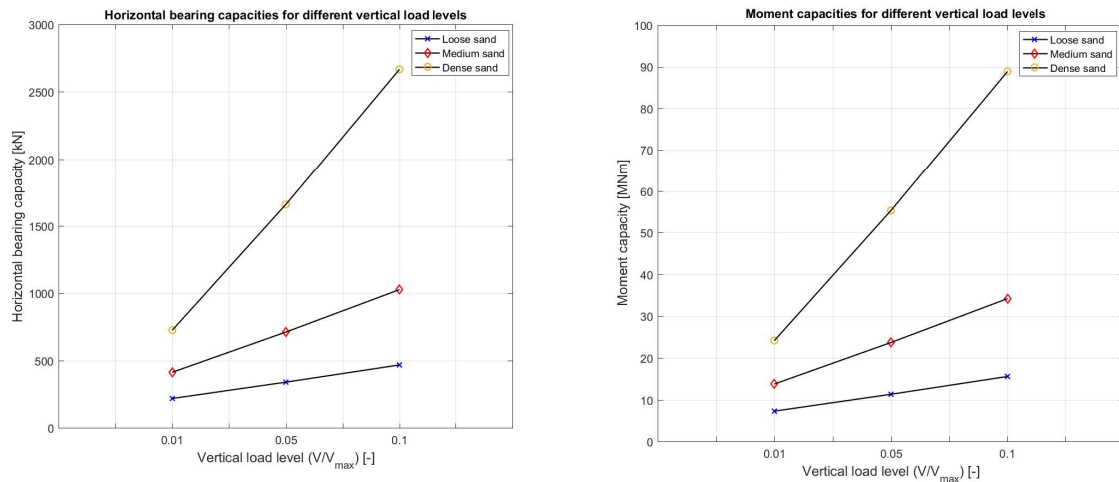


Figure 6.8. Horizontal bearing capacities for suction caissons subjected to different vertical loads in loose, medium dense and dense sands. **Figure 6.9.** Moment capacities for suction caissons subjected to different vertical loads in loose, medium dense and dense sands.

The horizontal and moment capacities for caissons with an aspect ratio of 1 in sands with different relative densities and vertical load levels can be seen in Fig. 6.8 and Fig. 6.9 respectively.

The figures show a very similar response to the vertically loaded caisson's response. Comparing the results in Figs. 6.8 and 6.9 with the results for the constant vertical load (Figs. 6.4 and 6.5), the same can be concluded here as for all the previous results: as the sand gets denser, the effect of the vertical load on the final bearing capacity significantly increases.

To further analyze the results, the total vertical displacements and rotations are plotted against the horizontal and moment loading respectively (Figs. C.4, C.6, C.8 for the $H - u_x$ and Figs. C.5, C.7, C.9 for the $M - \theta$ curves). As the vertical load increases the caisson in the dense sand shows the most striking increase in displacements and rotation, which is reasonable given the fact that the V_{max} values are by far the highest for the dense case hence the highest moments and horizontal loads as well. In medium dense sand the horizontal displacement and rotation slightly increases with increasing vertical load. The caisson shows an interesting behavior in loose sand; a significant increase can be observed in both displacement and rotation between the model subjected to $V/V_{max}=0.01$ and $V/V_{max}=0.05$, however for a vertical load level of $V/V_{max}=0.1$ the displacements decrease to a large extent, while the rotation increases compared to $V/V_{max}=0.05$.

It can be interesting to check how the embedment length influences the effect of the vertical load level. Fig. 6.10 shows the horizontal bearing capacities for models with different embedment lengths subjected to different vertical loads. Based on the figure it can be seen that also the effect of the embedment length increases with increasing vertical load.

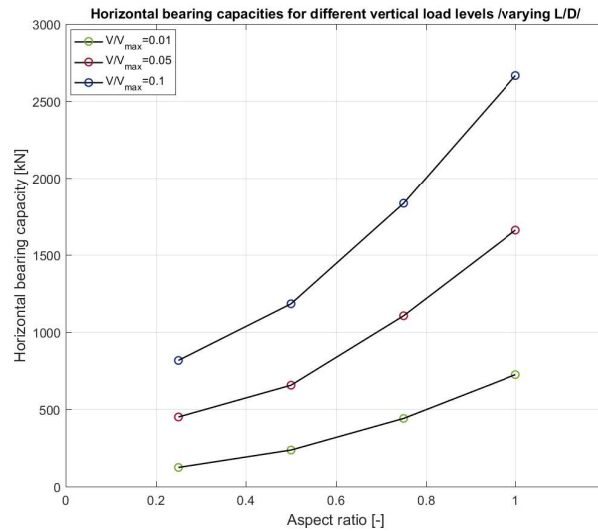


Figure 6.10. Vertical bearing capacities for suction caissons with aspect ratios of 0.25, 0.5, 0.75 and 1, subjected to different vertical loads in dense sand.

The caisson response (load-displacement and moment-rotation curves) with varying vertical loads for the different aspect ratios in dense sands can be seen in the Appendix, Figs. C.10 - C.19. First the different aspect ratios are plotted for V/V_{max} cases of 0.01, 0.05 and 0.1 and compared (Figs. C.10 - C.15), then the results for the different vertical load levels are checked for each aspect ratio (Figs. C.16 - C.19). By raising the vertical load, both the displacements and rotations increase for all aspect ratios. For lower levels of vertical loading the displacements for an aspect ratio of 1 and 0.75 are very similar and lower than the displacements for an aspect ratio of 0.5. With increasing vertical load level, the maximum displacements are in decreasing order (from an aspect ratio of 1-0.25). At higher vertical load levels, with the exception of the smallest caisson, the rotations are almost identical. At lower vertical load levels the smallest caisson rotates to a same extent as the largest one. The smallest caisson shows an interesting response. The larger the vertical load level, the larger the stiffness of response, for a case of $V/V_{max}=0.1$ giving almost the same stiffness as the biggest caisson. By comparing Figs. C.16 - C.19, a more ductile response is observed with increasing vertical load. In overall the displacements and rotations are quite high, in real life, these would be unacceptable and would significantly impair the serviceability of the wind turbines.

6.2.3 Constant vertical load (varying lid diameters)

In the previous section the response of caissons with varying embedment lengths have been assessed. Now the focus is on caissons with constant embedment length and varying diameters. First the bearing capacities are compared in soils of different relative densities for the different aspect ratios. This time the aspect ratios correspond to the following skirt length/diameter ratios [m]: 0.25 - 6/24, 0.5 - 6/12, 0.75 - 6/8, 1 - 6/6. The results for the horizontal and moment capacities for the different aspect ratios can be seen in Figs. 6.11 and 6.12 respectively. The values can be seen in Table 6.3.

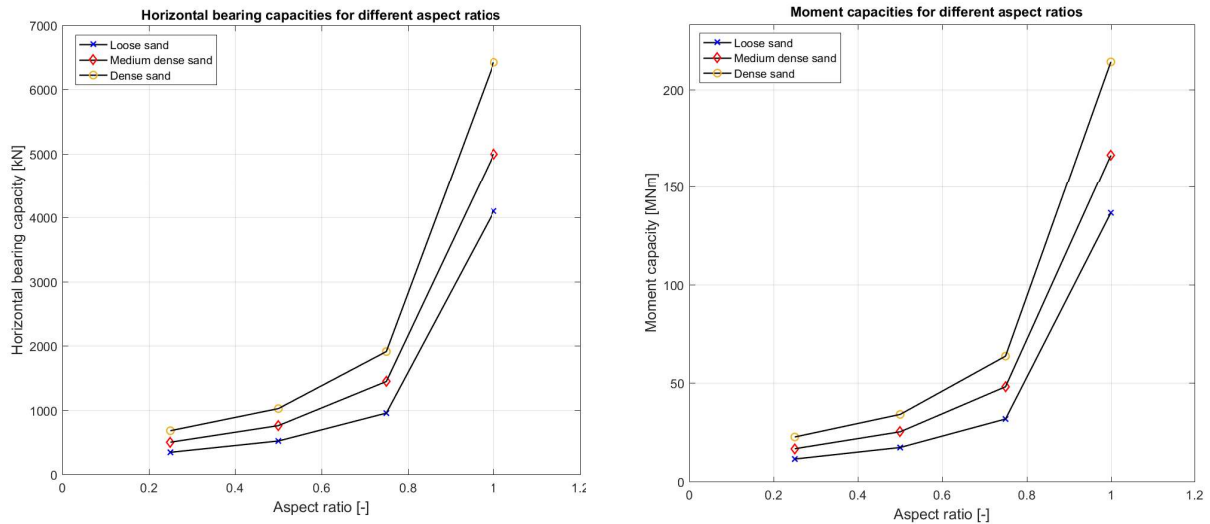


Figure 6.11. Horizontal bearing capacities for suction caissons with aspect ratios of 0.25, 0.5, 0.75 and 1. **Figure 6.12.** Moment capacities for suction caissons with aspect ratios of 0.25, 0.5, 0.75 and 1.

Table 6.3. Horizontal bearing capacity values for caissons with different aspect ratios

| Aspect ratio (L/D) | Hor. capacity (loose sand) [kN] | Hor. capacity (medium sand) [kN] | Hor. capacity (dense sand) [kN] | Difference [kN] |
|---------------------------|------------------------------------|-------------------------------------|------------------------------------|--------------------|
| 0.25 | 343 | 500 | 679 | 336 |
| 0.50 | 519 | 758 | 1023 | 504 |
| 0.75 | 953 | 1445 | 1911 | 958 |
| 1 | 4098 | 4998 | 6423 | 2325 |

Figs. 6.11 and 6.12 show very similar results to Figs. 6.4 and 6.5 for the varying embedment lengths. It is hard to compare the effect of embedment length and diameter, as here the diameters are increased abruptly, compared to the small increase in the embedment lengths. The capacities can be significantly increased by increasing the diameters beyond doubt, giving a much larger increase in the bearing capacities, than by increasing the embedment lengths. But it is important to point out that the amount of material needed to increase the lid diameters are significantly more than what is needed to increase the skirt lengths to obtain the same amount of increase in capacity. For example to obtain an increase of 258 kN in the horizontal capacity on medium dense sand, the diameter needs to be increased by 2 meters (from 6 m to 8 m). Assuming the same thickness for the lid and skirt, this means an increase of 87.92 m^2 . To obtain the same amount of increase in capacity, the skirt length should be increased by 3 meters. This means an increase of 56.52 m^2 . It is interesting to check the effect of the relative density on the results. When the embedment lengths were increased, the relative densities had a huge influence on the obtainable bearing capacities from loose sand to dense sand (probably due to the already explained phenomena - the benefits of increased friction with the longer skirt and dense sand), for the biggest, an aspect ratio of 1, the capacity increased by 205%. While when the diameter is increased, this capacity increase is 157% for the smallest aspect ratio (the

caisson with the largest diameter). The load displacement and moment-rotation curves can be seen in Figs. 6.13 and 6.14.

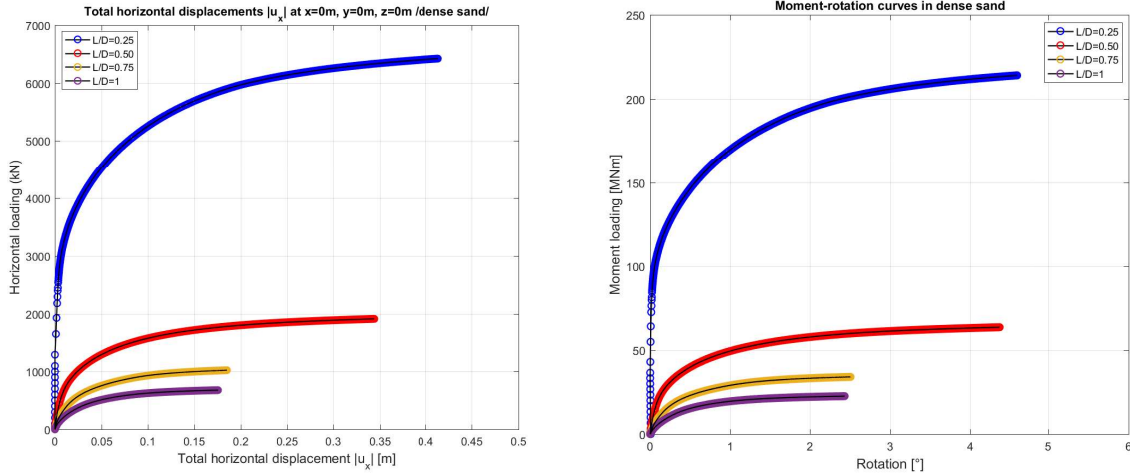


Figure 6.13. Horizontal loading-horizontal displacement curves for suction caissons with aspect ratios of 0.25, 0.5, 0.75 and 1 in dense sand measured at the center of the lid. **Figure 6.14.** Moment-rotation curves for suction caissons with aspect ratios of 0.25, 0.5, 0.75 and 1 in dense sand.

The caisson with an aspect ratio of 0.25 (lid diameter of 24 m) shows a very stiff response, it barely moves nor rotates until around 3000 kN-100 MNm. This behavior can be beneficial if high capacity and little displacements are demanded for the suction caisson.

6.2.4 Interpretation of results

The vertical load and embedment length dependency of the bearing capacity of caissons subjected to combined loading can be explained in a simple way. Since the vertically loaded caisson is highly dependent on the friction parameters [Collin and Charlier, 2016], a bucket that is extremely pushed in the soil and able to adhere to the soil particles stronger (higher friction angle means higher contact friction angle hence the capacity-increasing effects of denser sands), will be more resistant to destabilizing forces (moment, horizontal force) as a result. However, the vertical load "assists" the rotation, leading to increased vertical, horizontal displacements, as well as rotations. While the effect of vertical load is evident, the effect of embedment length (aspect ratio) on the displacements and rotations are hard to assess as they are significantly dependent on the vertical load level. This makes it hard to interpret and compare Figs. 6.6 and C.10-C.19.

6.3 Combined loading using HS and HS small strains models

The model with the aspect ratio of 1 in dense sand is further analyzed using different constitutive models. It is very important to calibrate the stiffness parameters of the HS and MC models first, if the aim is to compare the behavior using the two different soil

models. Several studies include recommendations for the stiffness parameters of MC and HS soil models, however the right choice of parameters vary from model to model.

While in many cases the use of $E_{MC}=E_{ref}^{50}$ is recommended and also [Datcheva, 2014] concludes based on Plaxis triaxial tests that the best agreement between the two models can be achieved by using $E_{MC}=E_{ref}^{50}$, based on the actual results of the numerical modelling [Datcheva, 2014] also points out that by using $E_{MC}=E_{ref}^{50}$ the two models do not produce the same results, unless a value of E_{MC} much larger than E_{ref}^{50} is used.

Triaxial soil tests in Plaxis have been run to find the HS stiffness parameters that give the best approximation of the MC triaxial test results. Tests showed that stiffness parameters of $E_{ref}^{50}=150$ MPa, $E_{ref}^{oed}=150$ MPa and $E_{ref}^{ur}=450$ MPa approximates the MC model behaviour the best in dense sand, meaning approximately $E_{ref}^{50}=2E_{MC}$.

To compare the behavior of MC and HS models, several models test have been run in Plaxis using different stiffness parameters in addition to the ones defined in Table 5.2. Initially the dense case is analyzed, after which the caisson behavior in medium dense and loose sands are analyzed as well. In Figs. 6.15 and 6.17 horizontal loading-horizontal displacements and moment-rotation curves for the MC and HS models can be seen in dense sand. Figs 6.16 and 6.18 are zoomed on the curves of interest.

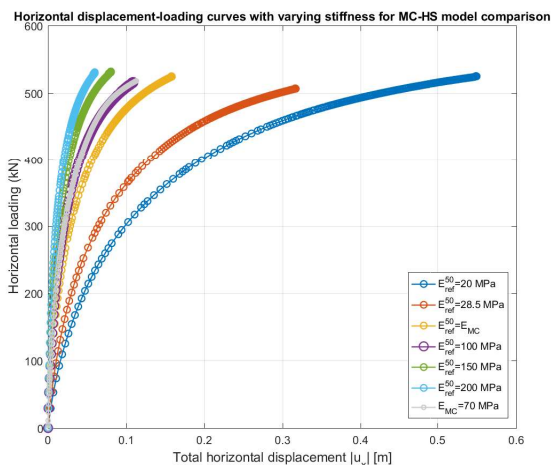


Figure 6.15. Horizontal loading-horizontal displacement curves for suction caissons with varying stiffness parameters for MC and HS soil model comparison in dense sand. The displacements are measured at the center of the lid.

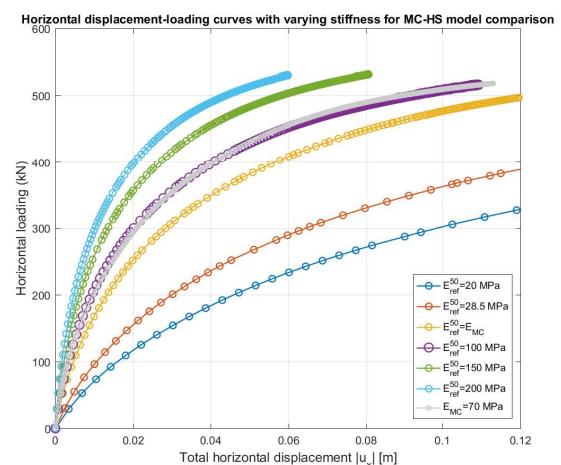


Figure 6.16. Horizontal loading-horizontal displacement curves for suction caissons with varying stiffness parameters for MC and HS soil model comparison in dense sand. The displacements are measured at the center of the lid.

Firstly, it can be seen that both the horizontal and moment curves give very similar results, therefore for the loose and medium dense soils only the horizontal loading-displacements curves will be considered. Several model tests have been run using relatively small and also bigger stiffness parameters. Even though the plaxis triaxial test results showed an acceptable similarity between the results of the HS and MC models, using $E_{ref}^{50}=150$ MPa, $E_{ref}^{oed}=150$ MPa and $E_{ref}^{ur}=450$ MPa, both the bearing capacities and displacements are

different (both at lower and higher loading rates) as it can be seen in Figs. 6.15 and 6.17. Only by using lower stiffness can the HS model obtain the MC model's results. Using $E_{ref}^{50}=150$ MPa, the model underestimates, while using $E_{ref}^{50}=E_{MC}$ the model overestimates the displacements. The perfect match can be obtained using $E_{ref}^{50}=100$ MPa, $E_{oed}^{50}=100$ MPa and $E_{ur}^{50}=300$ MPa.

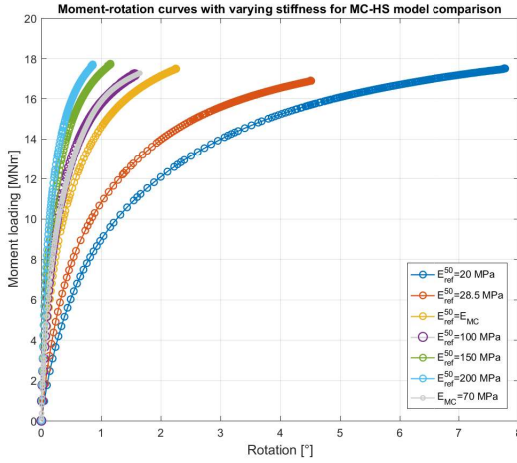


Figure 6.17. Moment-rotation curves for suction caissons with varying stiffness parameters for MC and HS soil model comparison in dense sand.

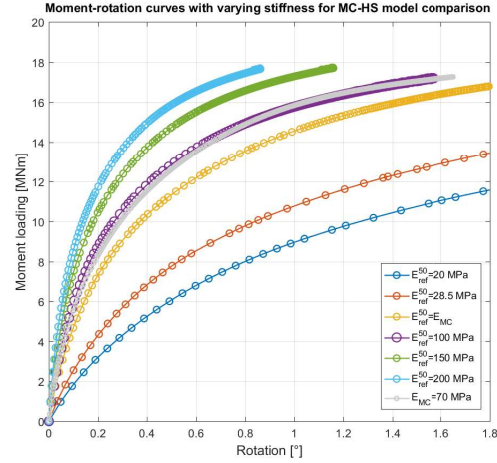


Figure 6.18. Moment-rotation curves for suction caissons with varying stiffness parameters for MC and HS soil model comparison in dense sand.

The horizontal load-displacement curves for the caissons in medium dense sands can be seen in Figs. 6.19 and 6.20. It can be seen that the HS model results with $E_{ref}^{50}=65$ MPa follows the MC model's results the best.

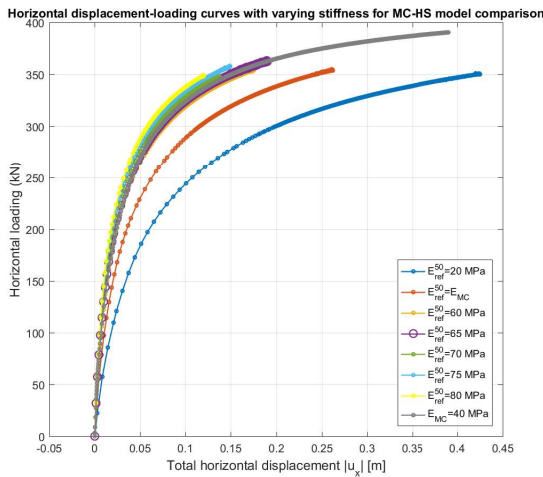


Figure 6.19. Horizontal loading-horizontal displacement curves for suction caissons with varying stiffness parameters for MC and HS soil model comparison in medium dense sand.

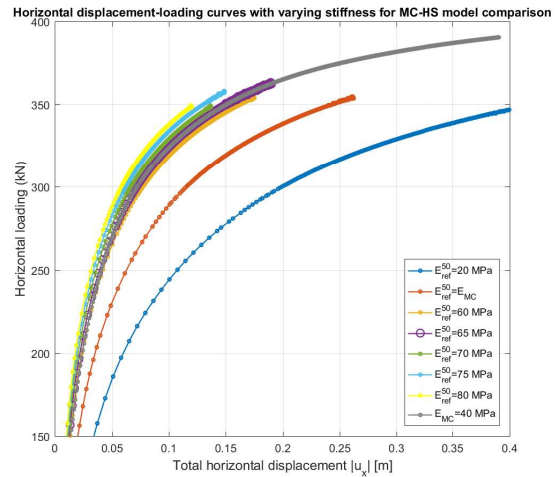


Figure 6.20. Horizontal loading-horizontal displacement curves for suction caissons with varying stiffness parameters for MC and HS soil model comparison in medium dense sand.

As mentioned before, the moment-rotation curves give very similar results as it can be seen in Fig. C.20. However it can also be noticed that the HS models require smaller displacements to reach failure and the capacities are also smaller compared to the MC model. The same can be observed in Fig. 6.21 for caissons in loose sands, where using $E_{ref}^{50}=30$ MPa gives the best agreement with the MC model's results.

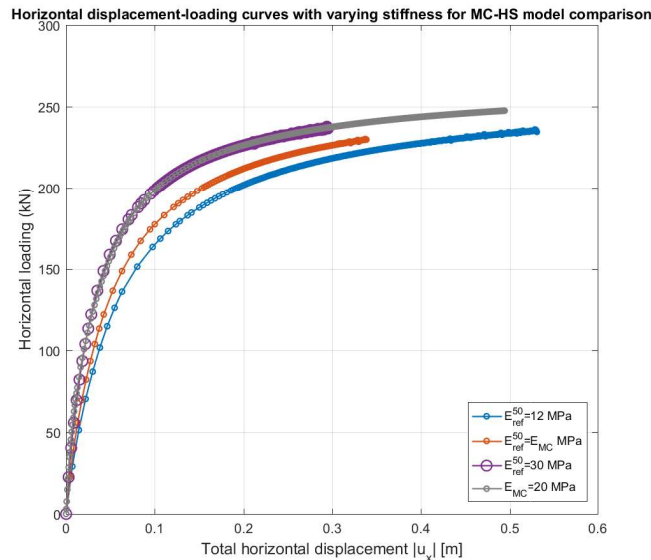


Figure 6.21. Horizontal loading-horizontal displacement curves for suction caissons with varying stiffness parameters for MC and HS soil model comparison in loose sand. The displacements are measured at the center of the lid.

Now that the HS model is calibrated, the MC, HS and HS-small strains models can be compared as well. The stiffness that gave the most similar results to the MC model are going to be used for the HS-small strains models.

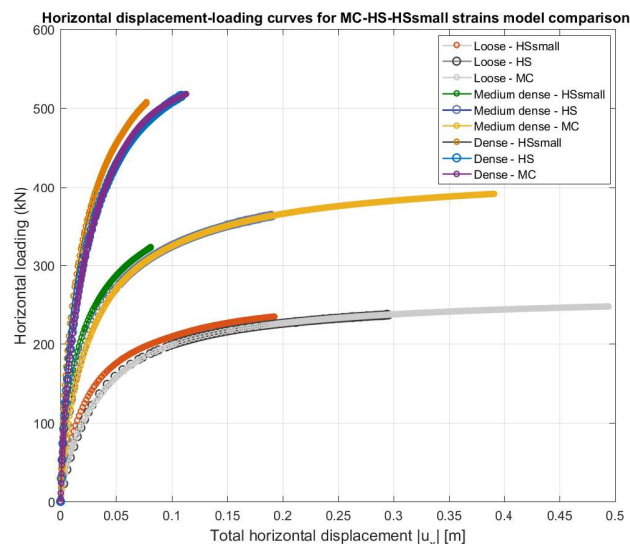


Figure 6.22. Horizontal loading-horizontal displacement curves for suction caissons for MC-HS-HSsmall soil model comparison in loose, medium dense and dense sands. The displacements are measured at the center of the lid.

The responses obtained with the MC, HS and HSsmall strain models in loose, medium dense and dense sands can be seen in Fig. 6.22. Comparing the results with the HS and MC model results, smaller bearing capacities and smaller displacements can be observed.

Trying obtain a better approximation with the HS-small strain models, the stiffness parameters were set equal to the ones of the MC models, meaning $E_{ref}^{50} = E_{MC}$ for all sands. As it can be seen in Fig.6.23, the results obtained using $E_{ref}^{50} = E_{MC}$ gives a closer approximation of the MC model results. However this way the displacements are overestimated compared to the HS and MC model results. The best approximation has been obtained in loose sand. A summary of the stiffness parameter used for this model comparison can be seen in Table 6.4.

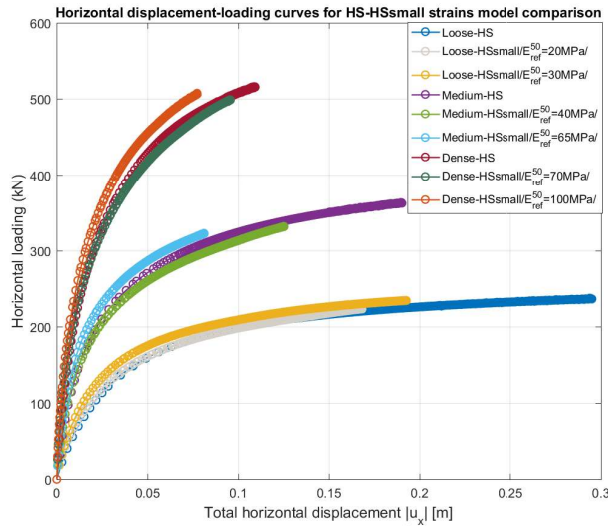


Figure 6.23. Horizontal loading-horizontal displacement curves for suction caissons for HS-HSsmall soil model comparison in loose, medium dense and dense sands. The displacements are measured at the center of the lid.

Table 6.4. Different stiffness parameters used for the model comparisons to obtain similar results.

| Sand relative density | Soil constitutive model | E_{ref}^{50} [MPa] | E_{oed}^{50} [MPa] | E_{ur}^{50} [MPa] | E_{MC} [MPa] |
|-----------------------|-------------------------|----------------------|----------------------|---------------------|----------------|
| Dense | MC | - | - | - | 70 |
| Dense | HS | 100 | 100 | 300 | - |
| Dense | HS-small | 70 | 70 | 210 | - |
| Medium dense | MC | - | - | - | 40 |
| Medium dense | HS | 65 | 65 | 195 | - |
| Medium dense | HS-small | 40 | 40 | 120 | - |
| Loose | MC | - | - | - | 20 |
| Loose | HS | 30 | 30 | 90 | - |
| Loose | HS-small | 20 | 20 | 60 | - |

6.3.1 Interpretation of results

The HS model gave similar results to the MC model when a stiffness $E_{ref}^{50} > E_{MC}$ was used, while the HS small strains model gave a better approximation of the MC model results using $E_{ref}^{50} = E_{MC}$, as suggested in several articles. Firstly it can be concluded based on the results that the more complex the soil constitutive model used, the smaller the corresponding displacements at the same load level, the smaller the obtainable bearing capacities and the displacements at failure. Secondly the transition between the elastic and plastic response is somewhat smoother using the HS and HS small strains models. This transition is most conspicuous in dense sand.

Conclusion 7

The advantages and disadvantages of each foundation type has been overviewed with a focus on the bearing behaviors, installation methods, construction and transporting. Given the fact that most projects are subjected to budget and time restrictions during the design phase, the suction caisson can provide a favorable foundation option to reduce overall costs and construction times. It has been concluded that the perfect choice of design codes and guidelines is case-sensitive, depending on the soil environment and loading conditions. In case of highly varying soil parameters and if better precision is needed, probabilistic methods should be used which represents the uncertainties with the statistical distribution of the soil parameters.

The suction caisson behavior under monotonic and cyclic, both moment and vertical loads in sands have been thoroughly studied as well. The drained and partially drained simulations showed different behavior. Faster rate of loading led to the generation of underpressure, while the increased water height showed to delay the onset of the cavitation phenomena, both of them dramatically increasing the tensile capacity. The accumulation of excessive downward deformations led to the conclusion that the tensile capacity should only be determined by the frictional components (ignoring the cavity phenomena) to comply with SLS requirements. Cyclic tests showed the decrease of stiffness, accumulation of deformations and increase in the size of the hysteresis (damping) with the progress of loading. It is still an unsolved problem to model the degradation or improvement of stiffness for field suction caissons.

In the numerical study a convergence analysis has been conducted with models consisting of rigid bodies and models of plate elements using Plaxis 3D. The latter showed faster and more stable convergence around an element number of 18000. The model was able to reproduce the results of a previously validated model, after which the parametric study could be started. The effect of different geometry, vertical load rate, soil relative density and the used soil constitutive model has been analyzed. Both the effect of embedment length and diameter has been checked. While both of them had a huge effect on the obtainable bearing capacities, the former showed a more significant influence on the results. Results also showed that the response is highly dependent on the soil relative density and vertical load rate; in dense soils the effect of vertical load rate and aspect ratio gets more significant as well. Model tests have been run with different soil constitutive models. The more complex models showed smaller bearing capacities and displacements at failure and a smoother transition between the elastic and plastic response compared to the MC model. As precision increases with calculation time and vica versa, it is important to decide the degree of precision needed to save calculation time. The HS and MC models run for the same amount of time, while the HSsmall strain models took 3-4 times more. Finding the right stiffness parameters for the comparison of numerical models is not straightforward and highly case-dependent. However using more advanced soil models to compare field behavior with numerical model behavior gives a better approximation.

Bibliography

- 4C-offshore, 2016.** 4C-offshore. *Suction bucket or caisson foundations*, 2016. URL <http://www.4coffshore.com/windfarms/suction-bucket-or-caisson-foundations-aid11.html>.
- Andersen, 2017.** Lars V. Andersen. *Advanced soil mechanics lecture slides*. <https://www.moodle.aau.dk/course/view.php?id=15188>, 2017.
- Benz, 2007.** Thomas Benz. *Small-Strain Stiffness of Soils and its Numerical Consequences*. Institut fur Geotechnik, 2007. ISBN 3921837553 / 9783921837559.
- Bowles, 1996.** Joseph E. Bowles. *Foundation analysis and design*. 5th edition. New York McGraw-Hill, 1996. ISBN 0079122477.
- Byrne, 2006.** R. B. Kelly; G. T. Houlsby; B. W. Byrne. *A comparison of field and laboratory tests of caisson foundations in sand and clay*. Géotechnique, 56, no. 9, 791–825. ISSN 0016–8505 / 1751–7656, 2006.
- Byrne, 2010.** R. B. Kelly; G. T. Houlsby; J. Huxtable; B. W. Byrne. *Field trials of suction caissons in sand for offshore wind turbine foundations*. Géotechnique, 56, no. 1, 3–10, 2010.
- Collin and Charlier, 2016.** B. Cerfontaine; F. Collin and R. Charlier. *Numerical modelling of transient cyclic vertical loading of suction caissons in sand*. Géotechnique, 66, no. 2, 121–136. ISSN/E-ISSN: 0016–8505 / 1751–7656, 2016.
- Czapp, 2014.** Z. Czapp. *Deep foundations (course book for deep foundation design, BUTE)*. http://oktatas.epito.bme.hu/pluginfile.php/23618/mod_resource/content/0/deep_foundations_textbook_-_theory.pdf, 2014. Last visited: 09-06-2014.
- Datcheva, 2014.** K.N. Vakili; Arash Alimardani Lavasan; Tom Schanz; Maria Datcheva. *The influence of the soil constitutive model on the numerical assessment of mechanized tunneling*. In Michael A. Hicks; Ronald B. J. Brinkgreve and Alexander Rohe (editors) *Numerical Methods in Geotechnical Engineering*, pages 889–894. ISBN: 978–1–138–00146–6 / 978–1–315–75182–5, 2014.
- Det Norske Veritas.** Det Norske Veritas. *Design of offshore wind turbine structures*. <http://www.dnv.com>. Last visited: 07-04-2016.
- GeotechnicalInfo, 2012.** GeotechnicalInfo. *Geotechnical materials*, 2012. URL http://www.geotechnicalinfo.com/geotechnical_materials.html.
- Gilbert, 2015.** Zhongqiang Liu; Suzanne Lacasse; Farrokh Nadim; Robert Gilbert. *Reliability of API and ISO guidelines for bearing capacity of offshore shallow foundations*. In T. Schweckendiek; A.F. van Tol; D. Pereboom; M.Th. van Staveren; P.M.C.B.M. Cools (editors), *Geotechnical Safety and Risk V.*, pages 821–828, 2015.

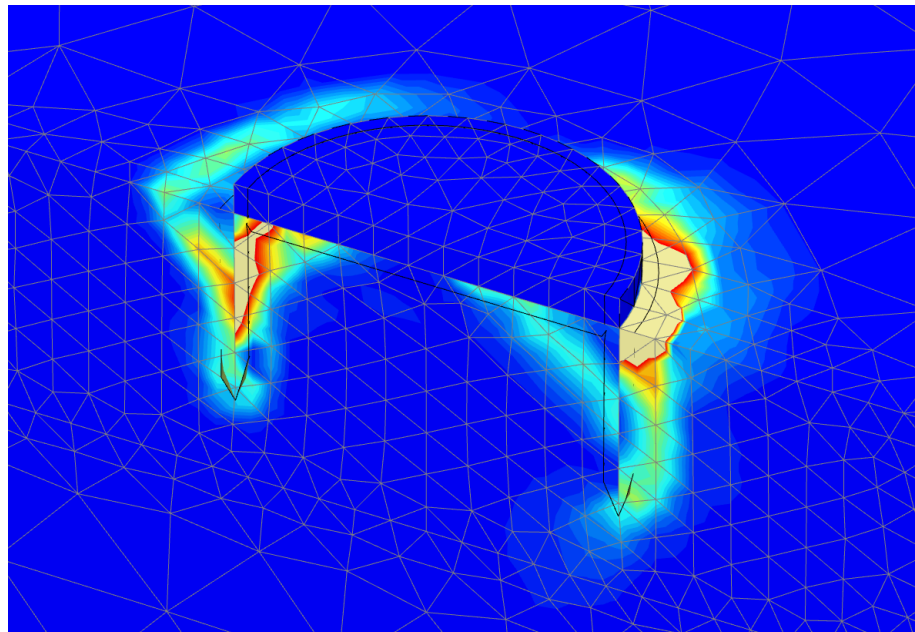
- Gourvenec, 2011.** Mark Randolph; Susan Gourvenec. *Offshore geotechnical engineering*. 1st edition. Spon press, 2011. ISBN 978-0415477444.
- Houlsby, 2010.** B.W. Byrne; G.T. Houlsby. *Assessing novel foundation options for offshore wind turbines*. pages 1–10, 2010.
- Houlsby, 2015.** G.T. Houlsby. *Interactions in offshore foundation design*. Géotechnique, 66, 791–825. ISSN/E-ISSN: 0016–8505 / 1751–7656, 2015.
- Ibsen, 2010.** Lars Bo Ibsen. *Analytical model for design of bucket foundations*, 2010.
- J.D.Sørensen, 2015.** M. Damgaard; L.V.Andersen; L.B.Ibsen; H.S.Toft; J.D.Sørensen. *A probabilistic analysis of the dynamic response of monopile foundations: Soil variability and its consequences*. In Professor P.D. Spanos (editors), Probabilistic Engineering Mechanics, pages 1–14. ISSN: 0266–8920, 2015.
- Józsa, 2014.** Dr. J. Farkas; V. Józsa. *Alapozás (BSc képzés)*. http://oktatas.epito.bme.hu/pluginfile.php/49386/mod_resource/content/1/Alapoz%C3%A1s%20e1%C5%91ad%C3%A1s%20jegyzet.pdf, 2014. Last visited: 26-05-2014.
- Kumarswamy, 2016.** W.M. Swolfs; R.B.J. Brinkgreve; S. Kumarswamy. *Plaxis material models manual*. <https://www.plaxis.com/support/manuals/plaxis-3d-manuals/>, 2016.
- Lesny, 2010.** Kerstin Lesny. *Foundations for offshore wind turbines: Tools for planning and design*. 1st edition. VGE-Verlag, 2010. ISBN 3867970424 / 9783867970426.
- Omar, 2014.** Samer Barakat; Radhi Alzubaidi; Maher Omar. *Probabilistic-based assessment of the bearing capacity of shallow foundations*. In Springer Berlin Heidelberg (editors), Arabian Journal of Geosciences, 8, 6441–6457. ISSN: 1866–7511 / 1866–7538, 2014.
- Ottosen, 2005.** Matti Ristinmaa; Niels Saabye Ottosen. *The mechanics of constitutive modeling*. Lund University, Sweden, 2005. ISBN 9780080525693.
- Penzes, 2016.** M.R.; Zania Varvara Penzes, P.; Jensen. *Suction caissons subjected to monotonic combined loading*. Proceedings of the 17th Nordic Geotechnical Meeting, pages 1–9. ISBN–e: 978–9935–24–002–6, 2016.
- Randolph, 1997.** M.F. Bransby; M. F. Randolph. *Combined loading of skirted foundations*. Géotechnique, vol. 48, no. 5, 637–655. ISSN/E-ISSN: 0016–8505 / 1751–7656, 1997.
- Schwägerl, 2016.** Christian Schwägerl. *Europe’s offshore wind industry booming as costs fall*, 2016. URL <https://www.theguardian.com/environment/2016/oct/20/europes-offshore-wind-industry-booming-as-costs-fall>.
- Thiicken, 2013.** M. Achmus; C.T. Akdag; K. Thiicken. *Load-bearing behavior of suction bucket foundations in sand*. Applied Ocean Research, vol. 43, 157–165, 2013.

Universal-foundations, 2017. Universal-foundations. *Suction caisson technology*, 2017. URL <http://universal-foundation.com/technology/>.

Wagner, 1990. P. Wagner. *Meerestechnik*. Ernst and Sohn, 1990. ISBN 10: 3433012121 / 13: 9783433012123.

Wikipedia, 2017. Wikipedia. *Suction caisson*, 2017. URL https://en.wikipedia.org/wiki/Suction_caisson.

Numerical modelling of foundations for offshore wind turbines



9TH SEMESTER PROJECT - MASTER THESIS
STRUCTURAL AND CIVIL ENGINEERING
AALBORG UNIVERSITY
AUGUST 12TH 2017



AALBORG UNIVERSITY
STUDENT REPORT

School of Engineering and Science
Study Board of Civil Engineering
Thomas Manns Vej 23, 9220 Aalborg Øst
<http://www.ses.aau.dk>

Title:

Numerical modelling of foundations
for offshore wind turbines

Project period:

April 2017 - August 2017

Participant(s):

Tamás Csaba Bogdán

Supervisors:

Johan Clausen
Laura Govoni

Total pages: 115

Report pages: 91

Appendix pages: 13

Completed: 12-08-2017

Synopsis:

The aim of the thesis is to study the long-term behavior of suction caissons (bucket foundations) in drained sand. The project consists of two parts, a literature review and a numerical study part.

In the former first the most commonly used foundation types (gravity-based, monopile, jacket and suction caisson foundations) are presented in detail with a focus on bearing behavior, construction and transport and installation and operating. Consequently the most commonly used design codes and guidelines are demonstrated, pointing out the differences between and shortcomings of the deterministic, semi-probabilistic and probabilistic models. Additionally, based on field, lab and numerical model tests by experts in suction caissons, the behavior of such foundations are studied under different loading conditions.

In the numerical analysis part first the different soil constitutive models are presented, then the model is validated based on a convergence analysis and an already calibrated model by [Thieken, 2013]. Later a numerical study is conducted to study the effects of different constitutive models, caisson geometries, loading types (uniaxial or combined loading), vertical loading on the response of the foundation.

Appendices

| | |
|---|----------|
| Appendix A List of Enclosures | 3 |
| Appendix B Model validation | 4 |
| B.1 Failure mechanism analysis | 4 |
| B.2 Convergence analysis | 4 |
| Appendix C Numerical study | 7 |
| C.1 Vertical loading, MC model | 7 |
| C.2 Combined loading, MC model | 9 |
| C.2.1 Different V/V_{max} values for different relative densities | 9 |
| C.2.2 Different V/V_{max} values for different aspect ratios | 10 |
| C.2.3 Combined loading using HS and HS small strains models | 13 |

List of Enclosures A

As more than 100 Plaxis files have been created with each of them occupying from 600 MB to 5000 MB of storage space, only a few important models are chosen to be included with the thesis, without the calculation data. Should the reader is interested in other files, the author can be contacted.

- **Matlab files for Plaxis 3D design:** contains the exported results and the matlab files created to plot these results,
- **Plaxis 3D design:** contains two models: a rigid body model from the convergence analysis part and a plate element model from the numerical study part with the MC and HSsmall strain models and all the load stages.

Model validation B

B.1 Failure mechanism analysis

The tables containing the results of the calculations for the different model sizes can be seen in this section.

Table B.1. Capacities and total displacements of the examined models.

| Model sizes | $\sum M_{stage}$ values [-] | Total displacement at $x=3$ m, $y=0$ m, $z=0$ m $(u)[10^{-3}\text{m}]$ | Total displacement at $x=-3$ m, $y=0$ m, $z=0$ m $(u)[10^{-3}\text{m}]$ |
|-------------|-----------------------------|--|---|
| 30×15×15 | 0.4527 | 3.955 | 4.230 |
| 40×20×20 | 0.4618 | 4.154 | 4.440 |
| 50×25×18 | 0.4762 | 4.250 | 4.526 |
| 60×30×18 | 0.4818 | 4.353 | 4.631 |
| 60×30×30 | 0.4838 | 4.400 | 4.690 |
| 72×36×18 | 0.5342 | 4.460 | 4.730 |
| 72×36×36 | 0.5357 | 4.544 | 4.820 |
| 100×50×50 | 0.6299 | 4.768 | 5.040 |

Table B.2. Ranges of total deviatoric strains and total displacements of the examined models.

| Model sizes | Range of total deviatoric strains, /with maximum strain/ [-] | Total displacement at $x=3$ m, $y=0$ m $z=-6$ m $(u)[10^{-3}\text{m}]$ | Total displacement at $x=-3$ m, $y=0$ m $z=-6$ m $(u)[10^{-3}\text{m}]$ |
|-------------|--|--|---|
| 30×15×15 | 0.15-0.9 /20.49/ | 1.595 | 1.633 |
| 40×20×20 | 0.015-0.035 /59.25/ | 1.564 | 1.609 |
| 50×25×18 | 0.2-0.9 /5.08/ | 1.500 | 1.560 |
| 60×30×18 | 0.15-0.7 /32.9/ | 1.420 | 1.538 |
| 60×30×30 | 0.4-1.5 /52.5/ | 1.440 | 1.530 |
| 72×36×18 | 0.2-1.4 /31.43/ | 1.406 | 1.477 |
| 72×36×36 | 0-0.1 /19.08/ | 1.429 | 1.483 |
| 100×50×50 | 0.25-2.5 /11.91/ | 1.308 | 1.415 |

B.2 Convergence analysis

The tables containing the calculation results of all 4 model types:

Table B.3. Results obtained from the finite element calculations for the rigid body model (the total displacements are measured on the x - z plane).

| Coarseness factor | Number of elements | $\sum M_{stage}$ | $ u $ at | $ u $ at | $ u $ at |
|-------------------|--------------------|------------------|---|--|---|
| | | | $x=3$ m, $z=0$ m [*10 ⁻³ m] | $x=-3$ m, $z=0$ m [*10 ⁻³ m] | $x=0$ m, $z=0$ m [*10 ⁻³ m] |
| 1 | 4747 | 0.8279 | 3.702 | 3.983 | 3.167 |
| 0.8 | 5470 | 0.6978 | 3.930 | 4.210 | 3.340 |
| 0.6 | 5669 | 0.7561 | 3.920 | 4.210 | 3.330 |
| 0.4 | 8127 | 0.5954 | 4.097 | 4.404 | 3.458 |
| 0.3 | 10082 | 0.5595 | 4.193 | 4.488 | 3.520 |
| 0.2 | 18475 | 0.4762 | 4.250 | 4.527 | 3.551 |
| 0.1 | 78792 | 0.4179 | 4.314 | 4.590 | 3.586 |

Table B.4. Results obtained from the finite element calculations for the plate model with $\gamma_{steel}=77$ kN/m³ and E=21 GPa (the total displacements are measured on the x - z plane).

| Coarseness factor | Number of elements | $\sum M_{stage}$ | $ u $ at | $ u $ at | $ u $ at |
|-------------------|--------------------|------------------|---|--|---|
| | | | $x=3$ m, $z=0$ m [*10 ⁻³ m] | $x=-3$ m, $z=0$ m [*10 ⁻³ m] | $x=0$ m, $z=0$ m [*10 ⁻³ m] |
| 1 | 4747 | 0.7829 | 4.627 | 5.2 | 3.659 |
| 0.8 | 5470 | 0.7856 | 4.657 | 5.236 | 3.682 |
| 0.6 | 5669 | 0.7619 | 4.702 | 5.292 | 3.725 |
| 0.4 | 8127 | 0.6890 | 4.690 | 5.279 | 3.713 |
| 0.3 | 10082 | 0.6410 | 4.711 | 5.310 | 3.730 |
| 0.2 | 18475 | 0.5305 | 4.761 | 5.367 | 3.776 |
| 0.15 | 32259 | 0.5160 | 4.768 | 5.386 | 3.779 |
| 0.1 | 78792 | 0.4923 | 4.770 | 5.392 | 3.790 |

Table B.5. Results obtained from the finite element calculations for the plate model with $\gamma_{steel}=0$ kN/m³ and E=21 GPa (the total displacements are measured on the x - z plane).

| Coarseness factor | Number of elements | $\sum M_{stage}$ | $ u $ at | $ u $ at | $ u $ at |
|-------------------|--------------------|------------------|---|--|---|
| | | | $x=3$ m, $z=0$ m [*10 ⁻³ m] | $x=-3$ m, $z=0$ m [*10 ⁻³ m] | $x=0$ m, $z=0$ m [*10 ⁻³ m] |
| 1 | 4747 | - | 6.490 | | |
| 0.8 | 5470 | - | 6.513 | | |
| 0.6 | 5669 | - | 6.619 | | |
| 0.4 | 8127 | - | 6.640 | | |
| 0.3 | 10082 | - | 6.669 | | |
| 0.2 | 18475 | - | 6.725 | | |
| 0.15 | 32259 | - | 6.741 | | |
| 0.1 | 78792 | - | 6.715 | | |

Table B.6. Results obtained from the finite element calculations for the plate model with $\gamma_{steel}=0$ kN/m^3 and $E=210$ GPa (the total displacements are measured on the x - z plane).

| Coarseness factor | Number of elements | $\sum M_{stage}$ | $ u $ at | $ u $ at | $ u $ at |
|-------------------|--------------------|------------------|---|--|---|
| | | | $x=3$ m, $z=0$ m [*10 ⁻³ m] | $x=-3$ m, $z=0$ m [*10 ⁻³ m] | $x=0$ m, $z=0$ m [*10 ⁻³ m] |
| 1 | 4747 | 0.7640 | 4.486 | 4.133 | 3.529 |
| 0.8 | 5470 | 0.7547 | 4.519 | 4.163 | 3.553 |
| 0.6 | 5669 | 0.7407 | 4.577 | 4.219 | 3.595 |
| 0.4 | 8127 | 0.6686 | 4.646 | 4.275 | 3.640 |
| 0.3 | 10082 | 0.6087 | 4.673 | 4.307 | 3.660 |
| 0.2 | 18475 | 0.5078 | 4.719 | 4.365 | 3.697 |
| 0.1 | 78792 | 0.4776 | 4.730 | 4.407 | 3.715 |

C.1 Vertical loading, MC model

Vertical loading-total vertical displacement curves for a suction caisson with different embedment lengths in loose, medium dense and dense sand can be seen in Figs. C.1, C.2 and C.3. To better show the effect of relative density on the responses, the load-displacement curves in case of an aspect ratio of 1 for loose, medium dense and dense sands can be seen in Fig. 6.3.

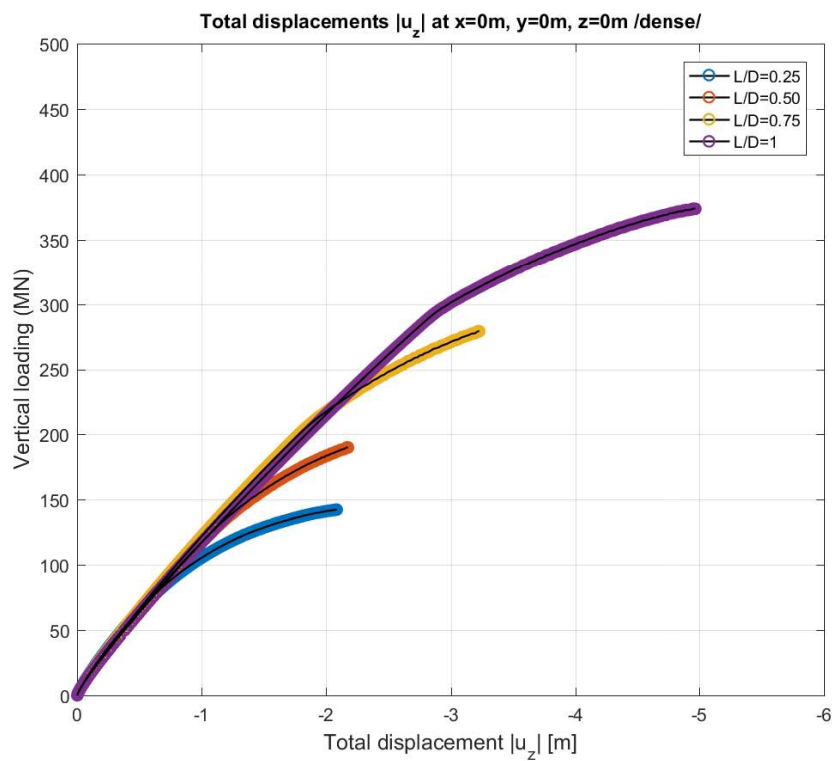


Figure C.1. Vertical loading-total vertical displacement curves for suction caissons with aspect ratios of 0.25, 0.5, 0.75 and 1 in dense sand.

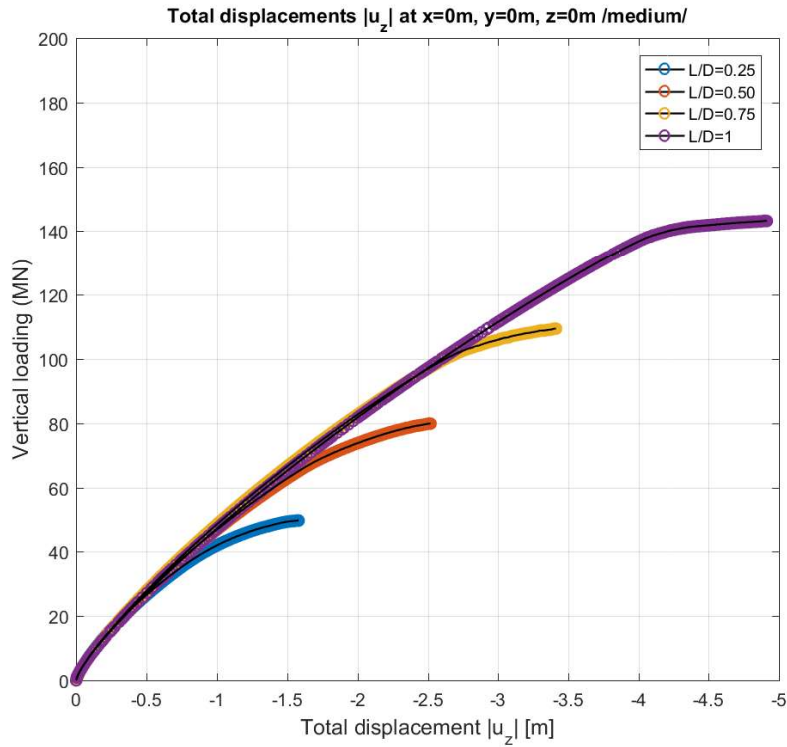


Figure C.2. Vertical loading-total vertical displacement curves for suction caissons with aspect ratios of 0.25, 0.5, 0.75 and 1 in medium dense sand.

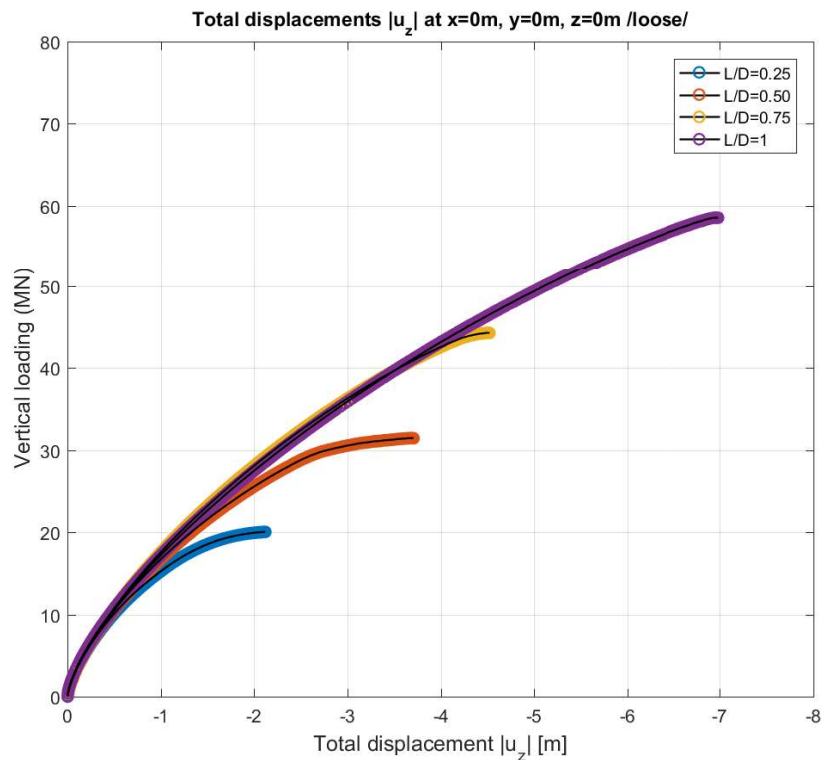


Figure C.3. Vertical loading-total vertical displacement curves for suction caissons with aspect ratios of 0.25, 0.5, 0.75 and 1 in loose sand.

C.2 Combined loading, MC model

C.2.1 Different V/V_{max} values for different relative densities

Horizontal displacement and rotation

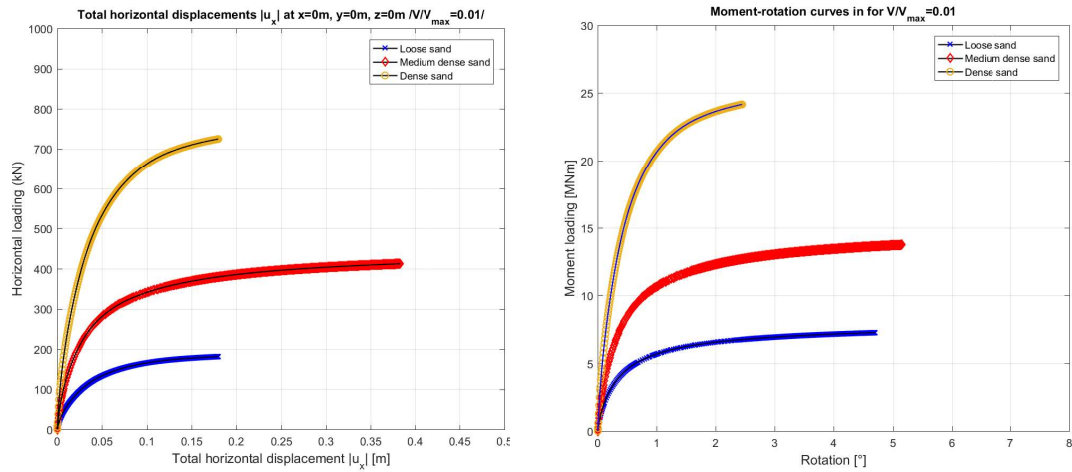


Figure C.4. Horizontal loading-horizontal displacement curves for suction caissons subjected to a vertical load level of $V/V_{max} = 0.01$ in loose, medium and dense sands, measured at the center of the lid.

Figure C.5. Moment-rotation curves for suction caissons subjected to a vertical load level of $V/V_{max} = 0.01$ in loose, medium and dense sands.

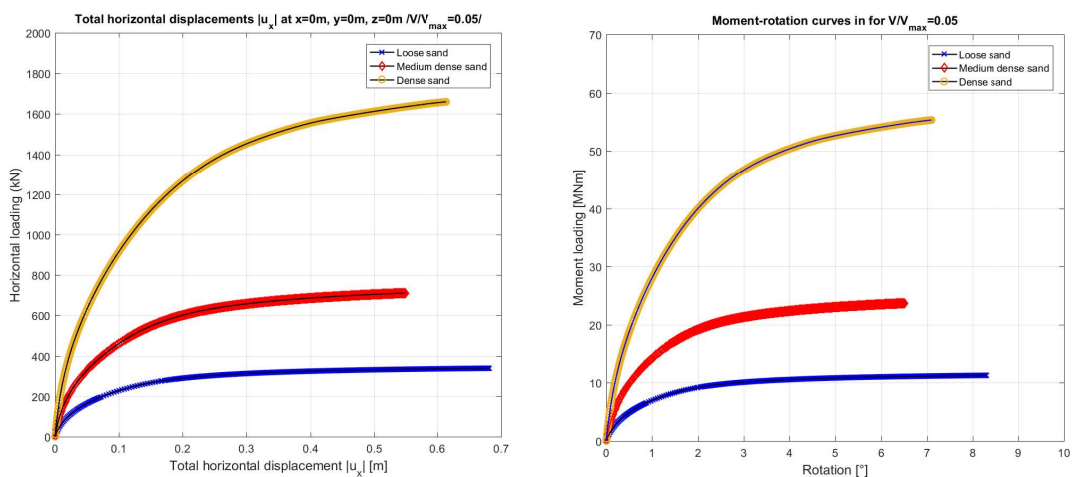


Figure C.6. Horizontal loading-horizontal displacement curves for suction caissons subjected to a vertical load level of $V/V_{max} = 0.05$ in loose, medium and dense sands measured at the center of the lid.

Figure C.7. Moment-rotation curves for suction caissons subjected to a vertical load level of $V/V_{max} = 0.05$ in loose, medium and dense sands.

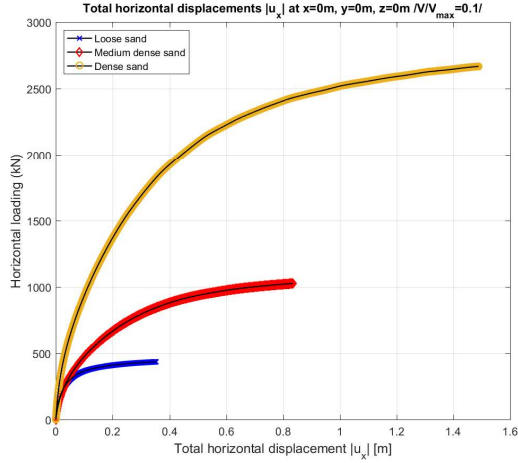


Figure C.8. Horizontal loading-horizontal displacement curves for suction caissons subjected to a vertical load level of $V/V_{max}=0.1$ in loose, medium and dense sands measured at the center of the lid.

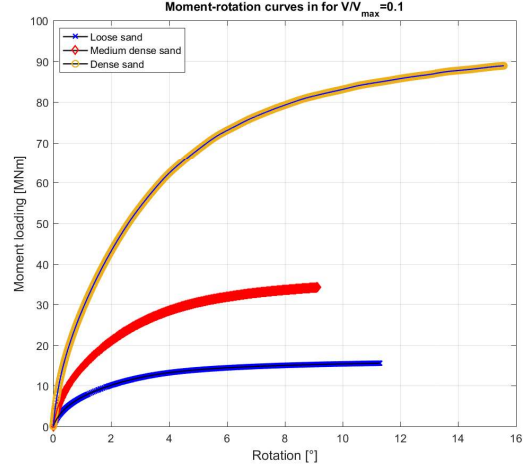


Figure C.9. Moment-rotation curves for suction caissons subjected to a vertical load level of $V/V_{max}=0.1$ in loose, medium and dense sands.

C.2.2 Different V/V_{max} values for different aspect ratios

Horizontal displacement and rotation

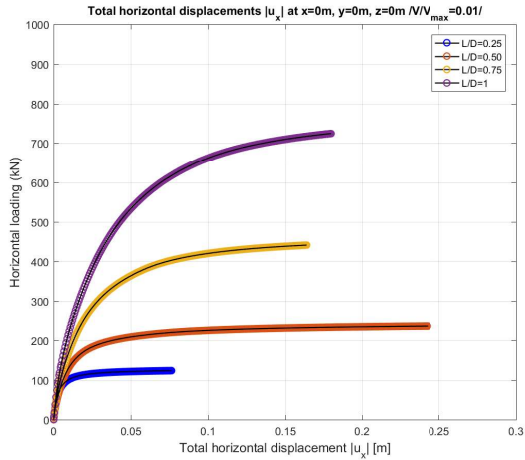


Figure C.10. Horizontal loading-horizontal displacement curves for suction caissons with different embedment lengths, subjected to a vertical load level of $V/V_{max}=0.01$ in dense sand. The displacements are measured at the center of the lid.

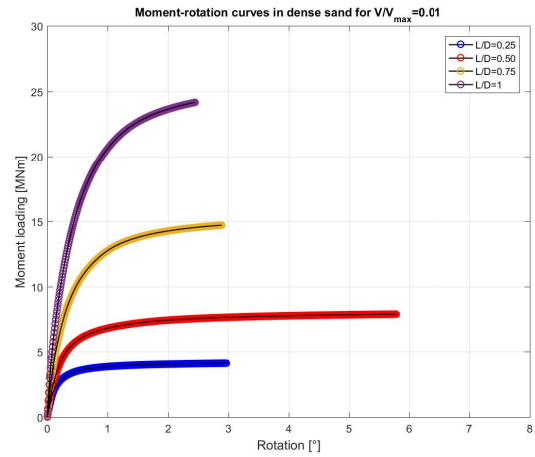


Figure C.11. Moment-rotation curves for suction caissons with different embedment lengths, subjected to a vertical load level of $V/V_{max}=0.01$ in dense sand.

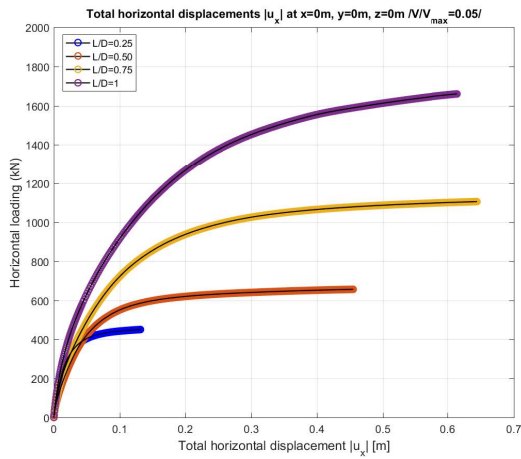


Figure C.12. Horizontal loading-horizontal displacement curves for suction caissons with different embedment lengths, subjected to a vertical load level of $V/V_{max}=0.05$ in dense sand. The displacements are measured at the center of the lid.

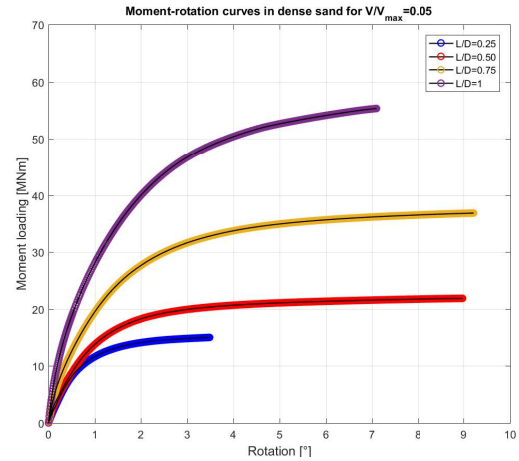


Figure C.13. Moment-rotation curves for suction caissons with different embedment lengths, subjected to a vertical load level of $V/V_{max}=0.05$ in dense sand.

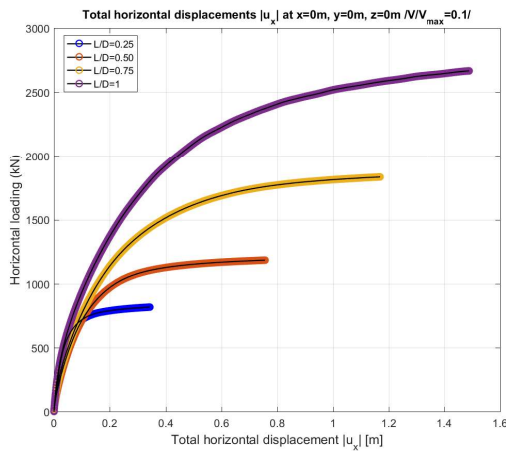


Figure C.14. Horizontal loading-horizontal displacement curves for suction caissons with different embedment lengths, subjected to a vertical load level of $V/V_{max}=0.1$ in dense sand. The displacements are measured at the center of the lid.

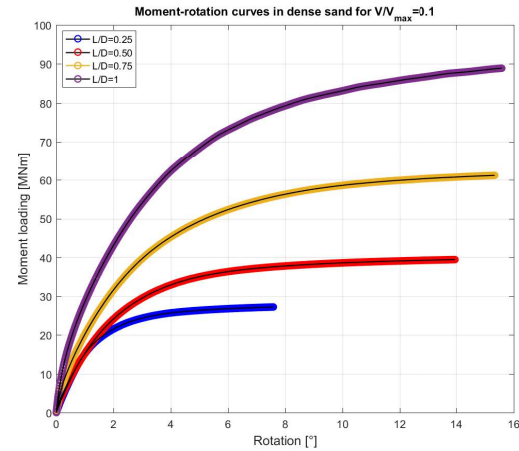


Figure C.15. Moment-rotation curves for suction caissons with different embedment lengths, subjected to a vertical load level of $V/V_{max}=0.1$ in dense sand.

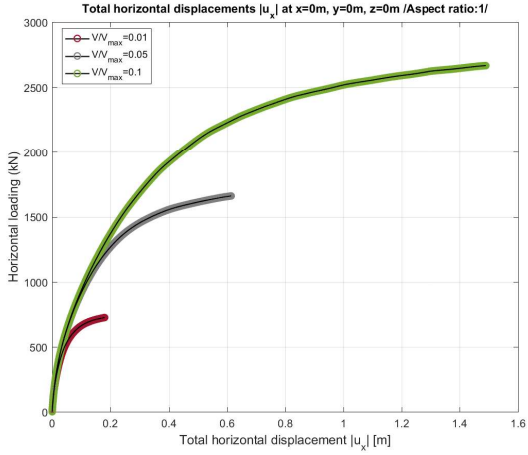


Figure C.16. Horizontal loading-horizonal displacement curves for suction caissons with an aspect ratio of 1, subjected to different vertical load levels ($V/V_{max}=0.01$, 0.05 and 0.1) in dense sand. The displacements are measured at the center of the lid.

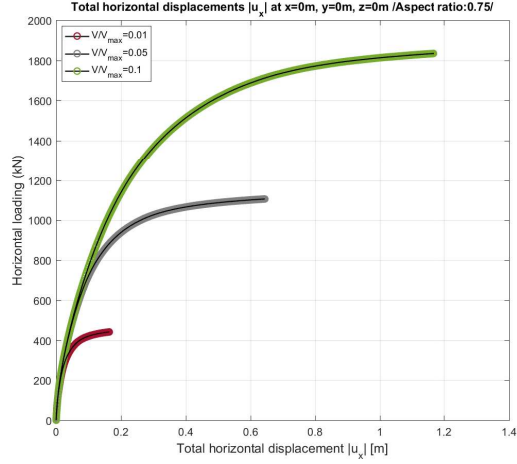


Figure C.17. Horizontal loading-horizonal displacement curves for suction caissons with an aspect ratio of 0.75, subjected to different vertical load levels ($V/V_{max}=0.01$, 0.05 and 0.1) in dense sand. The displacements are measured at the center of the lid.

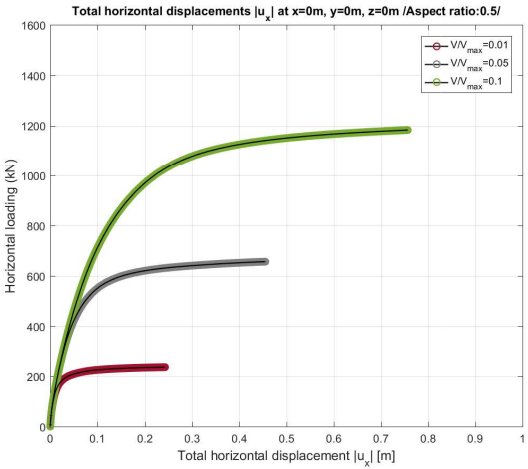


Figure C.18. Horizontal loading-horizonal displacement curves for suction caissons with an aspect ratio of 0.5, subjected to different vertical load levels ($V/V_{max}=0.01$, 0.05 and 0.1) in dense sand. The displacements are measured at the center of the lid.

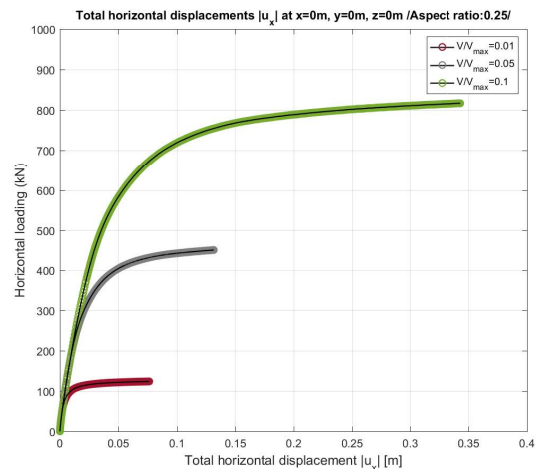


Figure C.19. Horizontal loading-horizonal displacement curves for suction caissons with an aspect ratio of 0.25, subjected to different vertical load levels ($V/V_{max}=0.01$, 0.05 and 0.1) in dense sand. The displacements are measured at the center of the lid.

C.2.3 Combined loading using HS and HS small strains models

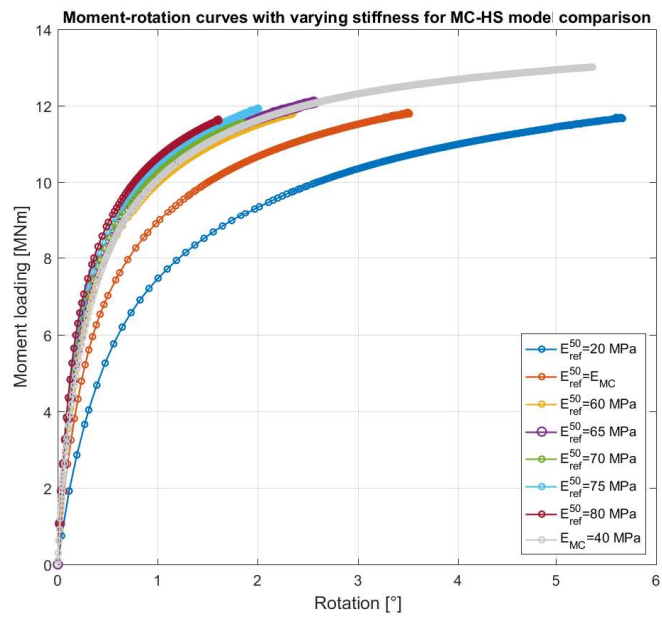


Figure C.20. Moment-rotation curves for suction caissons with varying stiffness parameters for MC and HS soil model comparison in medium dense sand.